# HOT-FILAMENT PLASMA ENHANCED CHEMICAL VAPOUR DEPOSITION OF TRANSFER-FREE GRAPHENE USING NICKEL CATALYST

**MAISARA OTHMAN**

**FACULTY OF SCIENCE**
**UNIVERSITY OF MALAYA**
**KUALA LUMPUR**

**2018**

University of Malaya

# HOT-FILAMENT PLASMA ENHANCED CHEMICAL VAPOUR DEPOSITION OF TRANSFER-FREE GRAPHENE USING NICKEL CATALYST

**MAISARA OTHMAN**

**THESIS SUBMITTED IN FULFILMENT OF THE REQUIREMENTS FOR THE DEGREE OF DOCTOR OF PHILOSOPHY**

**DEPARTMENT OF PHYSICS**
**FACULTY OF SCIENCE**
**UNIVERSITY OF MALAYA**
**KUALA LUMPUR**

**2018**

University of Malaya

**UNIVERSITY OF MALAYA**

**ORIGINAL LITERARY WORK DECLARATION**

Name of Candidate: **MAISARA OTHMAN**

Matric No: **SHC 130062**

Name of Degree: Doctor of Philosophy

Title of Thesis: **HOT-FILAMENT PLASMA ENHANCED CHEMICAL VAPOUR DEPOSITION OF TRANSFER-FREE GRAPHENE USING NICKEL CATALYST**

Field of Study: **EXPERIMENTAL PHYSICS**

I do solemnly and sincerely declare that:

(1) I am the sole author/writer of this Work;
(2) This Work is original;
(3) Any use of any work in which copyright exists was done by way of fair dealing and for permitted purposes and any excerpt or extract from, or reference to or reproduction of any copyright work has been disclosed expressly and sufficiently and the title of the Work and its authorship have been acknowledged in this Work;
(4) I do not have any actual knowledge nor do I ought reasonably to know that the making of this work constitutes an infringement of any copyright work;
(5) I hereby assign all and every rights in the copyright to this Work to the University of Malaya ("UM"), who henceforth shall be owner of the copyright in this Work and that any reproduction or use in any form or by any means whatsoever is prohibited without the written consent of UM having been first had and obtained;
(6) I am fully aware that if in the course of making this Work I have infringed any copyright whether intentionally or otherwise, I may be subject to legal action or any other action as may be determined by UM.

Candidate's Signature Date:

Subscribed and solemnly declared before,

Witness's Signature Date:

Name:

Designation:

University of Malaya

**HOT-FILAMENT PLASMA ENHANCED CHEMICAL VAPOUR DEPOSITION OF TRANSFER-FREE GRAPHENE USING NICKEL CATALYST**

## ABSTRACT

The synthesis and characterization of transfer-free graphene using a home-built plasma enhanced chemical vapour deposition (PECVD) system were studied in this research. Most of the graphene growth using the CVD technique require a metal surface and an additional lift-off step to transfer the graphene from the metal surface. The structures of the graphene could be damaged during the transferring process, leading to a performance which is far below the theoretical value in reality. Nevertheless, CVD technique can produce graphene with a large area that has vital roles in the industry and engineering. Its potential roles have led to the fabrication of transfer-free graphene reported by some existing studies but the commercialization of this technique remains challenging due to the complexity of the method. In this study, the transfer-free graphene was deposited on the silicon dioxide ($SiO_2$) substrate at a relatively low temperature using the nickel (Ni) thin films. The Ni layer was used as a catalyst to assist the formation of graphene at the Ni-substrate interface. Prior to the deposition of graphene, a thin Ni film was deposited onto the $SiO_2$ substrate using the sputtering technique. The morphology, thickness, and grain size of the Ni films were shown to be dependent on the Ni target to substrate distance. Furthermore, the structure, morphology, and chemical bonding of the transfer-free graphene were found to be strongly dependent on the thickness and the grain size of the Ni films. The grain size was dependent on the Ni thickness, which had an impact on the Ni grain boundaries. The grain boundary acted as the nucleation site for the carbon atom to diffuse through the Ni. The formation of the transfer-free film shifted from carbon to graphene when the Ni thickness was increased. An optimized Ni thickness resulted in a more ordered graphene with lesser defect. Furthermore, the addition of a hot-filament to the PECVD system further improved the quality of the transfer-free graphene under

University of Malaya

the same deposition condition. This is because the Ni catalyst showed better catalytic effects during graphene deposition using the hot-filament assisted PECVD as compared to the simple PECVD. The thermal effect promoted the formation of a less defective graphene with a more ordered structure, which could be achieved by larger Ni grain size and grains boundaries. The resulting transfer-free graphene films were investigated for their structural, chemical bonding and morphology. Deposition time strongly influenced the number of graphene layers and structural ordering. The graphene film shifted from multilayer towards bilayer graphene with lower defects when the deposition time was decreased by using the optimum parameters from the above studies, the highest quality transfer-free graphene was obtained by optimizing the substrate temperature. Decreasing the substrate temperature had increased the number of graphene layer and resulted in a highly defective graphene. The optimized substrate temperature for bilayer graphene growth was 400°C at deposition time of 1 minute. The formation of defects due to a large distribution of non-perfect hexagonal graphene rings had led to a high inclusion of hydroxyl groups and oxygen, vacancy defects and ultra-long defective edges which subsequently affected the wettability and the magnetic properties of the graphene films.

**Keywords:** Transfer-free graphene, PECVD, Nickel catalyst, Raman spectroscopy

University of Malaya

**PEMENDAPAN WAP KIMIA SECARA PEMANASAN FILAMEN PENINGKATAN PLASMA BAGI GRAFENA BEBAS PEMINDAHAN MENGGUNAKAN MANGKIN NI**

## ABSTRAK

Sintesis grafena bebas pemindahan menggunakan system pemendapan wap kimia secara peningkatan plasma (PECVD) buatan sendiri dan penciriannya telah dipelajari di dalam hasil kerja ini. Kebanyakan pertumbuhan grafena yang menggunakan teknik pemendapan wap kimia, permukaan logam dan langkah tambahan bagi proses pemindahan grafena diperlukan. Struktur grafena berkemungkinan mengalami kerosakan semasa proses pemindahan dan menghasilkan filem yang kurang berprestasi daripada nilai teori yang sebenar. Namun, teknik ini boleh menghasilkan grafena berskala besar dimana mempunyai peranan yang penting di dalam industri dan kejuruteraan. Keupayaan peranan ini telah mendorong fabrikasi grafena bebas pemindahan dimana telah di laporkan oleh beberapa kajian sedia ada tetapi penggunaan teknik yang digunakan mencabar dan kompleks. Dalam kajian ini, grafena bebas pemindahan dimendapkan di atas substrat silikon teroksida ($SiO_2$) pada suhu yang agak rendah menggunakan filem nipis nikel (Ni). Lapisan Ni telah digunakan sebagai pemangkin untuk membantu penghasilan grafena di permukaan diantara Ni dan substrat. Sebelum proses pemendapan grafena, filem nipis Ni telah dimendapkan di atas substrat $SiO_2$ menggunakan teknik percikkan. Morfologi, ketebalan dan saiz butiran filem Ni telah ditemui bersandar kepada jarak sasaran Ni kepada substrat. Tambahan, struktur, morfologi, dan ikatan kimia grafena bebas pemindahan telah dijumpai bersandar kuat terhadap ketebalan dan saiz butiran filem Ni. Saiz butiran bersandar dengan ketebalan Ni dimana mempunyai impak pada saiz sempadan butiran. Sempadan butiran bertindak sebagai tapak penukleasan bagi atom karbon untuk meresap melalui Ni. Pembentukan grafena bebas pemindahan bertukar daripada karbon kepada grafena apabila ketebalan Ni meningkat. Ketebalan Ni yang optimum menghasilkan grafena yang berstruktur lebih tertib dan kurang kecacatan.

University of Malaya

Penggunaan pemanasan filamen kedalam sistem PECVD dalam kondisi yang sama menambah baik kualiti grafena bebas pemindahan. Ini adalah kerana mangkin Ni menunjukkan efek mangkin yang lebih baik semasa proses pemendapan grafena menggunakan pemendapan wap kimia secara peningkatan plasma dengan pemanasan filamen (HF-PECVD) berbanding PECVD. Kesan daripada pemanasan ini adalah menggalakkan pertumbuhan grafena kurang kecacatan dengan struktur yang lebih tertib, dimana telah dicapai melalui peningkatkan saiz butiran dan sempadan butiran Ni. Struktur, ikatan kimia dan morfologi bagi filem grafena bebas pemindahan yang terhasil telah dipelajari. Masa pemendapan sangat mempengaruhi bilangan lapisan dan struktur susunan grafena yang terhasil. Bilangan lapisan grafena berkurangan dari beberapa lapisan kepada dua lapisan dengan kadar kecacatan yang lebih rendah apabila masa pemendapan berkurangan. Dengan menggunakan parameter yang optimum daripada kajian di atas, suhu substrat yang optimum boleh dikaji untuk menghasilkan grafena bebas pemindahan yang berkualiti dengan suhu yang rendah. Menurunkan suhu substrat meningkatkan jumlah lapisan grafena dan menghasilkan grafena berkecacatan tinggi. Suhu substrat yang optimum bagi pertumbuhan dua lapisan grafena adalah 400°C dengan masa pemendapan selama 1 minit. Pertumbuhan kecacatan disebabkan oleh taburan tak sempuna cincin heksagon yang tinggi dimana menggalakkan penghasilan rangkuman kumpulan hidroksil dan oksigen yang tinggi, kekosongan kecacatan dan sudut kecacatan yang lebih panjang kedalam struktur rangkaian grafena, yang mana memberi kesan kepada kebolehbasahan dan sifat magnet filem grafena ini.

**Katakunci**: Grafena bebas pemindahan, PECVD, mangkin Ni, Raman spektroskopi

University of Malaya

## ACKNOWLEDGEMENTS

Firstly and foremost, thanks to Allah on whom ultimately we depend for sustenance and guidance, the Almighty, for giving opportunity, determination and strength to complete my PhD work.

I would like to express my deepest appreciation to Professor Datin Dr. Saadah Abdul Rahman and Dr. Richard Ritikos for being my supervisors all these years. My research work would not has been possible without the generous assistance from them in terms of guidance, support and wisdom throughout these years.

I would like to take this opportunity to express my gratitude to the University of Malaya for awarding the SBUM scholarship and postgraduate research grant (PG120-2014B) for the financial support of my research work. My gratitude also goes to all staffs in department of physics who has contributed their role in my PhD journey.

I would also like to thanks my senior and dear friends, Dr. Goh, Ijah, Mai, Hajar, Nana, Zira, Linda, Syed and others, who always support each other's throughout our journey in UM.

My acknowledgement would be incomplete without thanking my family. The blessing of my parents and mother in law, and love of my siblings.

Finally, my most sincere gratitude is extend to my husband, Muhammad Aiman and our beloved daughter, Aisar Imtinan for their understanding, love and supports. I love you guys.

University of Malaya

## TABLE OF CONTENTS



University of Malaya

University of Malaya

University of Malaya

University of Malaya

University of Malaya

## LIST OF FIGURES



University of Malaya

University of Malaya

University of Malaya

University of Malaya

University of Malaya

University of Malaya

## LIST OF TABLES



University of Malaya

## LIST OF SYMBOLS AND ABBREVIATIONS

| | | |
|---|---|---|
| Ar | : | Argon |
| AFM | : | Atomic force microscopy |
| C | : | Carbon |
| $C_A$ | : | Contact angle |
| $CH_4$ | : | Methane |
| Cu | : | Copper |
| FESEM | : | Field emission scanning electron microscopy |
| FWHM | : | Full width half maximum |
| HCl | : | Hydrochloric acid |
| HF-PECVD | : | Hot-filament plasma enhanced chemical vapour deposition |
| $H_2$ | : | Hydrogen |
| $M_S$ | : | Saturation magnetization |
| nc-G | : | Nano crystalline graphene |
| Ni | : | Nickel |
| O | : | Oxygen |
| PECVD | : | Plasma enhanced chemical vapour deposition |
| RF | : | Radio frequency |
| Si | : | Silicon |
| $SiO_2$ | : | Silicon dioxide |
| sccm | : | Standard cubic centimeters per minute |
| $T_S$ | : | Substrate temperature |
| VSM | : | Vibrating magnetometer measurement |
| XPS | : | X-ray photoelectron spectroscopy |
| XRD | : | X-ray diffraction |

University of Malaya

# CHAPTER 1: INTRODUCTION

## 1.1 Introduction of Graphene and Graphene Growth

Graphene is a single layer of two-dimensional (2D) material consisting of carbon atoms formed in a hexagonal lattice structure. In 2004, Novoselov (2004) won the Nobel Prize in Physics due to their groundbreaking work on graphene (Novoselov et al., 2004). Since then, graphene has attracted great interest because of its important properties, such as thermodynamic stability, mechanical stiffness, and high charge carrier mobility (Obraztsov, 2009). Over the years, great efforts have been made to explore both the physical properties and the applications of graphene. Several examples of the applicability of graphene include the transparent electrode for solar cell devices (Li et al., 2009), the interconnection of electronic devices due to the high carrier mobility (Chen et al., 2010), and the membranes for water desalination (Humplik et al., 2011). However, with graphene being a relatively new material, many applications have not been thoroughly explored.

Pristine graphene was originally obtained by the mechanical exfoliation of graphite in 2004 (Novoselov et al., 2004). Due to the production in small size by using this mechanical exfoliation technique, versatile methods for the synthesis of graphene have been gradually developed. These methods include the oxidation of graphite (Dikin et al., 2007), liquid phase exfoliation (Hernandez et al., 2008; Lotya et al., 2009), chemical vapour deposition (CVD) (Li et al., 2009; Mohsin et al., 2013), and thermal decomposition of silicon carbide (SiC) (Berger et al., 2004; Huang et al., 2008). Among which, transition metal catalyzed CVD has been considered as an inexpensive approach for the synthesis of large-area graphene with high quality. On the contrary, the liquid-phase exfoliated graphene demonstrates an uncontrollable size and a highly defective

University of Malaya

structure. Meanwhile, the epitaxial growth of graphene on SiC substrate requires a high temperature, an ultrahigh vacuum, and an expensive substrate.

## 1.2 Motivation of Research

The growth of graphene without a metal catalyst requires a high temperature ranging from 1100°C to 1650°C (Chen et al., 2013; Chen et al., 2011). Therefore, CVD has been used as a reliable technological process for fabrication of graphene at a lower temperature using the transition metals, such as copper (Cu) (Li et al., 2011; Mattevi et al., 2011) and nickel (Ni) (Lee et al., 2010; Liu et al., 2010). The growth of graphene on the polycrystalline Cu substrate has been regarded as more viable in obtaining the monolayer graphene due to the surface controlled process (Luo et al., 2011). This monolayer graphene growth could be controlled by Cu due to its low carbon solubility (<0.001 atomic %) (Bae et al., 2010; Li et al., 2009). Meanwhile, the growth of graphene on Ni substrate has been observed to grow a few layers of graphene due to the higher solubility of carbon in Ni (>0.1 atomic %) even at a low deposition temperature. However, this catalytic effects could greatly reduce the deposition temperature, as the temperature for carbon to dissolve in Ni is as low as 25 °C (Kwak et al., 2012). Furthermore, the formation of monolayer or bilayer graphene using this technique is limited by the grain size of the crystalline Ni obtained from the thermal annealing of Ni thin film (Kim et al., 2009; Reina et al., 2008).

Despite the ability of metal catalysts to reduce the deposition temperature, the thermal CVD growth of graphene on Cu requires a temperature between 800 °C to 1000 °C and the graphene growth on Ni must undergo an additional step which is the annealing process for Ni treatment. In addition, the CVD technique requires post-growth transfer process from the surface catalyst onto the dielectric substrate. This process not only increases the complexity of the procedure but also causes degradation of the graphene quality as the

University of Malaya

process would inevitably induce defects, impurity, wrinkles, and cracks (Chae et al., 2009; Li et al., 2009). Nevertheless, the high-temperature growth and transferred graphene could influence the performance of the device application and impose a limitation on the choice of substrate.

Defects in graphene which may appear during growth or processing could deteriorate the performance of a graphene-based device, making it almost impossible to work with defect-free or impurity-free graphene. However, the deviation from perfection can lead to other positive effects which could be useful in some applications. For instance, the structural defects in graphene could be tailored to the local properties of graphene and achieve new functionalities, which are relevant to the functional performance of the materials (Jorio et al., 2009; Yan et al., 2008). Recently, graphene has been an ideal material for the functional hydrophobic surface due to its exceptional physicochemical properties for self-cleaning (Min et al., 2008; Zhang et al., 2011), anti-corrosion ( Xu et al., 2009), anti-icing (Cao et al., 2009), drag reduction coating (Shi et al., 2007), and oil-water separation (Feng et al., 2004; Yonglai et al., 2009). However, the wettability properties of graphene, especially that of the CVD graphene, have not been studied extensively.

Based on the previous research, the formation of wrinkles or crumples in graphene has been shown to provide a pathway to introduce a hierarchical structure into the graphene structure, allowing a hydrophobic coating (Kim et al., 2009). Furthermore, the higher OH content in the defective graphene which deposits at a lower temperature significantly impacts the wettability properties of graphene. Moreover, the defects in graphene could also induce magnetic moments which interact ferromagnetically due to the localized unpaired spin (Wang et al., 2008). The magnetic ordering in the graphene indicates its potential to be used in the design of future magnetic nanoelectronic and spintronic

University of Malaya

applications (Goerbig et al., 2009). Despite the weak magnetization being a potential challenge for its practical application, the ferromagnetism in graphene is undeniably an important area for further research.

## 1.3 Research Objectives

This research work focuses on the growth of a large area of transfer-free graphene at a low temperature using Ni catalyst. Plasma enhanced chemical vapour deposition (PECVD) has been used to synthesize the graphene at a relatively low temperature. Instead of annealing the Ni, hot-filament PECVD (HF-PECVD) has been used. The objectives of this research work are:

- To determine the optimum Ni layer thickness required for the growth of a large area of transfer-free graphene grown by PECVD
- To compare the structure, morphology, and chemical bonding properties of graphene layer grown by PECVD and HF-PECVD
- To investigate the effects of deposition time of transfer-free graphene grown by HF-PECVD on the structure, morphology, and chemical bonding properties
- To investigate the effects of the substrate temperature of transfer-free graphene grown by HF-PECVD on the structure, morphology, and chemical bonding properties
- To explore the role of substrate temperature in enhancing the hydrophobicity and magnetic properties of graphene

University of Malaya

## 1.4 Overview of Thesis

The thesis has been written in six chapters. The first chapter introduces this work. In the following chapter (Chapter 2), a literature review of other related works is presented. This chapter consists of four major parts: the first part outlines the structure of graphene, including a brief discussion on the different types of defects in graphene; the second part presents the analytical method related to this work, specifically the Raman spectroscopy; the third part focuses on the review of graphene growth using different techniques, and; the fourth part presents a brief discussion on the wettability and the magnetic properties of graphene.

The experimental and analytical methods are discussed in Chapter 3. This chapter is divided into two parts. Firstly, the details about the setup of the home-built HF-PECVD system, operating procedures of the system, and sample preparation for transfer-free graphene deposition are discussed. Then, the chapter describes the basic operation of the analytical apparatus based on this study, including the calculation used to analyze the data.

Chapter 4 and 5 delineate the results of the characterization of the transfer-free graphene sample. In Chapter 4, the optimum Ni thickness and the effects of Ni thickness on the properties of transfer-free graphene using PECVD are presented. This chapter fulfills the first objective of this research. Chapter 5 is divided into three parts: the first part outlines the comparison of the properties of transfer-free graphene grown from PECVD and HF-PECVD; the second part describes the improvement in the properties of the transfer-free graphene using HF-PECVD by reducing the deposition time, and; the last part defines the optimum substrate temperature in growing high-quality transfer-free graphene and depicts its effects on the hydrophobicity and the magnetic properties of the films.

University of Malaya

Based on the results and discussion in Chapter 4 and 5, this paper aims to establish a conclusive idea regarding the formation of large-area transfer-free graphene using Ni catalyst at a low temperature with HF-PECVD technique. Finally, the conclusion and recommendations for future work are presented in Chapter 6.

University of Malaya

# CHAPTER 2: LITERATURE REVIEW

## 2.1 Structure of Graphene

Zero-dimensional fullerene, one-dimensional nanotubes, and three-dimensional graphite can be produced from graphene by wrapping or stacking. Due to its unique microstructure, graphene has numerous important chemical and physical properties, including a high electron mobility and thermal conductivity (Tian et al., 2016), an ultra-high specific surface area, a superior stiffness (Zandiatashbar et al., 2014), and a great strength. Moreover, it has a semi-integer quantum Hall effect and perfect quantum tunneling effects (Novoselov et al., 2007). These characteristics make graphene the most popular carbon material after fullerene and carbon nanotubes.

Graphene is defined as a single two-dimensional hexagonal sheet of carbon atoms as shown in Figure 2.1(a). The standard plane unit cell vectors are $|a_G| = |b_G| = 2.4589$ Å (Baskin et al., 1955). However, the unit cell contains 2 carbon atoms at (0, 0) and ($a_G/3$, $2b_G/3$) which give a carbon a real density of 3.820 atoms Å$^{-2}$. Graphene bonds are hybridized into $sp^2$ configuration where the three in-plane $\sigma$ bonds are extremely strong, forming the rigid backbone of the hexagonal structure. It is the partially filled $p_z$ or $\pi$ orbitals perpendicular to the plane. These $\pi$ orbitals are responsible for the electron conduction (refer to Figure 2.1(b)). The formation of out-of-plane $\pi$ orbitals due to the interaction between graphene layers or interaction with the substrate could influence the electronic structure of the graphene.

University of Malaya

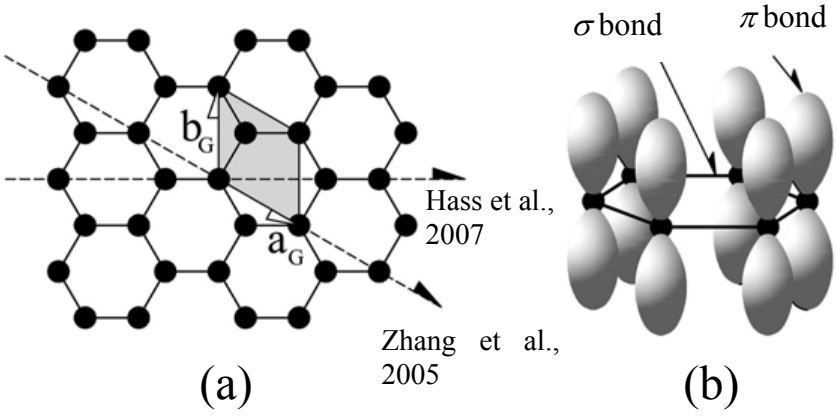


**Figure 2.1: (a) Graphene hexagonal structure of identical C atom. The unit cell (shaded area) consisting of two C atoms is shown along with the standard unit cell vector $a_G$ and $b_G$. The structure of 'armchair' edge (Hass et al., 2007) and the 'zig-zag' edge directions are shown (Zhang et al., 2005). (b) Schematic of the in-plane $\sigma$ bonds and the $\pi$ orbitals perpendicular to the plane of the C sheet. Figure is taken from the (Hass et al., 2008).**

The graphene sheets are known to stack in several ways to form graphite with generic name. As shown in Figure 2.2, the three most common stacking arrangements are the hexagonal (AA stacking), the Bernal (AB stacking), and the rhombohedral (ABC stacking). Among which, Bernal stacking has the lowest energy stacking and it is the most abundant form in a single crystal graphite (Haering, 1958). The Bernal stacking is formed from the stacking of two graphene sheets on top of each other, where one of the z-direction graphene sheet is stacked at 60° to another rotated graphene sheet. The sheets are separated by a distance of $c_G/2$, where $c_G$ = 6.672 Å at 4.2 K and 6.708 Å at 297 K (Baskin et al., 1955). This structure produces two sublattices of the atoms, whereby an A atom is positioned above an A atom in the sheet below or a B atom with no atom below it in the adjacent sheet. In a graphite with the Bernal structure, the overlap of the partially filled $\pi$ orbitals perpendicular to the plane accounts for the weak bonding between the AB sheets. These bonds are sometimes known as the Van der Waals bonds (Schabel et al. 1992).

University of Malaya

The least common form of graphite is the hexagonal AA stacking. This type of stacking arrangement consists of two unrotated sheets separated by a distance of $c_G/2$ perpendicular to the sheets (refer to Figure 2.2). It consists of a single sublattice with two atoms or cells. Meanwhile, the rhombohedral graphite is formed by three graphene sheets with each being separated by $c_G/2$. The middle sheet is rotated relative to the bottom sheet by 60° as in the Bernal graphite and the top sheet has the same orientation relative to the middle sheet but is translated by ($2a_G/3$, $b_G/2$) from the middle sheet. As evident in Figure 2.2, the $c_G/2$ is slightly different for each stacking arrangement. However, the difference is ~0.2 % for the Bernal stacking which is often considered negligible (Charlier et al., 1994).

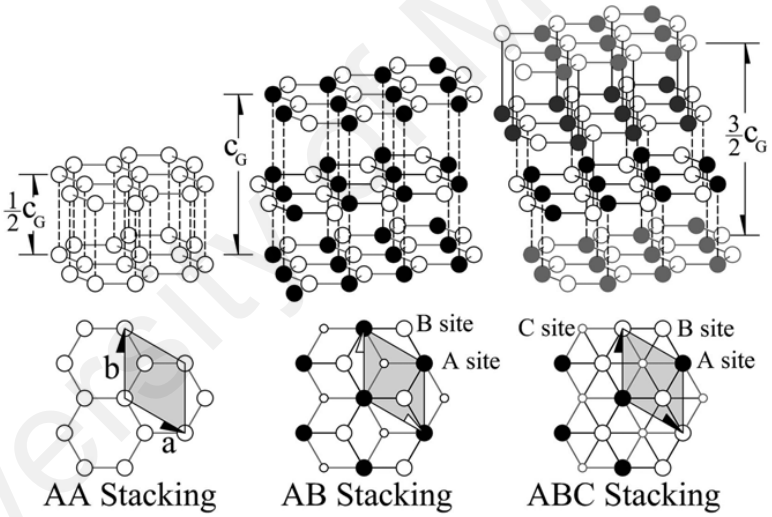


**Figure 2.2: Schematic of graphite structure at different graphene stacking arrangements: (i) Hexagonal AA stacking, (ii) Bernal AB stacking, and (iii) rhombohedral ABC stacking. The shaded area represents the unit cell. Figure is taken from the (Hass et al., 2008).**

The electronic band structure of graphene was first calculated in 1947 by Wallace (Wallace, 1947). The *ab initio* band structure calculation for an isolated graphene sheet is shown in Figure 2.3. The crucial aspect of the band structure occurs at Fermi energy, $E_F$, where the $E$=0 in the plot with an electron momentum near the $K$- or $K'$-point. The hopping of electrons between the two equivalent carbon sublattices A and B (refer to

University of Malaya

Figure 2.1) leads to the intersection of π bands at the zone boundary, '*K*-point'. As illustrated in Figure 2.3(b) and (c), the energy dispersion near the Diract points is linear, $E = \hbar k v_F$, where $v_F \approx c/300$ ($c$ is the speed of light), giving rise to a Fermi surface near $E$=0, which is composed of six Dirac cones. This unique linear dispersion signifies that the effective mass of the electrons is zero near $E_F$. In addition, the linear dispersion has another significant impact on the electron state (below $E_F$) and the hole state (above $E_F$). The electron and hole are represented as quasi-particles connected in a way that is best described by the Diract equation (Guinea et al., 1988; McCann et al., 2006; Peres et al., 2006; Semenoff, 1984; Slonczewski et al., 1958). The electrons and holes belong to the same branch of the dispersion curve as described by the pseudospin $\sigma$ which is parallel to the electron momentum but opposite to the hole momentum. As demonstrated by Figure 2.3 (b), this 'chirality' indicates that the electron is not allowed to travel from *K* to *K'* since the pseudospin is not conserved. This conservation rule gives rise to the ballistic transport observed in graphene (Ando et al., 1998; Frank et al., 1998), which corresponds to the fact that the long-range Coulomb potentials cannot trap the Diract quasi-particles (De Martino et al., 2007). This finding indicates that the coherence lengths can be very large in the epitaxial graphene. For more detailed theoretical explanation, refer to (Katsnelson et al., 2007).

University of Malaya

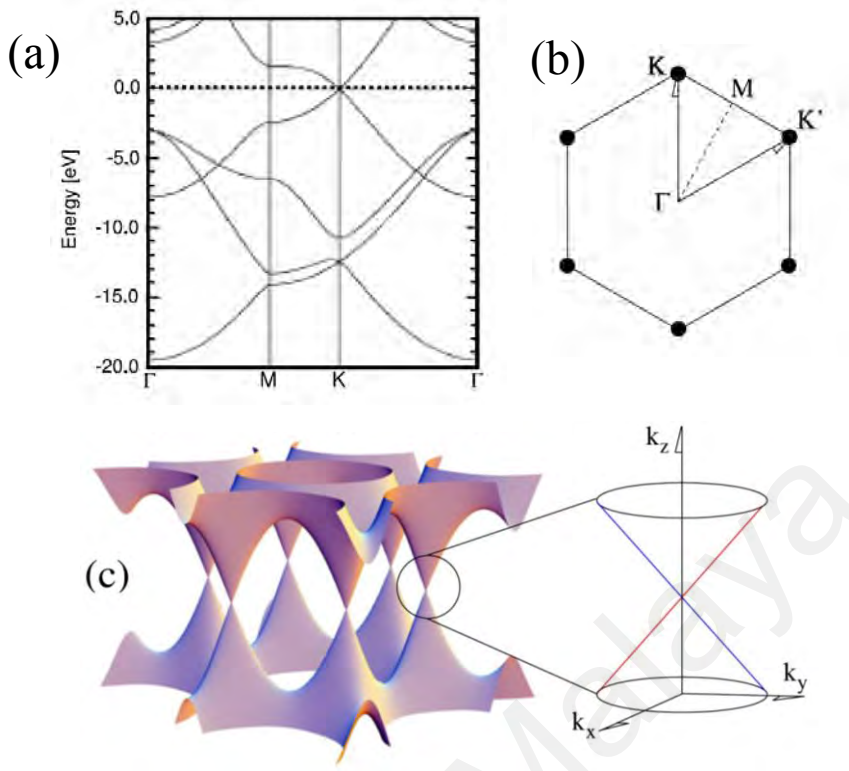


**Figure 2.3: (a) An *ab initio* band structure of graphene calculated from the (Latil et al., 2006), (b) A schematic of the Fermi surface of graphene consisting of a point intersection of Diract cone, (c) Two dimensional tight binding energy surface of graphene with an enlarged image showing the linear dispersion or the Diract cone near the *K*-point (Hass et al., 2008).**

The stacking sequence of graphene layers can alter the band structure by breaking the A and B sublattice symmetry (Guinea et al., 2006; Latil et al., 2006; McCann et al., 2006). For example, the A atoms are bonded to A atoms in the bottom plane, while B atoms have no corresponding atoms in the bottom plane for AB stacking (refer to Figure 2.2). The effects of this stacking pattern on the band structure normally observed in the multilayer graphene, are demonstrated in Figure 2.4. In both the Bernal and the rhombohedral stacking, the weak inter-planar interaction breaks the AB symmetry, producing the bonding $\pi$ and $\sigma$ states and the anti-bonding of $\pi^*$ and $\sigma^*$ states. As a result, the splitting of a band is observed near the Diract point, corresponding to the change in the energy dispersion that is no longer linear.

University of Malaya

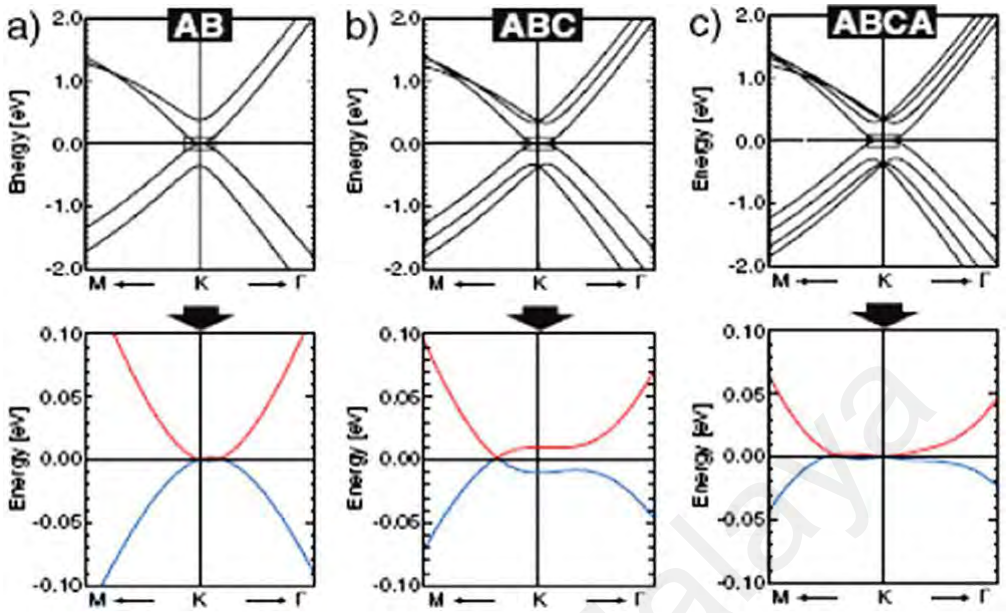


**Figure 2.4 : Ab initio band structures near K-point for (a) AB stacking, (b) ABC stacking and (c) ABDA stacking. Bottom panels show the band crossing near $E=E_F$. (Hass et al., 2008).**

## 2.2 Defects in Graphene

Defects in the graphene are inevitable despite its outstanding electronic and mechanical properties with a high perfection of the atomic lattice. The introduction of defects cannot be avoided especially during the growth process due to the preparation method, temperature, and environment. The common methods of preparation can be divided into two categories, which are the CVD and the exfoliation method. Different preparation methods introduce various defects. In relation to the CVD method, topological defects are often introduced, mainly because of the dissolution technologies which are not mature. During the transferring process, the structure of the graphene may experience damage, such as overlapping or rupture. Furthermore, the choice of substrates has a certain impact on the graphene defects. The commonly used substrates are copper (Cu), silicon (Si), and nickel (Ni). These defects have a great impact on the performance as the performance of reality is far below the theoretical value.

University of Malaya

Essentially, there are two types of defects in graphene, namely the point defects and the one-dimensional line defects. It is well-known that the defects are not always stationary. Their migration reflects an important influence on the properties of the defective crystal and is usually governed by an activation barrier which depends on the types of defects.

### 2.2.1 Stone-Wales Defect

A simple example of graphene defect is the Stone-Wales (SW) defect (Gass et al., 2008). The graphene lattice can be reconstructed by forming non-hexagonal rings which do not involve any removed or added atoms. As shown in Figure 2.5, four hexagons are transformed into two pentagons and two heptagons by rotating one of the C-C bonds by 90°. This defect has been demonstrated to have a formation energy of 5 eV (Meyer et al., 2008).

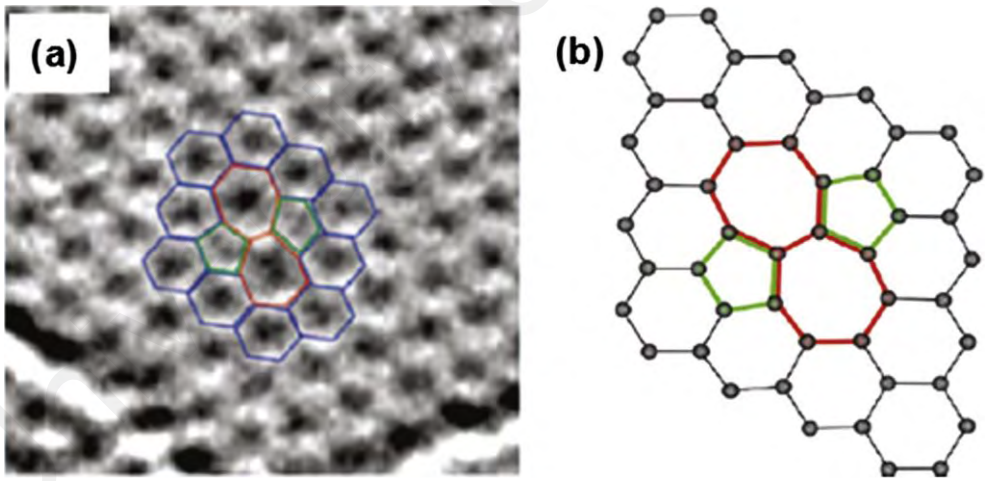


**Figure 2.5: Figure of Stone-Wales defects taken from (a) TEM image and (b) atomic structure as obtained from the Density functional theory (DFT) calculation. Figure is taken from (Liu et al., 2015).**

### 2.2.2 Single Vacancy

Single vacancy (SV) defect is one of the simplest defects in materials. This defect is formed from the missing of one lattice atom. Figure 2.6 shows an example of the SV

defect of graphene observed by TEM image (Meyer et al., 2008). This defect undergoes a Jahn-Teller distortion which leads to the saturation of two of three dangling bonds towards the missing atom. The remaining dangling bond due to geometrical reason leads to the formation of five-membered and nine-membered rings.

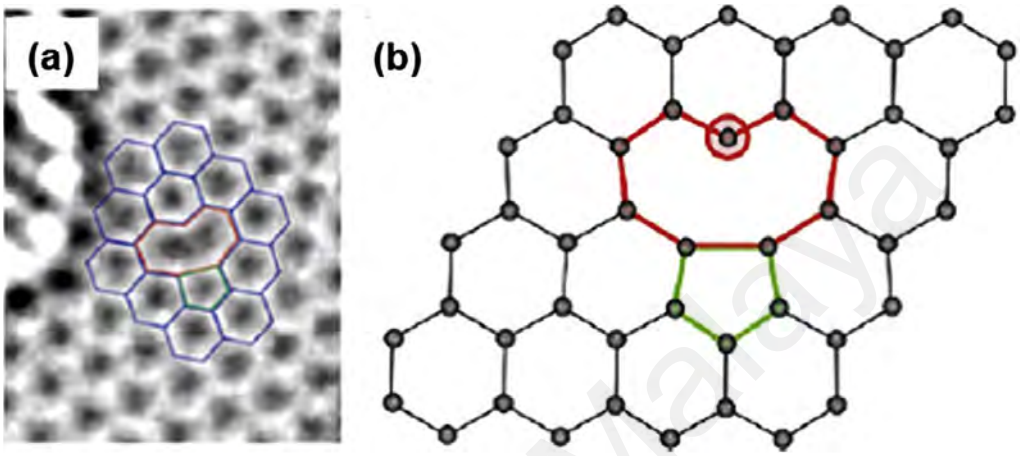


**Figure 2.6 : Single vacancy (a) as seen in TEM image (b) an atomic structure determined from the DFT calculation (Liu et al., 2015).**

### 2.2.3 Multiple Vacancy

Multiple vacancy can be created by the coalescence of several vacancies. For example, double vacancy (DV) may be created from the coalescence of two single vacancy (SV) or by removing two neighboring atoms. Two pentagons and one octagon are formed, instead of four pentagons, in a perfect graphene which result in the absence of a dangling bond in a fully reconstructed DV. The atomic network remains coherent with small perturbations in the bond lengths around the defects. This defect indicates that the simulated formation energy, $E_F$ of the DV is in the same order as the SV which is about 8 eV (Krasheninnikov et al., 2006; Liang et al., 2014). As two atoms are missing in the DV, the energy per missing atom (4 eV per atom) is much lower than that in the SV. Hence, DV is thermodynamically favored over the SV. Moreover, the removal of more than two atoms may be expected to result in a larger and more complex defect configurations. In general, the even number of missing atoms are more energetically

University of Malaya

favored because they allow complete saturation of dangling bond over the structure, whereas an open bond remains when there is an odd number of missing atoms (Kotakoski et al., 2006).

### 2.2.4 One Dimensional Defects

This type of defects has been observed in various experimental studies of graphene (Červenka et al., 2009; Coraux et al., 2008; Lahiri et al., 2010). Generally, line defects are tilt boundaries which separate two domains of different lattice orientations with the tilt axis normal to the plane. Such defects can be described as a line of reconstructed point defects with or without the dangling bonds (Ansari et al., 2010), as shown in Figure 2.7. For example, the domain boundary has been observed to appear due to lattice mismatch in graphene grown on Ni surface (Lahiri et al., 2010). Such defects can be formed by aligning (5-8-5) divacancies along the zig-zag lattice direction of graphene.

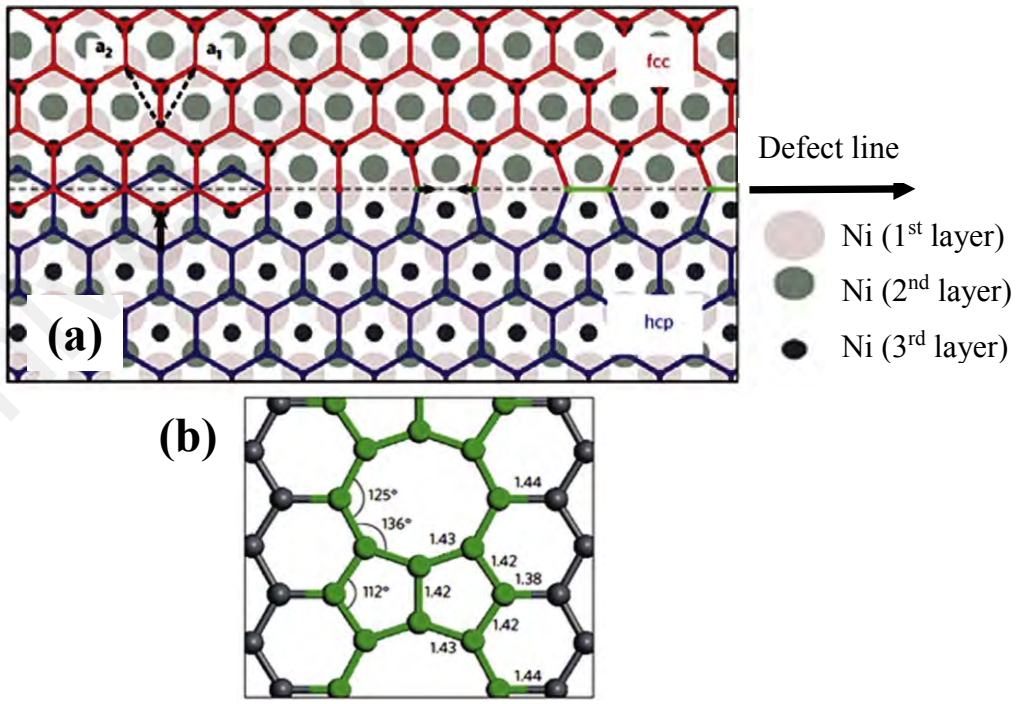


**Figure 2.7 : The grain boundary defects structure consisting of pentagon-pairs and octagon in graphene grown on Ni, and (b) the DFT relaxed geometry of the defect structure. (Lahiri et al., 2010).**

University of Malaya

### 2.2.5 Edge Defects

The graphene layer is terminated by edges with an atom being passivated with the hydrogen atoms or free. There are two forms of the graphene edges, namely the armchair and the zig-zag orientation. A defective edge could appear due to the local changes in the reconstruction or due to a substitution or removal of carbon atoms from the edge. For example, the removal of one carbon atom from a zig-zag edge leads to one pentagon in the middle of a row of hexagons at the edge. As illustrated in Figure 2.8, reconstruction of the other edge, in turn, forms a different combination of pentagons and heptagons. Moreover, the hydrogen atoms and other chemical groups that can saturate the dangling bonds at the graphene edge may also be considered as disorder.

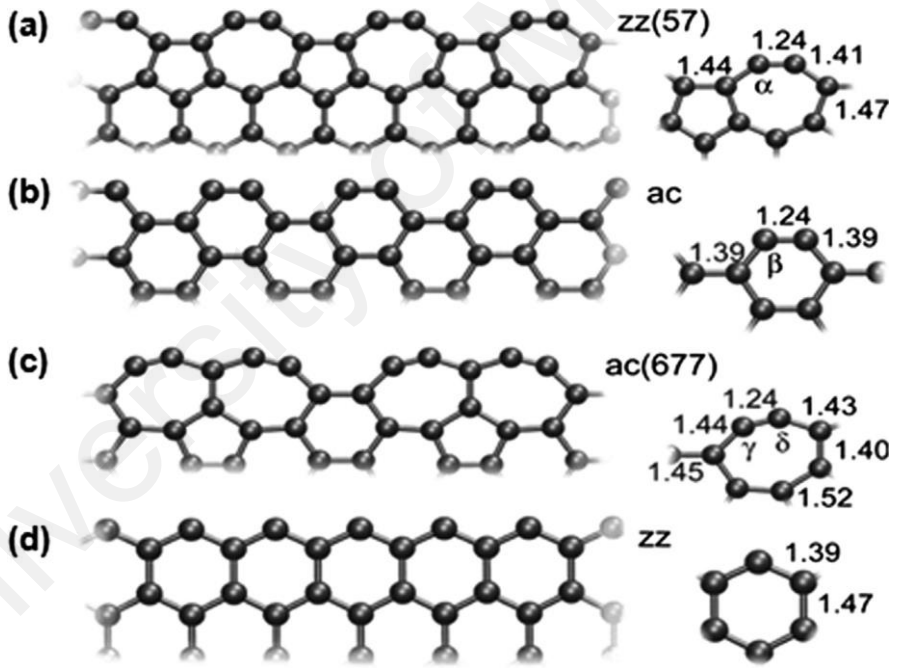


**Figure 2.8 : The edge reconstructions in graphene: (a) reconstructed zig-zag edge, (b) armchair edge, (c) reconstructed armchair edge and (d) zig-zag edge (Koskinen et al., 2008).**

University of Malaya

## 2.3 Defect-induced Double Resonant Raman Mode in Graphene

### 2.3.1 Double Resonant Raman Scattering

Double resonant Raman scattering is a second-order process which involves the scattering of a phonon and a defect (Thomsen et al., 2000; Venezuela et al., 2011). It involves a phonon with $q \neq 0$. The momentum conservation is guaranteed by the elastic scattering of either the hole or the electron with a defect in the phonon-defect process. The scattering process is divided into four steps: (i) initially, the incoming photon $\hbar\omega_i$ is absorbed which then resonantly excites an electron-hole pair; (ii) the excited electronics are then scattered by a phonon with the wave vector $q$; (iii) equally, the hole is scattered by a phonon with the wave vector $-q$, and; (iv) the electron-hole pair recombines and emits a photon with the energy $\hbar\omega_i$. This double-resonant Raman can be separated into either inter- or intra-valley double resonant scattering. While inter-valley scattering describes a scattering process of two inequivalent $K$ points, intra-valley refers to a scattering process between the electronic states at the same $K$ point. Figure 2.9 shows a schematic illustration of the inter-valley and intra-valley double-resonance process in a graphene.

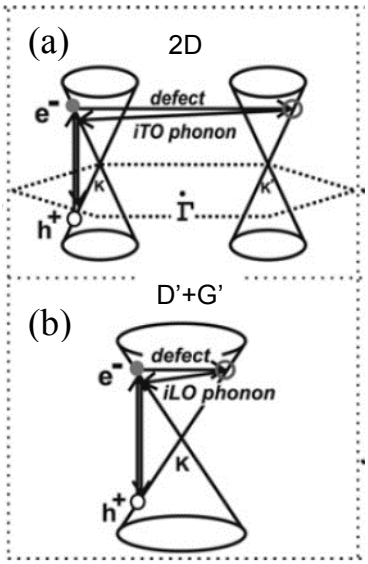


**Figure 2.9 : (a) Second-order DR process for the 2D band (inter-valley process) and (b)D'+G' band (intra-valley process) (Malard et al., 2009a).**

University of Malaya

### 2.3.2 Raman Spectroscopy of Graphene

As the unit cell of graphene consists of two inequivalent A and B atoms, the phonon dispersion splits up into six branches: three from the acoustic and another three from the optical branches. Figure 2.10 portrays the phonon dispersion of a single-layer graphene along the high-symmetry direction in the first Brillouin zone. These high-energy optical phonon branches (LO and TO) degenerate at Γ, exhibiting the $E_{2g}$ symmetry. Away from the Γ, the LO phonon branch observes an overbending. As the phonon dispersion of the graphene presents Kohn anomalies at certain high-symmetry points in Brillouin zone, the LO branch exhibits a Kohn anomaly at the Γ point, while the TO branch is affected by a Kohn anomaly at K (Piscanec et al., 2004). On the other hand, there are twelve branches of phonon spectrum in the bilayer graphene with double atoms in the unit cell. Most of these branches degenerate throughout the Brillouin zone. The TO phonon branches split along the Γ-*K* direction while the LO and TO phonon branches split up into a symmetric Raman-active ($E_g$ symmetry) and an anti-symmetric infrared-active vibration (*Eu* symmetry) at the Γ point.

The Raman spectra of monolayer and bilayer graphene are composed of several characteristic peaks. An example of the Raman spectra for graphene is shown in Figure 2.11. In all Raman spectra, a peak around 1580 $cm^{-1}$ can be identified with the degenerated LO/TO Γ-point vibration. This peak is characteristic for all types of graphitic or $sp^2$ hybridized structure of carbons films and it is referred to as the G mode. Another prominent feature is the 2D mode located at ~2650 $cm^{-1}$ which originates from a double-resonant inter-valley scattering process with two TO phonons from the border of the Brillouin zone around the *K* points (Thomsen et al., 2000). The peak exhibits nearly a single-Lorentzian line shape for the single-layer graphene. However, the line shape changes drastically as the number of the layer increases. A broader peak is observed, representing the presence of multiple peaks for $N \geq 2$ (N = number of layer) and reflecting

University of Malaya

the evolution of the electronic bands around the *K* point (Ferrari et al., 2006). Additionally, there is an extra peak observed around 3240 $cm^{-1}$ which is represented by the D'+G' mode in the Raman spectra. This mode results from an intra-valley scattering process with two LO phonons from the overbending LO region near the Γ point. In addition to the two-phonon double resonant Raman mode, there is a double-resonant phonon defect scattering process. The defect-induced Raman mode is referred to D, D', and D'' mode which are located at ~1350 $cm^{-1}$, ~1620 $cm^{-1}$, and ~1100 $cm^{-1}$, respectively.

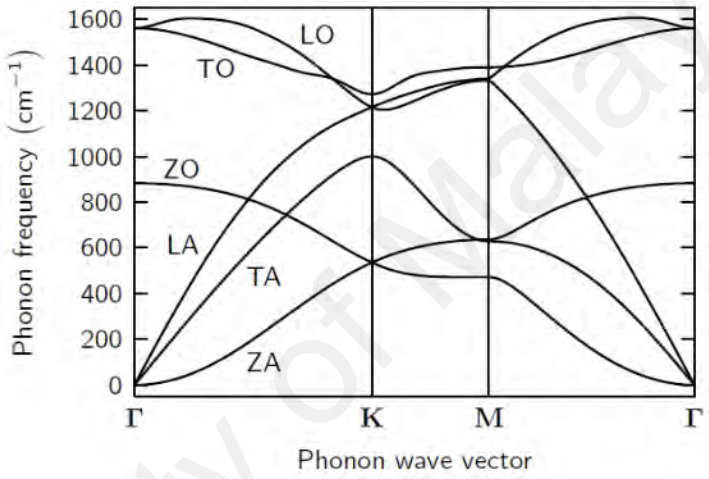


**Figure 2.10 : Phonon dispersion of a single-layer graphene along the Γ-K-M-Γ high symmetry from the LDM calculation (Herziger, 2015).**

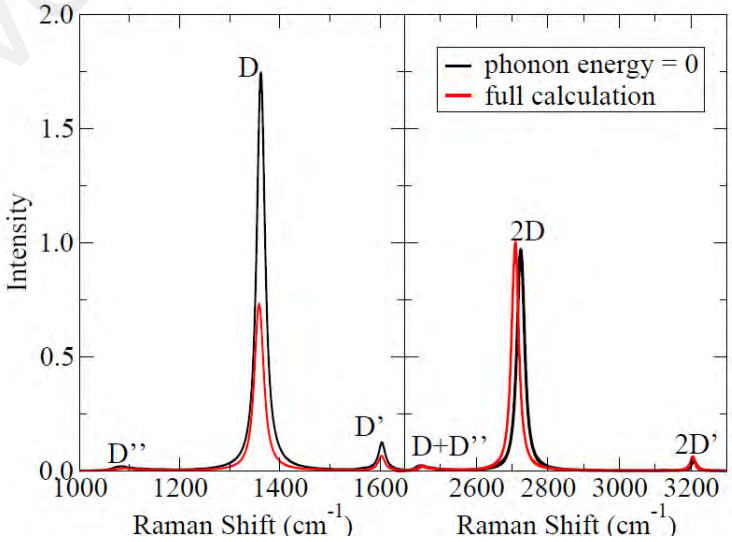


**Figure 2.11 : An example of Raman spectra for graphene (Venezuela et al., 2011)**

University of Malaya

## 2.4 Growth of Graphene

In relation to the graphene synthesis, several techniques have been developed to produce good quality and large-scale films that are suitable for applications. The graphene with the best electronic properties thus far has been produced via the mechanical exfoliation from the Highly Ordered Pyrolytic Graphite (HOPG), which is 10 micrometers in size (Novoselov et al., 2004). Furthermore, graphene can be produced by the high-temperature annealing of a single crystal SiC (Emtsev et al., 2009), chemical reduction of the graphite oxide (Tung et al., 2009), and chemical vapour deposition (CVD) on the metal substrate (Li et al., 2009). Among the various deposition techniques, CVD appears to have the greatest potential of becoming a adoptable technology. It has been one of the most used fabrication technique for thin film and it is known to be cost-effective in producing a scalable graphene.

### 2.4.1 Growth of PECVD Graphene

CVD is a technique of thin film deposition on a substrate from vapour species through the chemical reaction (Miao et al., 2011). It is an easy-to-control deposition process as compared to other techniques. Moreover, CVD on a transition metal substrate has been an important technique in preparing and producing graphene for applications ever since the method was first reported in 2008. During the deposition process, the hydrocarbon precursor is decomposed to a carbon radical on the metal substrate at a high temperature. Ni and Cu substrates were first used in the early studies on CVD graphene synthesis (De Arco et al., 2009; Reina et al., 2008; Yu et al., 2008). These studies were followed by other research works which further explored the graphene growth using a variety of transition metal substrates (Coraux et al., 2009; Sutter et al., 2009; Sutter et al., 2008).

On the other hand, PECVD technique has a similar process to CVD but with a lower deposition temperature. The first study on the single to few-layer graphene by PECVD



University of Malaya

was reported in 2004 (Wang et al., 2004; Jianjun et al., 2004). A radio frequency (rf) of PECVD system was used to synthesize the graphene films on the various substrate. This technique has gained popularity among other researchers since then due to the low temperature and the simplicity of the deposition process via PECVD (Hiramatsu et al, 2004; Peng et al., 2013; Qi et al., 2011; Wang et al., 2004). In PECVD, graphene is grown onto a substrate from the vapour species through chemical reactions by the dissociation of gas. The use of capacitive coupling between the electrodes excites the reactant gases into a plasma, which then induces a chemical reaction. Thus, with a good control of the plasma chemistry, the growth temperature could be lowered.

### 2.4.2 Catalyst used in Graphene Growth

In the process of growing graphene without a catalyst, the formation of a large-area graphitic structure requires a high reaction temperature up to 2500 °C. This high reaction temperature requires a special setup of deposition system and substrate. In addition to the undesirable needs of a high deposition temperature, high energy barrier leads to a sensitive reaction rate to temperature which makes it difficult to control the graphene growth. As the film quality is determined by the reaction kinetics, the high energy barrier directly leads to the difficulty in controlling the film quality.

The function of a catalyst is to lower the energy barrier of the reaction. The introduction of catalyst in the graphene growth lowers not only the energy barriers for the pyrolysis of the precursors but also for the graphitic structure formation. Catalysts are usually metal, which may have finite carbon solubility. In this work, Ni which has non-negligible carbon solubility has been used as the catalyst (Natesan et al. 1973). The dissociated carbon atoms on the Ni surface may dissolve into a bulk during deposition due to their finite solubility. These dissolved carbon atoms precipitate onto Ni surface as temperature drops during the cooling process. As a result, a large amount of carbon source

University of Malaya

is absorbed on the Ni foils, forming a thin graphite rather than a graphene (Obraztsov et al., 2007; Reina et al., 2008). To solve this problem, a thin layer of Ni less than 500 nm could be deposited on the $SiO_2$/Si substrate to control the amount of dissolved carbon, while the speed of the cooling rate could suppress the formation of the thin graphite.

### 2.4.3 Growth Mechanism of Graphene using Ni Catalyst

Formation of graphene on the Ni catalyst using CVD has gained popularity as a scalable and cost-effective approach (Karu et al., 1966; Kim et al., 2009; Reina et al., 2008; Yu et al., 2008). Specifically, the polycrystalline Ni film has been shown to be a good substrate for this type of graphene growth. Most of the researchers have reported the synthesis of few-layer graphene using this technique. In general, graphene is formed on the Ni surface from the carbon atom surface segregation. The decomposed carbon atoms diffuse into the Ni and segregate on the nucleation sites of the Ni surface during the cooling period. Figure 2.12 illustrates the growth mechanism of graphene on a Ni surface during the synthesis.

The formation of such multi-layer graphene is associated with different factors, including the defects and the grains boundaries on the polycrystalline Ni substrate. It has been reported that the segregation and precipitation of carbon tend to happen at the grains boundaries of Ni (Reina et al., 2009; Shelton et al., 1974). The grains boundaries could be good nucleation sites for carbon segregation as the grains can act as active sites for the interaction of carbon atoms and lattice vacancies (Reina et al., 2009). Therefore, the formation of monolayer or bilayer graphene is limited by the grain size of the Ni (Zhang et al., 2010). To overcome this problem, the Ni can be heated to above 1000 °C to increase the grain size where the uniform grains boundaries provide a smooth surface for a uniform graphene formation (Garcia et al., 2011; Kim et al., 2009; Kwak et al., 2012).

University of Malaya

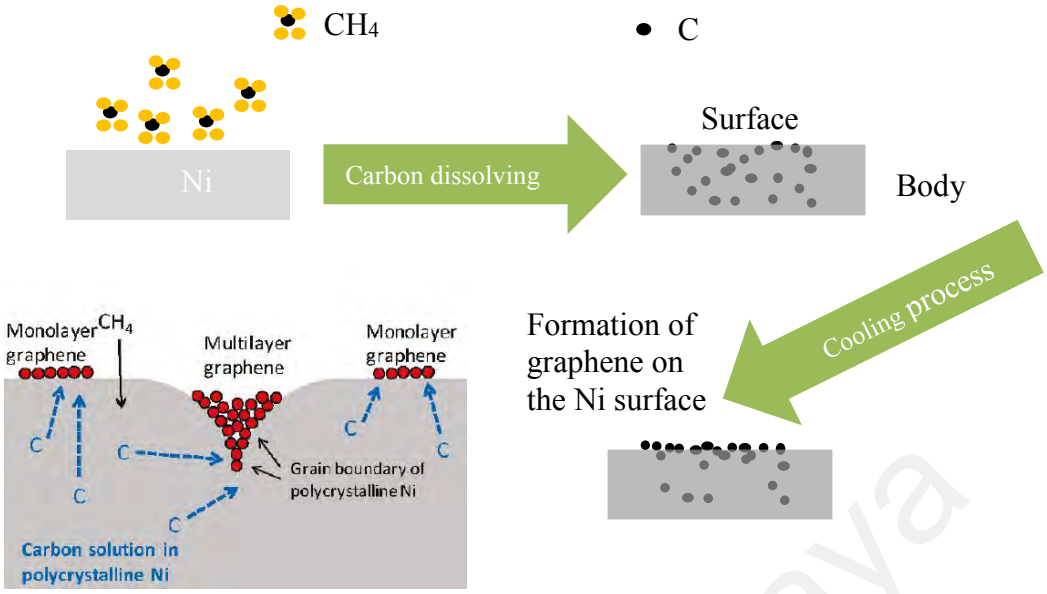


**Figure 2.12: Schematic diagrams of graphene growth mechanism on polycrystalline Ni surface (Zhang et al., 2010).**

### 2.4.4 Growth of Transfer-Free Graphene

The synthesis of transfer-free graphene on the dielectric substrate has long been an important research area among the researchers (An et al., 2016; Macháč et al., 2017; Othman et al., 2015; Pan et al., 2013). The reported works on the synthesis of transfer-free graphene were initiated by Yan et al (2011) in early 2011 (Yan et al., 2011). In the study by Yan et al (2011), transfer-free graphene was directly grown on an insulating substrate from a solid carbon source such as polymer films and Ni film. The polymers were deposited on the insulating substrate using a spin coater before being capped with a Ni layer which acted as the catalyst for graphene formation. The carbon source was then transformed into a bilayer graphene film on the insulating substrate after being annealed at 1000 °C. Subsequently, the Ni layer was removed by dissolution, affording the bilayer graphene on a substrate without any trace of polymer left from the transfer process. A schematic step of the graphene growth and the spectroscopic analysis is shown in Figure 2.13. The bilayer graphene was grown using this technique at an elevated temperature with a Ni film on top of or below the polymer films (Peng et al., 2011; Yan et al., 2011).

University of Malaya

A year later, another similar study on the transfer-free graphene synthesis was conducted by Kwak et al (2012) using a different carbon source (Kwak et al., 2012). In the study, a Ni film was deposited on the substrate and a solid carbon was then deposited on top of the Ni. A composed paste of graphite powder dispersed in ethanol was used as the carbon source. A pressure of 1 MPa was uniformly applied to the sandwiched layers using mechanical clamping to ensure an efficient contact at the C-Ni interface and to stimulate the C-C bond breaking on the Ni surface. The samples were then annealed for a short period at a temperature of 25 °C to 260 °C. Following the graphene growth, the C-Ni diffusion couple was etched away using the chemical solution, leaving behind the graphene film on the substrate. The schematic step and analysis of the study are presented in Figure 2.14.

Naturally, the synthesis of transfer-free graphene using a simpler technique has gained much interest among the researchers (An et al., 2016; Othman et al., 2015). Following the study by Kwak et al (2012), Ni film has been used as the catalyst or buffer layer by most researchers for the synthesis of transfer-free graphene. Its popularity is due to the ability of Ni to act as a catalyst at a low temperature. Moreover, it can be dissolved easily in the acidic solution for an etching process.

University of Malaya

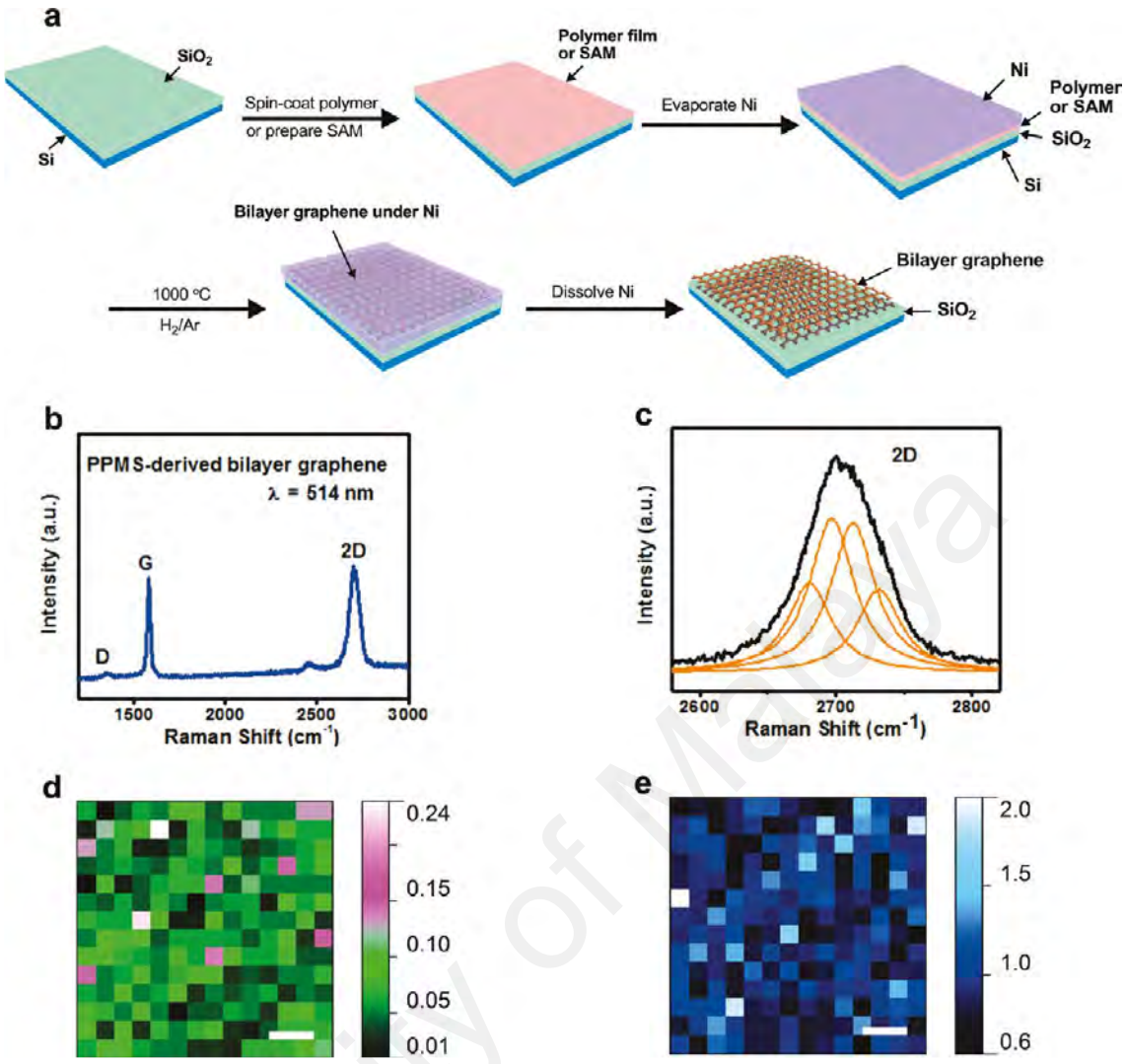


**Figure 2.13: (a) Synthesis of transfer-free bilayer graphene, (b) Raman spectrum, (c) and (d) Raman mapping of bilayer graphene (Yan et al., 2011).**

University of Malaya

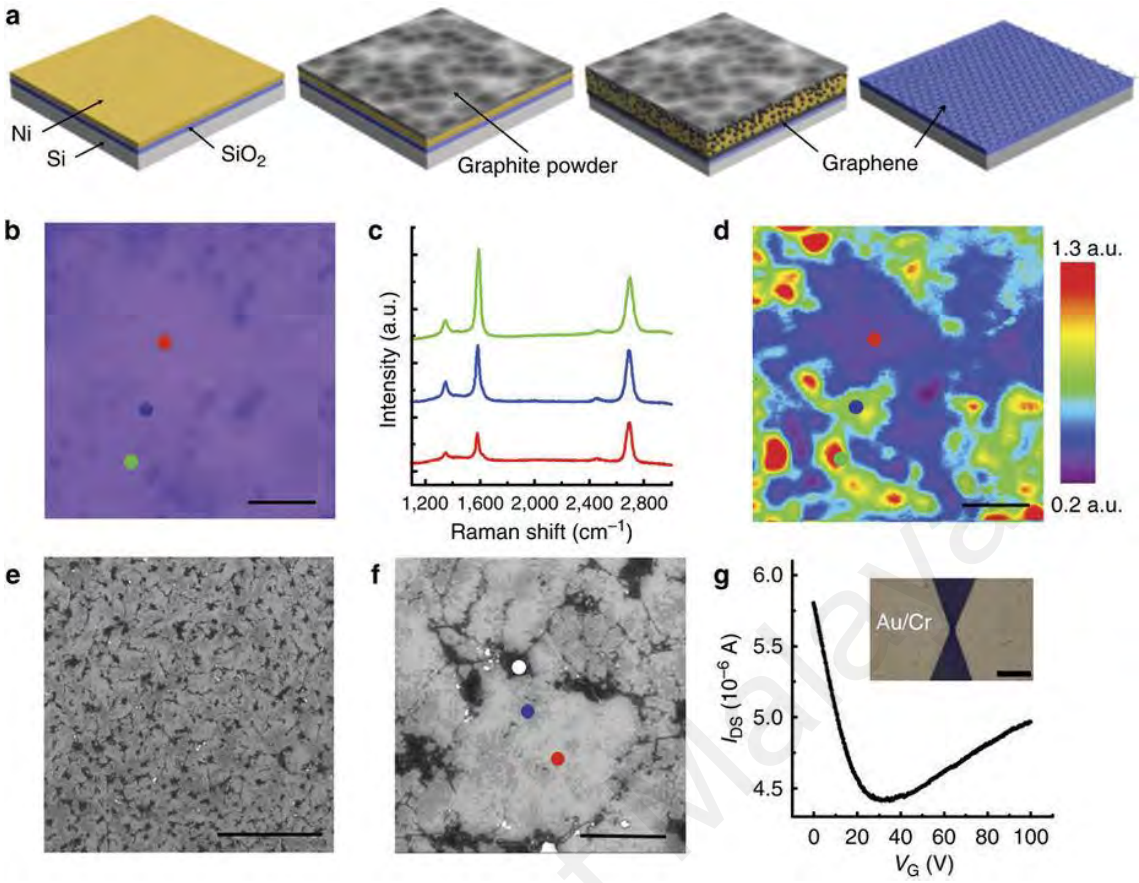


**Figure 2.14: (a) A schematic diagram of direct deposition graphene film on non-conducting substrates, (b) optical microscopy image, (c) Raman spectra, (d) Raman mapping, (e) SEM image (f) higher magnification of SEM image and (g) $I_{DS}$-$V_G$ curve of back-gated FET device (Kwak et al., 2012).**

## 2.5 Wettability of Graphene

Wettability behavior is determined by the intermolecular interactions between the liquid and the substrate. The stronger the liquid is attracted to the substrate, the wider the spread of the liquid drop and vice versa. There have been several studies regarding the water-graphene interaction which could be important if the graphene is used in a conformal coating. The conformal coating of the graphene could be a new class of conductive super-hydrophobic surfaces with possible uses in various applications (Han et al., 2008; Sansotera et al., 2010). The number of graphene layers influences the wetting properties of the graphene films surface. A monolayer graphene coating results in only ~1 to 2 % increase in the contact angle as compared to the bare substrate. For example, a

University of Malaya

baseline Cu has a water contact angle of ~85.9° which increases by ~0.7 % to 86.2° for the monolayer graphene (Rafiee et al., 2012). This result indicates that monolayer graphene coatings offer wetting transparency to the underlying substrate. The contact angle continues to increase gradually as the number of layer increases. The water contact angle finally saturates at the bulk graphite value of ~90.6° for graphene more than six layers.

In general, the wettability of a film coating is strongly influenced by its chemical composition and its geometric structure. Several experimental and modeling studies have focused on exploiting the superhydrophobicity of graphene (Hsieh et al., 2008). One of the techniques is by dispersing the graphene sheet which is formed from the thermal exfoliation of graphite oxide on a substrate using the high-power ultrasonication in acetone. The acetone becomes attached preferentially at the defective sites of graphene which are mostly formed at the graphene edges. The chemisorption of acetone in graphene leads to the carbon-hydrogen bond which is hydrophobic in nature, and hence the attachment of terminal methyl groups which imparts a net hydrophobic character of graphene (Ellis et al., 2003). Another method to improve the hydrophobic behavior of the graphene is by increasing the graphene surface roughness (Hsieh et al., 2011; Hsieh et al., 2008). The growth of nanosheets graphene forms voids between the graphene sheets which generate secondary roughness in the graphene. These graphene sheets display a two-dual roughened surface in the hierarchical structure which makes it difficult for water to wet the graphene surface. This situation introduces an air pocket into the roughened surface, which is explained by the Cassie model (Hsieh et al., 2008).

University of Malaya

## 2.6 Magnetic Properties in Graphene

Magnetism is not common for carbon materials. However, a newly introduced carbon-based magnetic material has extended the limits of technologies, particularly in the design of single molecular magnets and spintronic devices (Adams et al., 2012; Falicov et al., 1990; Yazyev, 2010). Initially, magnetism in graphene was discovered from the materials of graphene oxide (Wang et al., 2008). The observed magnetic behavior in this film was explained in term of the defects in the graphitic network, such as vacancies defects (Andriotis et al., 2003), interstitials (Yazyev, 2008), carbon adatoms (Lehtinen et al., 2003), and atoms at the edges of graphitic nano-fragments with dangling bonds either passivated with hydrogen atoms or free. Such defects have local magnetic moments due to the localized unpaired spin. As a result, ferromagnetism has been predicted and observed in such graphene and graphite films.

The presence of point defects in the graphene lattice, such as the introduction of hydrogen chemisorption defects, vacancy defects, and edges defects, leads to the graphene formed by H plasma process or high-energy ions irradiations (Xia et al., 2008). These defects play an important role in the generation of the robust ferromagnetism and saturation magnetization in graphene. In general, the H adatoms release unpaired electrons by breaking the C=C bond and creating the C-H bonding. The bonding of H and C atoms results in a removal of the $\pi$ orbital which leads to the transition from $sp^2$ to $sp^3$ hybridization (Ruffieux et al., 2002). It also creates $sp^3$ type defects which introduce the local sublattice imbalance and unpaired spin electrons (Ruffieux et al., 2002). The H chemisorption defects induce the strong ferromagnetism when the defects are located at the same sublattice. Theoretical calculations suggest that H maintains the magnetic moment of the defects and gives rise to a macroscopic magnetic signal (Lehtinen et al., 2004).

University of Malaya

Moreover, based on the Density Functional Theory (DFT), the configurations of the graphene also influence the magnetic moments in the graphene (Ferro et al., 2008). The results obtained in this theoretical calculation attribute the source of magnetism to the localized electronic states that are spin-polarized and occur at the level of Fermi energy. It is a case of the nanostructure graphene where the edge of the honeycomb lattice in the so-called "zig-zag" configuration could introduce a magnetic moment due to the spin-polarized edge state. The net spin moment in the zig-zag-edged nanosheet results from the topological frustration of the $\pi$ bonds (Wang et al., 2008). Meanwhile, the graphene edge with the arm-chair configuration indicates zero magnetic moment. For this case, the armchair edges open a gap which varies with the ribbon width (Son et al., 2006). This structure is semiconducting and has no magnetic order. Figure 2.15 shows the band spectrum of the armchair and the zig-zag edges in graphene.

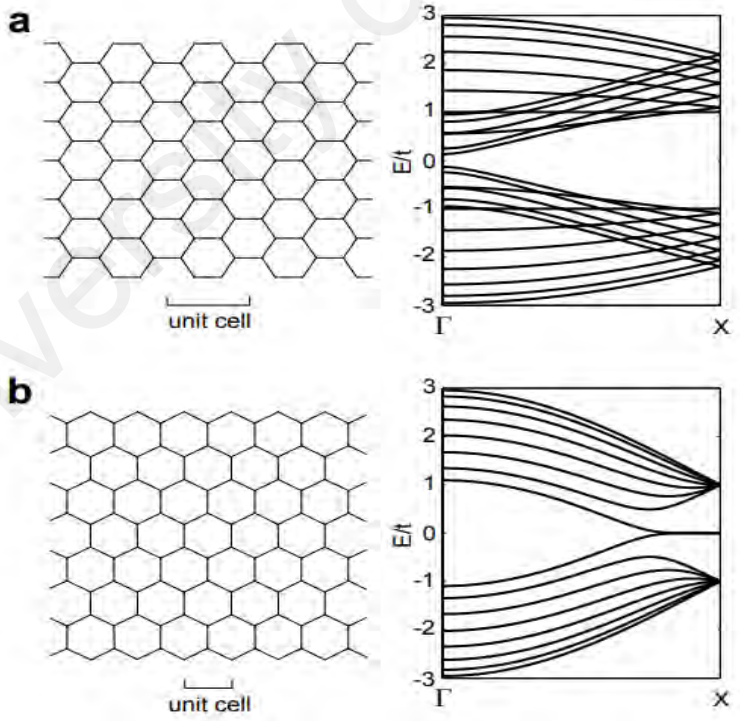


**Figure 2.15: Atomic structure and electronic band spectra of armchair edges (a) and zig-zag edges (b) in graphene (Yazyev, 2010).**

University of Malaya

# CHAPTER 3: EXPERIMENTAL AND ANALYTICAL TECHNIQUE

## 3.1 Introduction

This chapter presents the setup of home-built chemical vapour deposition (CVD) system. The CVD system can be easily modified to plasma-enhanced chemical vapour deposition (PECVD) or hot-filament plasma-enhanced chemical vapour deposition (HF-PECVD) subjected to the required deposition technique. The details of the CVD reactor, vacuum system, heating elements, plasma generator, and gas management are described in the chapter. In addition, this chapter elaborates the cleaning procedure of the substrate and the preparation of the Ni catalyst. Moreover, the deposition parameter and procedures of graphene growth are summarized in this chapter. The general characterization techniques utilized to study the morphological, structural, chemical bonding and element composition properties of Ni catalyst and graphene are briefly discussed in this chapter.

## 3.2 HF-PECVD System Setup

The CVD is a process of depositing thin films from a gas state (vapour) to a solid state (film) on the substrate. The schematic diagram and photograph of the home-built HF-PECVD system are illustrated in Figure 3.1 and Figure 3.2, respectively. The system consists of CVD reactor, vacuum system, heating components, plasma generator and gas regulating system. Notably, the function of the system can be changed by modifying some parts of the system subjected to the requirements for deposition.

University of Malaya

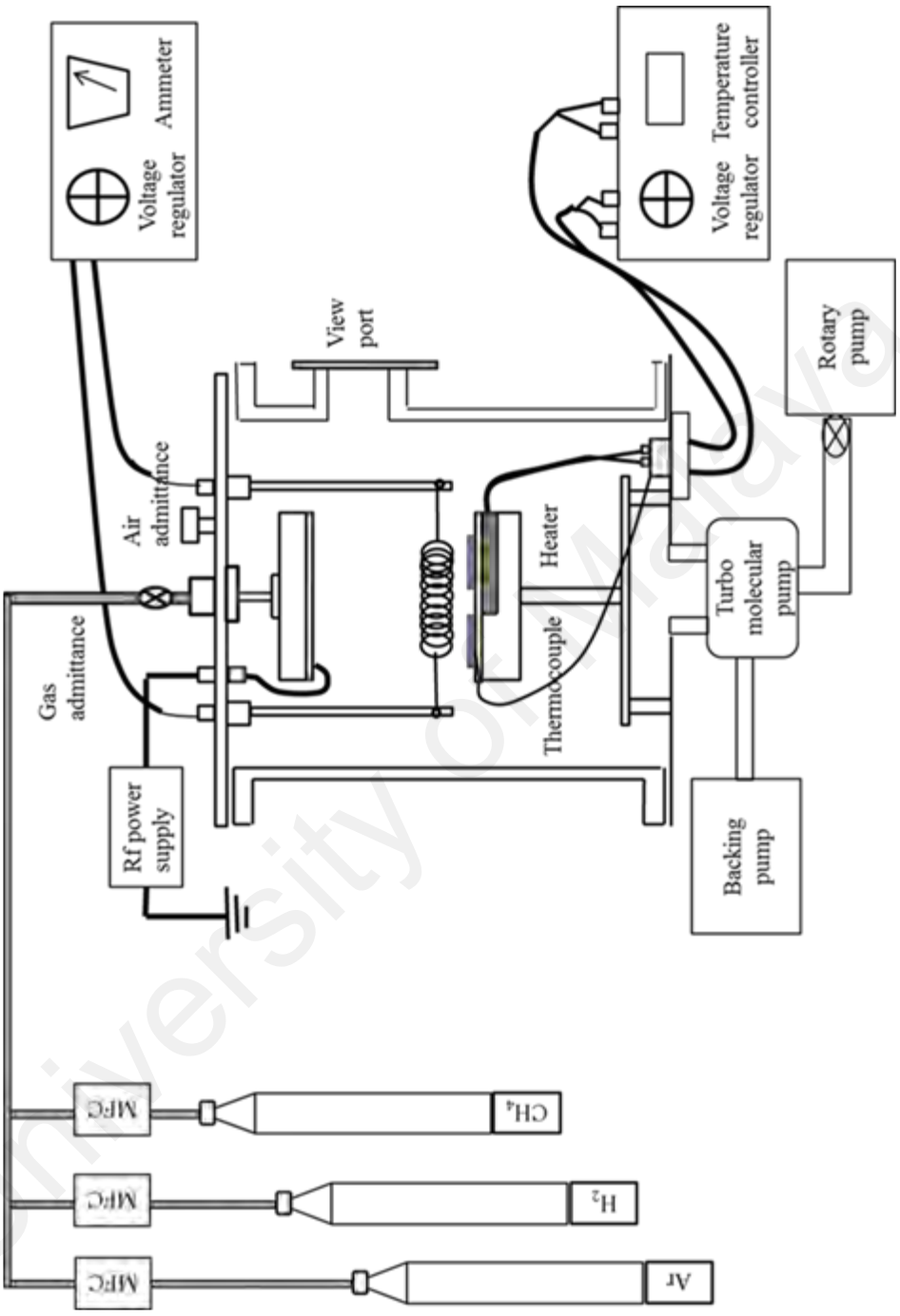


**Figure 3.1: Schematic diagram of HF-PECVD system.**

University of Malaya


**Figure 3.2: Photograph of (a) HF-PECVD system, (b) pressure meter display (c) mass flow controller (d) CVD chamber (e) RF regulator and temperature controller, and (f) vacuum pump.**

### 3.2.1 CVD Reactor

The CVD reactor consists of three parts including chamber, shower head, and substrate holder. The chamber is made of cylindrical stainless steel with diameter of 30 cm and height of 40 cm. A glass viewport on the chamber body is designed for viewing inner part of the chamber during the deposition process. Additionally, it is also a place for the optical pyrometer to read the filament temperature throughout hot-filament deposition. In the reactor chamber, a stainless-steel showerhead is placed on top of the system, where it is designed to disperse the precursor gases that flow from the gas inlet to the substrate. A stainless-steel substrate holder, which is designed for placing four substrates is located below the showerhead. A heater rod and thermocouple are attached to the substrate holder for the heating process. Moreover, the reactor chamber is well-sealed with Viton O-rings and tightly screwed to achieve the vacuum condition. The chamber is directly attached to vacuum system for the evacuation process.

### 3.2.2 Vacuum System

The vacuum condition throughout deposition process is crucial for providing a clean environment and minimizing contamination in the sample. In light of this, two types of pumps are used in the vacuum system, which are known as rotary pump and turbo pump. The rotary pump model used is Edwards 28 and turbo pump model used is Pfeiffer Vacuum, which is attached with TD400 turbo drive is directly connected to the bottom plate of CVD reactor. The usage of different types of pumps allow different levels of vacuum based on their pump speed. The system is in low vacuum when the rotary pump with the speed of 16.2 to 19.5 $ft^3min^{-1}$ is used. The ultimate vacuum achieved in the system is approximately ~$1 \times 10^{-3}$ mbar. Meanwhile, the system has high vacuum when the turbo molecular pump in conjunction with backing pump of Jungwoo 20 rotary pump is used, where the ultimate vacuum achieved is around $10^{-6}$ mbar. This turbo pump contains a rotor with high speeds blades, which directs the existing gas molecules in the

University of Malaya

system to be removed through the backing pump. It should be noted that the levels of vacuum are monitored using Oerlikon Leybold Vacuum TTR 91 Pirani gauge for low vacuum, and Oerlikon Leybold Vacuum PTR 225 Penning gauge for high vacuum. The pirani gauge operates at atmospheric to medium vacuum region with the value ranging from $10^{-3}$ to $5\times10^{-4}$ mbar, whereas penning gauge works at high vacuum measurement with the vacuum value ranging from $10^{-3}$ to $10^{-9}$ mbar.

### 3.2.3 Plasma Generator

The reactor gas and electrode are two important elements that required for generating plasma in the reactor chamber. Fundamentally, precursor gas is inserted into the chamber as the reactor gas, through the gas inlet and showerhead. The showerhead is designed with cone-shaped holes for uniform dispersion of precursors. Instead of gas disperser, the stainless-steel showerhead is functioning as an electrode to generate plasma in the system. Further, the electrode is powered through its connection to the RF generator (ENI Model No: ACG-6B) via an impedance matching network for the plasma generation. The impedance matching network is applied to match the impedance of plasma with the impedance of the AC generator. This could minimize the reflected power from the plasma to RF generator. The application of rf to the system configuration leads to the modification of the system into PECVD.

### 3.2.4 Heating Component

A Watlow Fire Rod heater cartridge is utilized for substrate heating, while thermocouple is used to measure the temperature of the heated substrate. The electrical power is supplied by the voltage regulator to the heater cartridge. The heater cartridge with limited temperature of lower than 500 °C is clamped in between the substrate holder to generate a heat transfer from the stainless-steel substrate holder to the substrate. The heater is connected to a voltage regulator model IBC voltage regulator 1 p-1 kVA,

University of Malaya

whereas the thermocouple is connected to the temperature controller (Taishio temperature controller TS-501). The temperature controller functions to set and control the substrate temperature.

The tungsten filament is used to increase the surface deposition temperature of the graphene films at relatively higher temperatures (>500 °C). Hence, the filament is placed on top of the substrate holder, which enables the heat to be radiated from the filament to the substrate. Moreover, the tungsten filament is connected to the IBC voltage regulator with voltage ranging from 0 to 250 V and the maximum current of 60 A. The regulated voltage supply controls the filament temperature. The filament temperature is measured using pyrometer, which is simulated from the incoming infrared energy. Virtually, the addition of filament to the system leads to changes in the system configuration to HF-PECVD.

### 3.2.5 Regulating System

Methane ($CH_4$) and hydrogen ($H_2$) gases are used as the precursor gas for the synthesis of graphene. The $CH_4$ and $H_2$ gases have high purification with the gas purity of 99.995 % and 99.9999 %, respectively. In addition, the $H_2$ gas serves as precursor in $H_2$ plasma treatment and pre-heating of tungsten filament. On the other hand, the purified argon (Ar) gas (99.999 %) is mainly used for sputtering the nickel (Ni) catalyst. The gases are introduced into the system through the gas lines, which are constructed using the stainless steel tubing with diameter of ¼ inch from the gas tanks to the system. The metering valves roughly control the gas flow into the system. Furthermore, the mass flow controller (MFC) is used to control the amount of desired gas with unit reading of standard cubic centimetre per minutes (sccm).

University of Malaya

## 3.3 Substrate Preparation

A silicon dioxide layer on Silicon ($SiO_2$/Si) which is p-type with orientation of (111) is used as a substrate for the graphene growth. The $SiO_2$/Si substrate with the oxide layer on top of the surface is functioning as a diffusion barrier for the transfer-free growth. In this work, $SiO_2$/Si wafer with resistivity and thickness of 0-30 Ohm/cm and 625 ± 25 μm, respectively was purchased from the Polishing Corporation of America manufacturing. The $SiO_2$/Si substrate is cut into the square shape with dimension of 2 cm × 2 cm to obtain large area of sample.

## 3.4 Substrate Cleaning Procedure

The cleaning process of substrate is necessary to eliminate contamination and hydrogen termination on the substrate as well as to increase the adhesion of films on the substrate. Prior to the cleaning process, removal of dust and particles on the $SiO_2$/Si substrate is performed through rinsing the surface of the substrates using the deionized water. The $SiO_2$/Si is then immersed in a diluted hydrochloric acid solution of 37 % HCl, M=36.49 g/mol: 30 % $H_2O_2$, M=34.01 g/mol: deionized water in a ratio of 1:1:6. Subsequently, the $SiO_2$/Si is rinsed with deionized water in ultrasonic bath. The step is repeated using diluted ammonia solution of 25 % $NH_4OH$, M=17.03 g/mol: 30 % $H_2O_2$, M=34.01 g/mol: deionized water in a ratio of 1: 1: 5. The HCl and $NH_4OH$ solution are used to remove residual metal contaminations and organic contaminations, respectively. Subsequently, the $SiO_2$/Si is rinsed in ethyl alcohol followed by acetone to prevent water marks. Finally, the substrate is dried under nitrogen ($N_2$) purging.

## 3.5 Deposition Procedure

In general, the deposition process of graphene using home-built PECVD system involves three steps including deposition of metal catalyst, graphene deposition, and

University of Malaya

catalyst etching process. Figure 3.3 demonstrates the schematic of the deposition steps of transfer-free graphene growth. Prior to the deposition of graphene, pre-deposition is performed for ensuring cleanliness of the substrates and system before deposition. After the deposition is completed, post-deposition step is required for removing the samples out from the chamber.

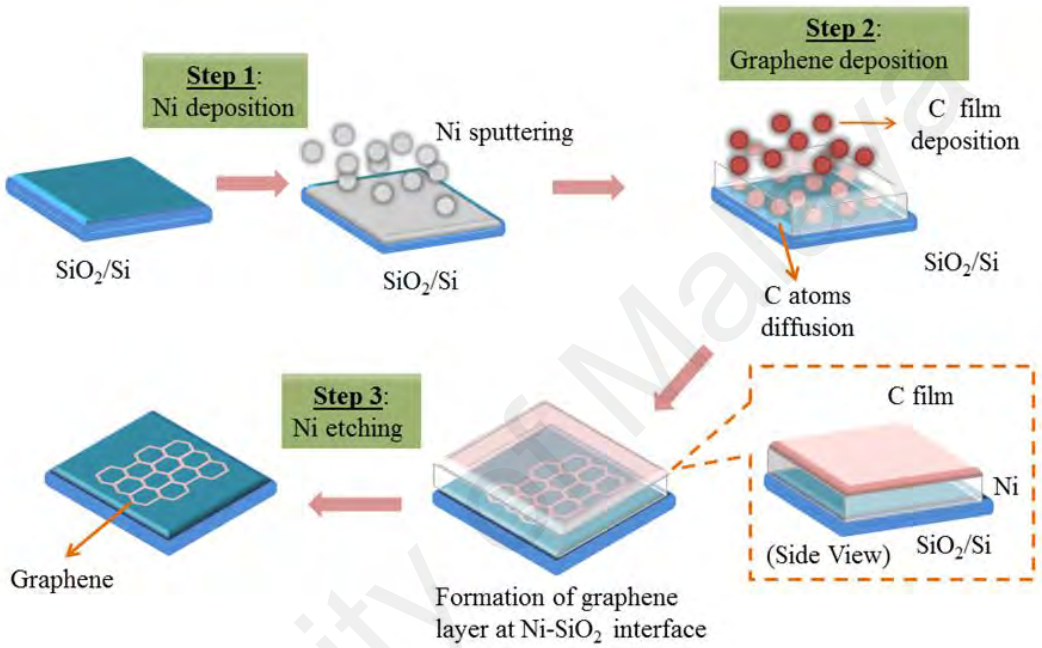


**Figure 3.3: Schematic of deposition process of transfer-free graphene.**

### 3.5.1 Pre-deposition

The cleanliness is crucial for producing good samples, where it is aimed to avoid any problem arise due to the contamination. First of all, the CVD chamber is thoroughly cleaned using acetone as a degreasing agent to eliminate dirt and contamination. Next, the cleaned substrates are placed onto the substrate holder into the CVD reactor. Prior to the evacuation process, all the evacuation valves are closed and the CVD reactor is screwed tightly. The reactor is then pumped down to low vacuum at pressure below $10^{-3}$ mbar. The residual gases contained inside the gas lines are emptied by opening the gas

University of Malaya

valves. Consequently, the residual gas is drained out through the chamber. Moreover, it is important to empty the line gases to avoid contamination by any other gas before introducing the gas source into the reactor for deposition. The CVD reactor is then pumped down using turbo molecular pump to high vacuum at pressure of ~$2\times10^{-5}$ mbar. Once a stable pressure is reached, the reactor pressure is kept at ~$3\times10^{-3}$ mbar, where the system is ready for the deposition process.

### 3.5.2 Deposition of Catalyst

Prior to graphene growth, nickel films are sputtered onto $SiO_2$/Si and quartz substrates using plasma-assisted CVD. Figure 3.4 illustrates the schematic diagram of the sputtering process. The sputtered Ni is functioned as a catalyst or buffer layer for the graphene growth. Nickel foil with diameter of 10 cm is used as a replacement to showerhead, where it simultaneously acts as a Ni target and electrode for plasma generation. Ar gas is dispersed in between the Ni target and substrate by inserting the Ar gas through the gas inlet that is located at the side of the CVD chamber. Both plasma and Ar gas are used as a reactor agent for the sputtering process. Furthermore, the substrates are heated at 150 °C for better adhesion of the Ni on the substrate. Generally, the Ni thickness is varied by adjusting the distance between the target and substrate.

University of Malaya

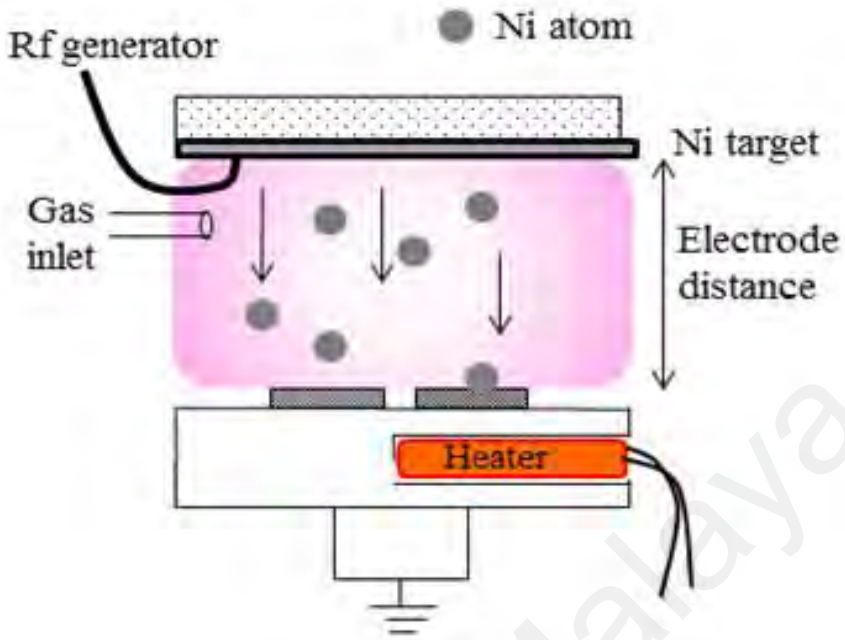


**Figure 3.4: Schematic diagram of Ni sputtering process.**

### 3.5.3 Deposition of Graphene

In general, the deposition involves both catalyst formation and graphene fabrication process. The deposition of both catalyst and graphene are performed using PECVD technique. The current study investigates four sets of samples, where the deposition parameters and the technique were altered for each set of deposition. The PECVD technique was mainly used for sets 1 and 2, while hot-filament was utilized for sets 3 and 4 to increase the growth temperature. The details of each deposition parameter and procedures are summarized in Table 3.1.

### 3.5.4 Post Deposition

After the deposition process is completed, all the excess gases are pumped out by evacuating the reactor chamber and the gas line. At the same time, the system is cooled down until the temperature reached below 80 °C. Once the system has reached the desired temperature, the rotary pump is switched off. The chamber is opened after allowing air to

University of Malaya

enter the chamber via admittance valve and reached atmospheric pressure. Finally, the samples are taken out from the chamber and stored for characterization.

**Table 3.1: Summary of deposition parameter and procedure.**

| No. of set | Technique | Study parameter | $H_2$ plasma treatment | Deposition parameter |
|---|---|---|---|---|
| 1 | Ni sputtering using PECVD | Electrode distance ($E_d$) | Rf power = 50 W<br>$H_2$ flow rate = 50 sccm<br>Duration time = 10 min | P = $6.0 \times 10^{-2}$ mbar<br>$T_s$= 150 °C<br>Rf power = 60 W<br>Ar = 2 sccm<br>$t_d$ = 15 minutes |
| 2 | PECVD transfer-free graphene | Ni thickness ($d_{Ni}$) | Rf power = 50 W<br>$H_2$ flow rate = 50 sccm<br>Duration time = 10 min | P = 1.8 mbar<br>$T_s$= 400 °C<br>Rf power = 80 W<br>$CH_4$ flow rate = 10 sccm<br>$H_2$ flow rate = 100 sccm<br>$T_d$ = 5 minutes |
| 3 | HF-PECVD transfer-free graphene | Deposition time ($t_d$) | Rf power = 50 W<br>$H_2$ flow rate = 50 sccm<br>Duration time = 60 sec | P = 1.8 mbar<br>$T_s$= 400 °C<br>Rf power = 80 W<br>$CH_4$ flow rate = 10 sccm<br>$H_2$ flow rate = 100 sccm |
| 4 | HF-PECVD transfer-free graphene | Substrate temperature ($T_S$) | Rf power = 50 W<br>$H_2$ flow rate = 50 sccm<br>Duration time = 60 sec | P = 1.8 mbar<br>Duration time = 60 sec<br>Rf power = 80 W<br>$CH_4$ flow rate = 10 sccm<br>$H_2$ flow rate = 100 sccm |

### 3.5.5 Etching Process of Ni

For the etching process of the Ni layer, the sample is immersed in a diluted hydrochloric acid solution of 37 % HCl, M=36.49 g/mol: 30 % $H_2O_2$, M=34.01 g/mol: deionized water in a ratio of 1:1:8. The sample is then rinsed with the deionized water and dried in the oven for a few minutes. The schematic diagram of the process is illustrated in Figure 3.5.

University of Malaya

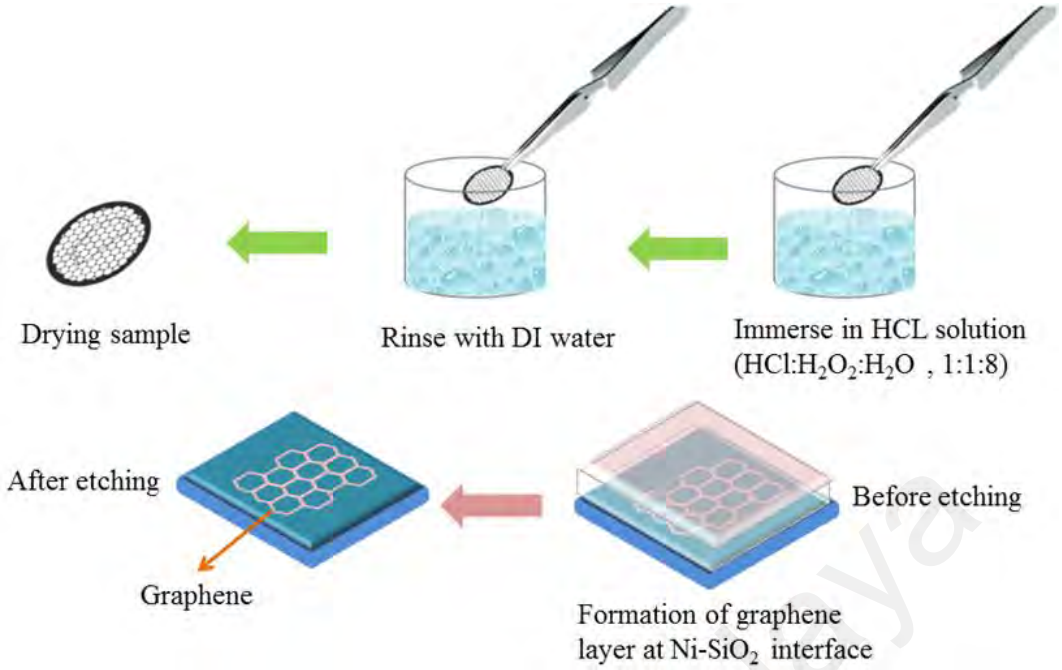


**Figure 3.5: Schematic of the Ni etching process.**

## 3.6 Characterization Technique

The characterization techniques are appropriate to study the physical behaviors of Ni catalyst and graphene films. The characterization techniques are classified into five categories, which consisted of films thickness, morphological study, elemental composition analysis, structural properties and chemical bonding analysis. The film thickness of the samples is measured using profilometer. In addition, the morphological study of the samples is performed via field emission scanning electron microscopy and atomic force microscopy. The structural properties of samples are investigated using X-ray diffraction, micro-Raman spectroscopy, and high-resolution transmission electron microscopy. The elemental composition and chemical bonding of the samples are examined using energy dispersion X-ray and X-ray photoelectron spectroscopy, respectively.

University of Malaya

### 3.6.1 Film Thickness

**a) Surface Profile**

The thickness of the nickel (Ni) film is measured using KLA-Tencor P-6 surface profiler system. This profiler unit is a contact mode, where the stylus touches the film's surface throughout the measurement. The height position of the stylus generates analog signal. The stylus measures the thickness of the film as it moves along the surface by converting the analog signal into a digital signal that is stored, analyzed and displayed by the profilometer. The thickness of the films was measured along the film starting from the substrate to the center of the film by passing through the films edge. The average thickness values of the samples were obtained by scanning the sample thickness at few different spots. Figure 3.6(a) and (b) depict the KLA-Tencor P-6 profilometer and example of the cross section profile, respectively. Table 3.2 demonstrates the parameter used for the surface profiler measurement.

**Table 3.2: List of parameters used for measurement of the Ni film thickness.**

| Parameter | Units |
|---|---|
| Speed of scan | 200 μm/s |
| Applied force | 1 mg |
| Scan rate | 50 Hz |

University of Malaya

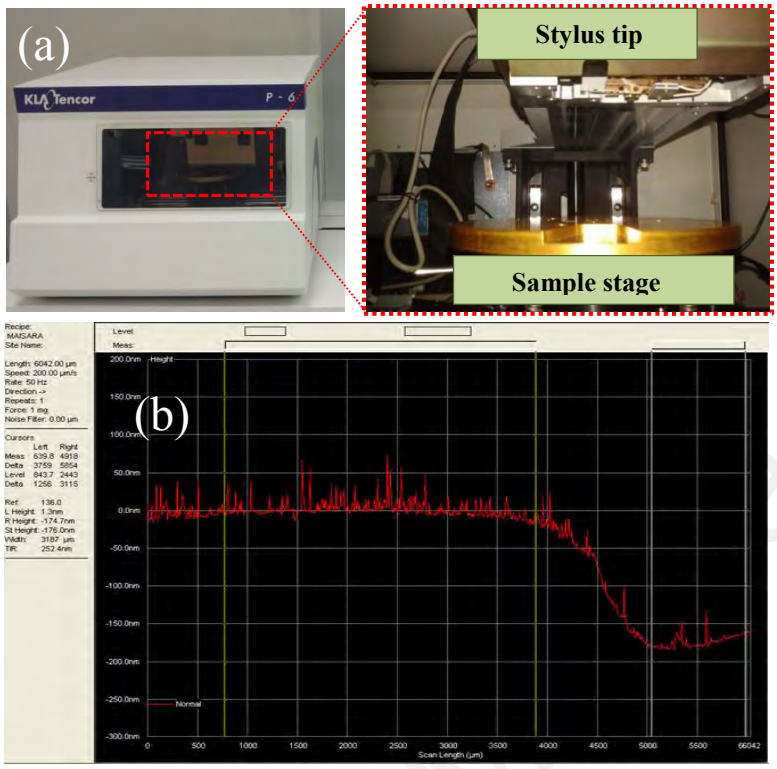


**Figure 3.6: The image of KLA-Tencor P-6 profilometer and example of the cross-section profile.**

### 3.6.2 Morphological Study

**a) Field Emission Scanning Electron Microscopy**

The characterization on surface morphology of micro or nanosize structures is commonly investigated using field emission scanning electron microscope (FESEM). The electron microscope is used as it provides better resolution and depth of focus images compared to optical microscope. The use of field emission gun in FESEM enables up to three orders of magnitude greater electron density. Thereupon, it provides higher brightness compared to the thermionic electron in SEM. The sample is scanned by a focus beam of electrons and the image is reconstructed using the signals and magnified on the screen. Figure 3.7 illustrates the scanning of the sample and image. The magnification of the SEM image is altered by adjusting the length of scan on the specimen (L Spec)

University of M

corresponding to a constant length of scan on the Cathode Ray Tube (CRT). The magnification size, M is expressed as follows:

$$M = {}^{L_{CRT}}\Big/_{L_{Spec}} \tag{3.1}$$

where, LCRT is the length of scan on the Cathode Ray Tube and LSpec is the length of scan on the specimen. Table 3.3 demonstrates the area of sample as a function of magnification. Figure 3.8 illustrates the typical FESEM images of Ni island that were captured using JEOL JSM 760C FESEM microscope at different magnifications.

**Table 3.3: The area of sample as a function of magnification.**

| Magnification | Area on sample |
|---|---|
| 10 X | $(1\ cm)^2$ |
| 100 X | $(1\ mm)^2$ |
| 1000 X | $(10\ \mu m)^2$ |
| 10000 X | $(1\ \mu m)^2$ |
| 50000 X | $(0.5\ \mu m)^2$ |

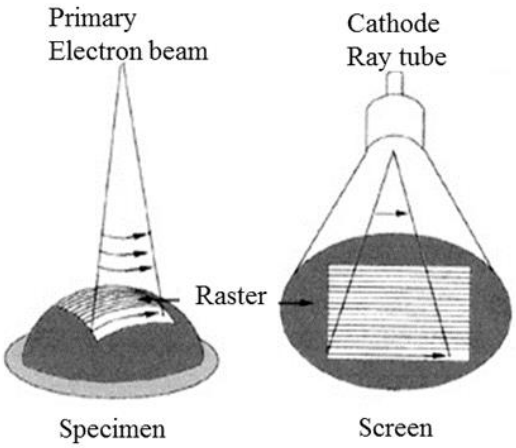


**Figure 3.7: Sample scanning and scanning image on screen.**

University of Malaya

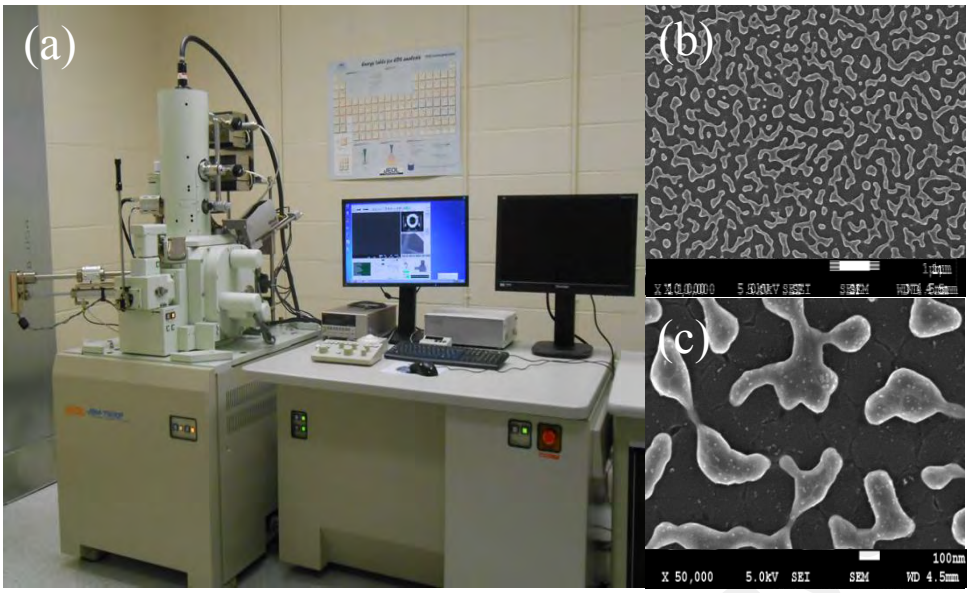


**Figure 3.8: Typical FESEM images of Ni island captured at different magnifications.**

**b) Atomic Force Microscopy**

The atomic force microscope (AFM) is a type of contact scanning probe that is functioned by measuring the sample's surface using a mechanical probe. This AFM method can be used to see a surface in full down to nanometer scale. It can be applied to soft and hard synthetic materials, irrespective of opaqueness or conductivity. In this work, the AFM is used for the imaging of the samples. Figure 3.9 illustrates the Agilent atomic force microscopy (AFM) 5500, two-dimensional and three-dimensional topography images of Ni films. The three-dimensional shape or topography of the sample is determined by measuring the reaction of the probe when force is applied towards the sample. This is obtained by scanning the sample with respect to the tip and recording the height of the probe that corresponds to a constant probe-sample interaction. The obtained AFM image is a simulated image based on height of each scanning point of the surface, where each point of the surface has a height.

University of Malaya

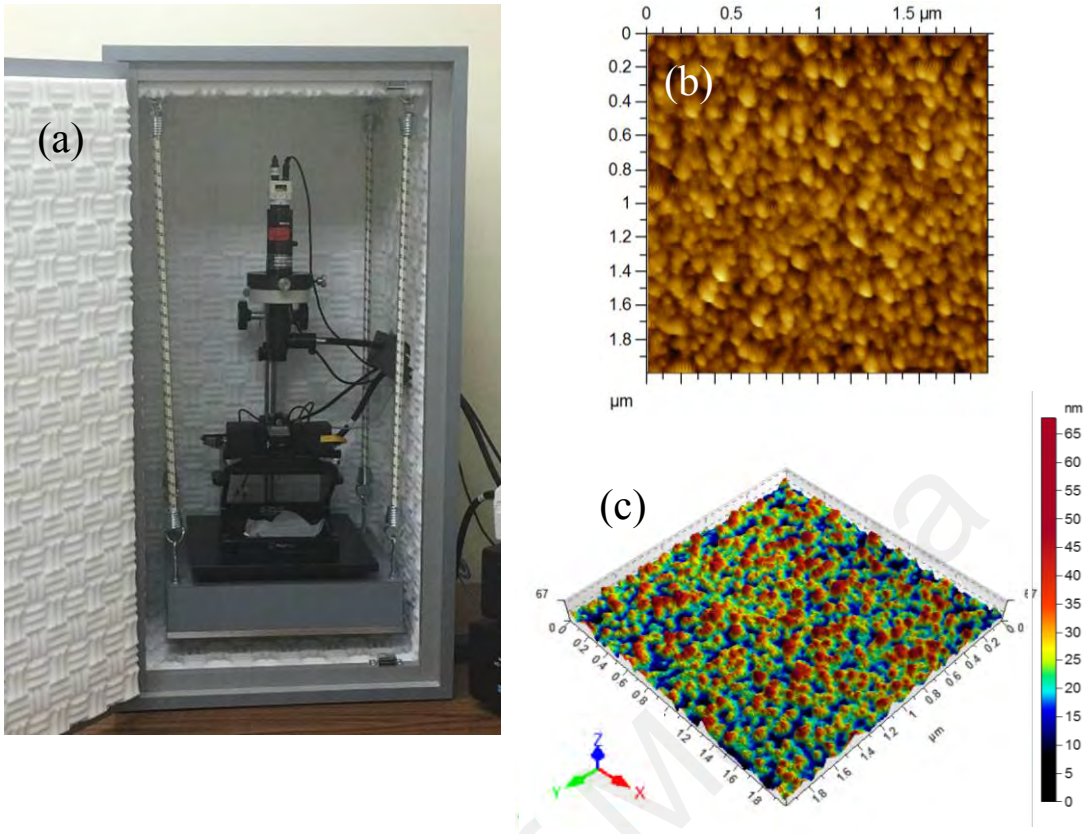


**Figure 3.9: (a) Photograph of Agilent atomic force microscope, (b) two-dimensional and (c) three-dimensional topography images of Ni films.**

### 3.6.3 Structural Properties

**a) X-ray Diffraction**

The X-ray diffraction (XRD) is commonly used for characterizing the crystal structure of the samples. The crystallinity of an element can be identified by determining the peak position in XRD pattern, while the orientation plane corresponding to the peak can be assigned. The qualitative determination of the crystallinity of the samples could be analyzed through the intensity of the diffraction peak. Figure 3.10 illustrates a typical XRD pattern of a crystalline Ni measured by SIEMENS D5000 X-ray diffractometer in a $2\theta$ range from 10° to 80°. It should be noted that the Si peak is detected from the Si substrate. The crystalline plane corresponding to the diffraction peaks of Ni are shown in the figure. Generally, the dominant diffraction peak is used for further structural analysis

University of Malaya

by deconvoluting it using Gaussion or Lorentzian function as shown in Figure 3.11. The crystallite size, $D_x$ of the Ni can be quantitatively calculated from the width of the diffraction peak, which is correlated to the intensity using Debye-Scherrer's equation (Cullity & Weymouth, 1957) as expressed below:

$$D_X = \frac{C\lambda}{\phi \cos\theta} \tag{3.2}$$

where, $C$ is the Scherrer's constant with value of 0.89, $\lambda$ is the wavelength of CuKα (1.5418 Å), $\phi$ is the FWHM of the diffraction peak and $\theta$ is the angle of the diffraction peak.

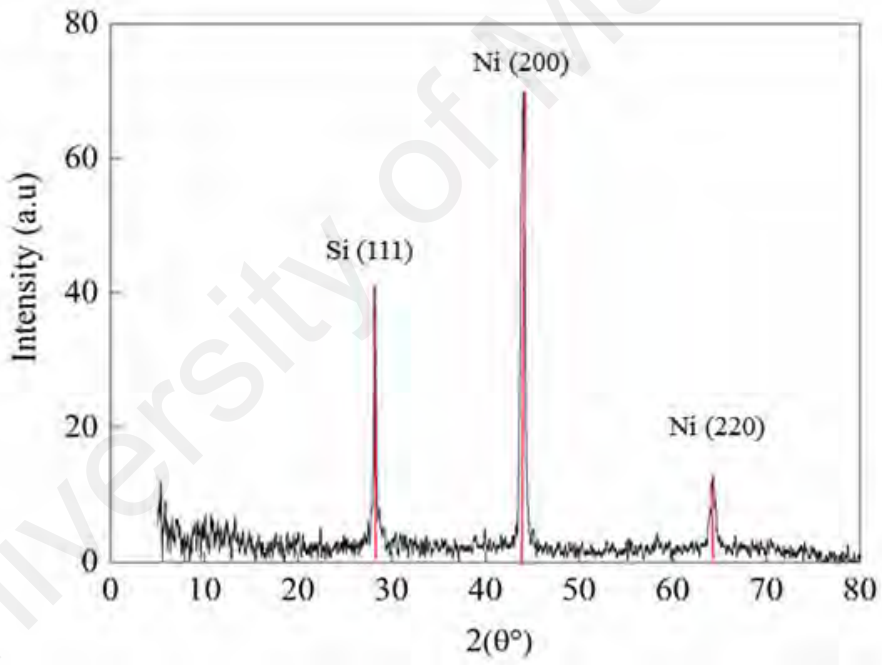


**Figure 3.10: Typical XRD pattern of a polycrystalline Ni sample deposited on $SiO_2$ substrate.**

University of Malaya

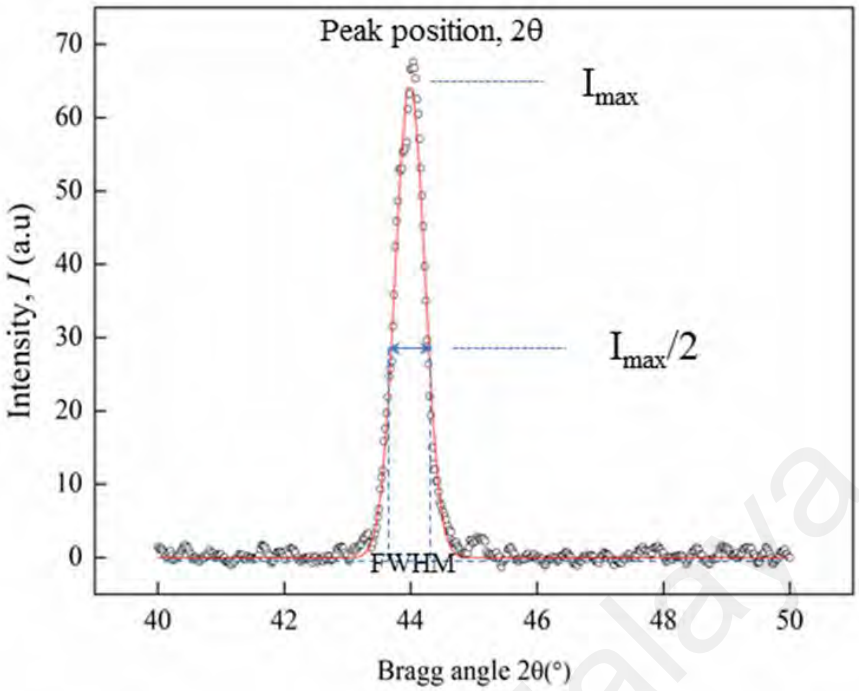


**Figure 3.11: Deconvolution of Ni (200) diffraction peak using Gaussian function.**

**b) Micro-Raman Spectroscopy**

The Raman spectroscopy is a vibrational technique that is widely used for investigating the structural properties of carbon material, including graphene films. The Raman spectroscopy has higher sensitivity, in which it is able to detect even the smallest difference in geometric structure and bonding within a molecule. The sensitivity of the Raman spectroscopy is appropriate to study the different forms of allotrope of carbon. This is because the various forms of allotrope of carbon differ only in the relative position of their carbon and their bonding to one another. Figure 3.12 illustrates the Renishaw's inVia Raman microscope. The sample is measured under ambient condition without the need for sample preparation procedure, where the Raman spectra can be obtained rapidly (within few seconds). Table 3.4 displays the list of parameters that are suitable for measuring Raman spectra of graphene film. In this work, 514 nm visible laser is used. The laser power (in percentage) and exposure time of the laser to the sample could be adjusted to prevent the sample heating or damage. Figure 3.13 illustrates the deconvoluted

University of Malaya

Raman spectrum of the graphene. Three main vibrational bands that present in the spectrum contain vital information about graphene. Moreover, the layer thickness is obtained by analyzing the band's peak position, band shape, and intensity.


**Figure 3.12: Photograph of Renishaw's inVia Raman microscope.**

**Table 3.4: List of parameters used for measuring Raman spectra of graphene film.**

| **Parameter** | **Units** |
|---|---|
| Laser wavelength (nm) | 514 |
| Grating (l/mm) | 2400 |
| Laser power (%) | 100 |
| Exposure time (s) | 10 |
| Objective lens | 50 X |

University of Malaya

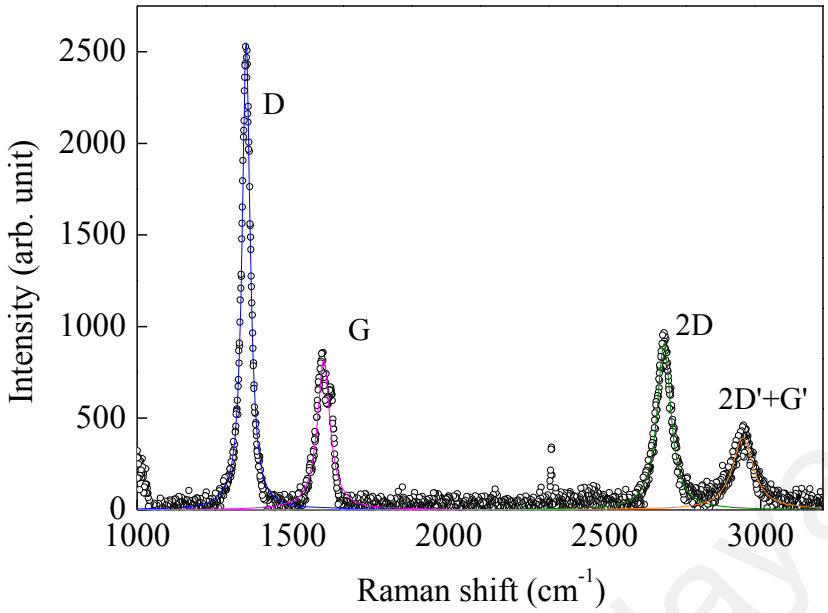


**Figure 3.13: Deconvolution of graphene Raman peaks using Lorentzian function.**

The Raman mapping is one of the powerful tools used to assess a sample's layer thickness uniformity, especially graphene. In addition, the Raman microscope features an automated stage and associated software to generate detailed point map. The Raman mapping involves the coordinated measurement of Raman spectra with successive movements of the sample by a specified distance. Figure 3.14 illustrates the image of graphene sample and the results of Raman mapping measurement. The Raman map of the sample is formed by obtaining a series of Raman point measurements in the area depicted in the image. The different colour areas indicate regions that different in layer thickness by measuring the ratio intensity of 2D and G peak.

University of Malaya

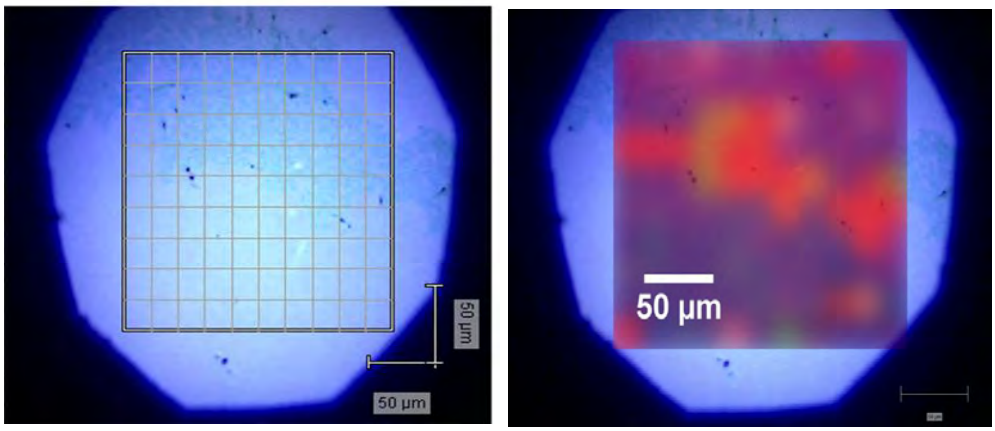


**Figure 3.14: Optical image and Raman mapping image of multilayer graphene.**

**c) High-resolution Transmission Electron Microscopy**

The high-resolution transmission electron microscopy (HRTEM) is the most effective method for investigating the number of graphene layers. The HRTEM requires the thin samples (<100 nm) in order to obtain higher resolution image. Furthermore, the copper grid with carbon supporting film is used to hold the sample. It should be noted that Lacey film 400 mesh copper grid was used in this work. Furthermore, the samples on the substrate were scratched out and immersed in an ethanol solution for sonication about 10 minutes. Subsequently, the graphene diluted ethanol solution was transferred onto the copper grid and dried for few days prior to the TEM measurement.

The HRTEM enables free-standing layers of graphene on a copper grid, which is easily observed in an optical microscope. The free-standing image is identified from the folding at the edges or within the free-hanging of graphene sheet when the sheet is locally parallel to the beam. The edges and folding could be identified by the direct visualization of the diffraction analysis of the freely suspended sheets. The dark lines represent the total number of graphene layer. Figure 3.15 illustrates the typical HRTEM micrographs of graphene and JEOL-JEM 2100-F of HRTEM.

University of Malaya

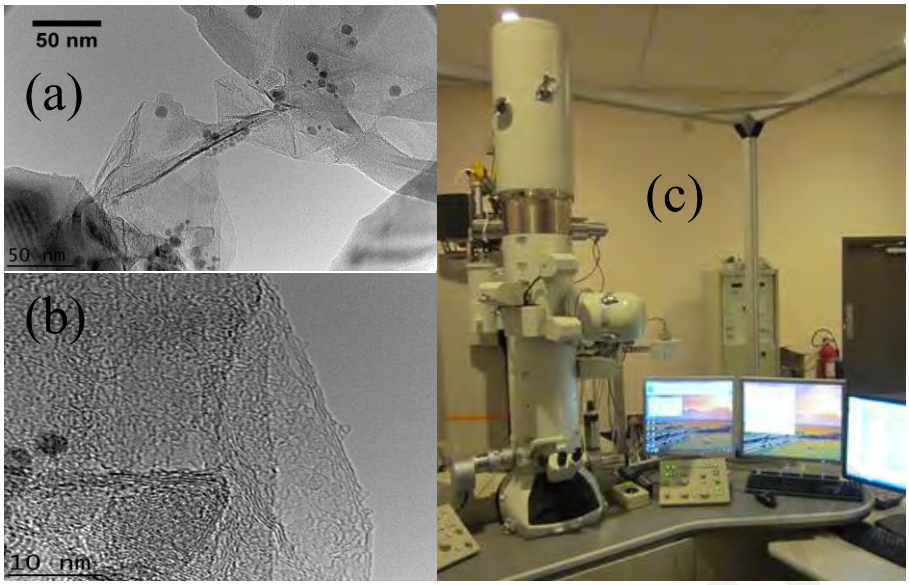


**Figure 3.15: (a) Low magnification, (b) high magnification of typical HRTEM micrographs of graphene and (c) JEOL-JEM 2100-F HRTEM.**

### 3.6.4 Element Composition

**a) X-ray Photoelectron Spectroscopy**

The X-ray photoelectron spectroscopy (XPS) is a quantitative spectroscopic technique that measures the elemental composition and chemical state of the graphene sample. In XPS, electrons that are emitted after the interaction of primary X-ray and the sample, are then liberated from the surface as a result of the photoemission process (XPS). Figure 3.16 demonstrates the photograph of Quanta PHI II used for characterizing the chemical bonding and element composition of the graphene sample. The XPS spectrum was obtained by exposing the sample to the X-ray beam, while simultaneously measure the kinetic energy and number of electron that escape from few nanometers (0 to 10 nm) of the sample. Figure 3.17 displays wide scan of graphene grown on $SiO_2$ substrate. A survey spectrum or wide scan demonstrates all elements present on the sample surface. Due to low thickness of graphene film, the X-ray beam penetrates the substrate and measures the elements in the substrate. Figure 3.18 demonstrates the high-resolution spectrum of

University of Malaya

graphene in the energy range of the C1s. The raw data spectrum (black) is fitted with five components or chemical states.


**Figure 3.16: Photograph of X-ray photoelectron microscope.**

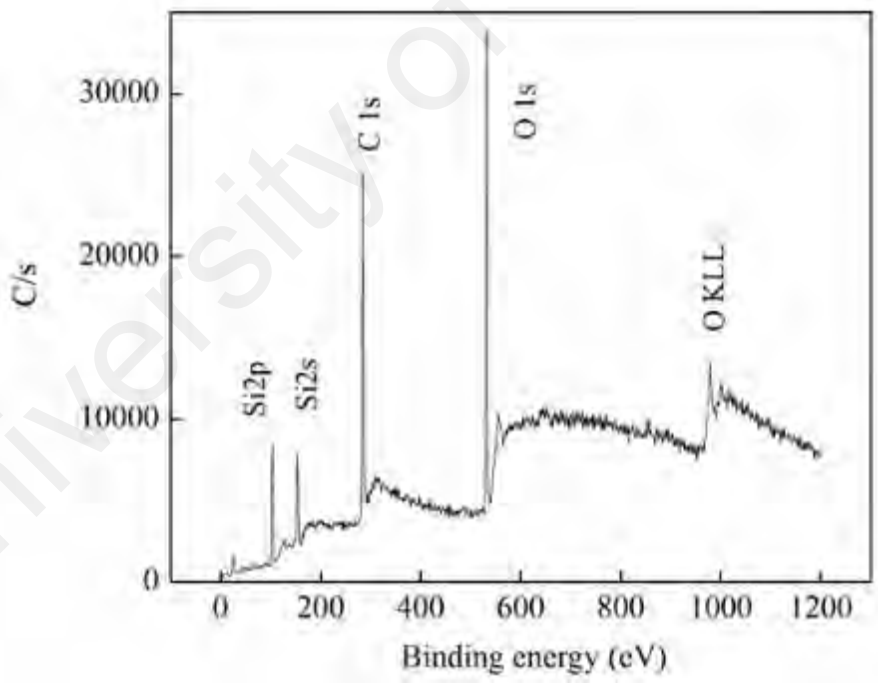


**Figure 3.17: Wide scan XPS spectrum of graphene film on $SiO_2$/Si substrate.**

University of Malaya

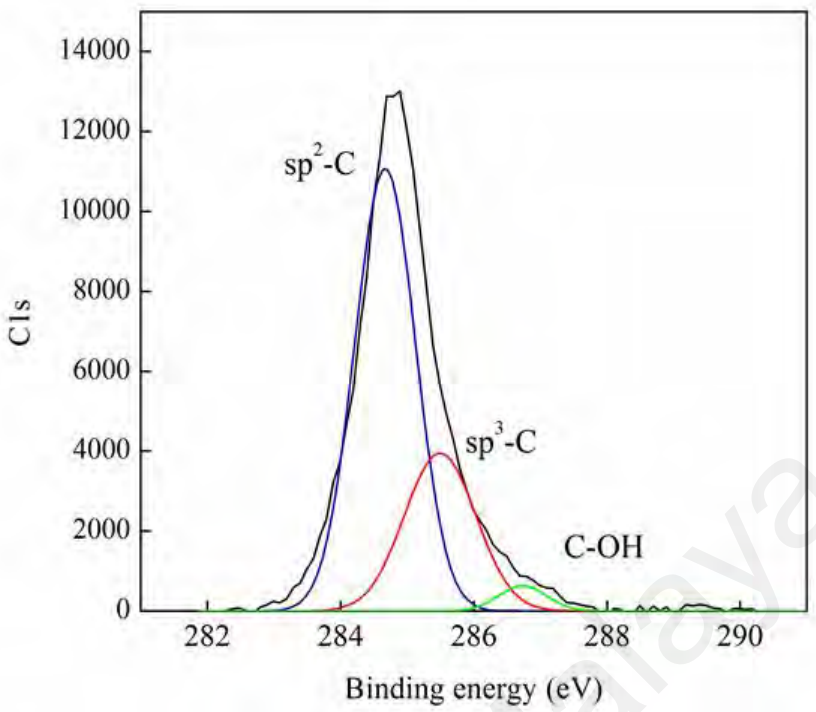


**Figure 3.18: High-resolution XPS spectrum of C1s.**

**b) Depth Profile X-ray Photoelectron Spectroscopy**

The depth profile XPS is a very useful technique for obtaining information of several nm or even less than one nm depth of catalytically active layers. The depth profile of sample can be obtained by combining a sequence of ion gun etch cycles interleaved with XPS measurements from the current surface. Moreover, an ion gun is used to etch the material for a period of time and exposes a new surface for each ion gun etching cycle. The XPS spectra are acquired while etching, and the spectra provide the means of analyzing the composition of the materials surfaces. The actual depth for each XPS analysis is dependent on the etching rate of the ion-gun, which in turn depends on the material being etched at any given depth. Figure 3.19 illustrates the XPS depth profile of Ni/graphene/Si substrate.

University of Malaya

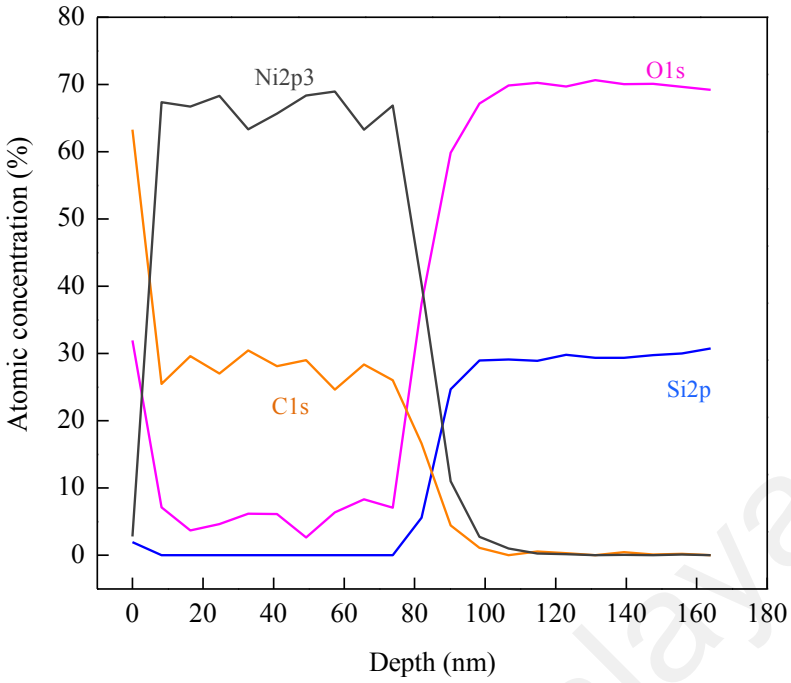


**Figure 3.19 : XPS depth profile of Ni/graphene/$SiO_2$ substrate.**

### 3.6.5 Wettability Properties

**a) Sessile Drop Method**

Generally, the wettability studies involve the measurement of water contact angle as the primary data. In this work, Theta Lite Optical Tensiometer was used to measure the contact angle, which indicates the degree of wetting when the water droplet interacts with the sample. The value of the contact angle is directly measured from the tangent angle of the contact point along the liquid-vapour interface in the droplet profile, as shown in Figure 3.20. The diagram of the measurement set-up is illustrated in Figure 3.21. The equipment consists of a horizontal stage to locate the sample, a micrometer syringe to form a water drop, an illumination source, and a camera. The camera is integrated to capture the photographs of the drop profile, in which the contact angle at leisure is measured. This direct optical method is advantageous because of its simplicity and the need for only small amount of liquid and surface area.

University of Malaya

The water contact angle measurement were carried out at room temperature of 25 ± 0.5 °C. A drop of distilled water is used in this measurement. The microliter syringe of 100µL is connected to the micromanipulator to adjust the position of the needle tip of the syringe. The tip is positioned at the center of the sample, which is a few micrometers above the films surface. This is done to reduce the gravitational effects when the water droplet is released. The droplet was selected to be 2 µL. The image of the water droplet is captured using CCD camera, which is connected to a computer. The images of the spreading water droplet and the contact angle are measured using the *OneAttension* software.

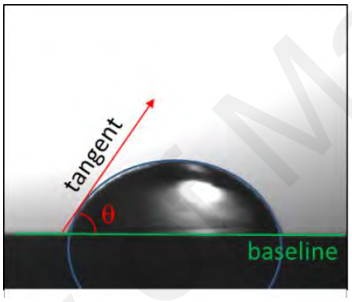


**Figure 3.20: The angle between the tangent line at the contact point and the horizontal line of the solid surface.**

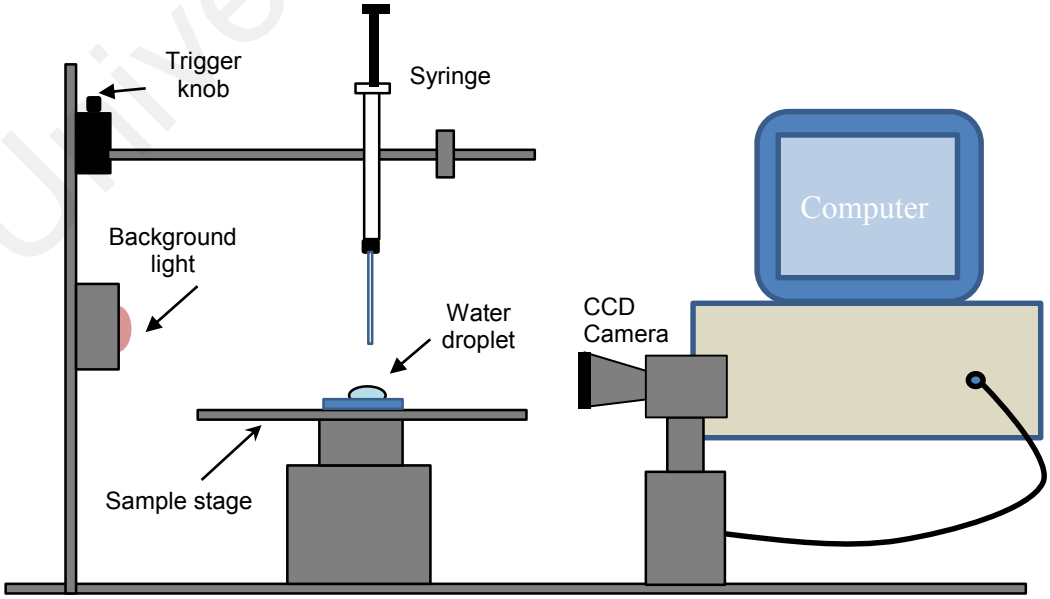


**Figure 3.21: Contact angle measurement set-up.**

University of Malaya

### 3.6.6 Magnetic Properties

**a) Vibrating Sample Magnetometer**

The vibrating sample magnetometer (VSM) is a measurement technique that allows the determination of magnetic moment of the sample. In this study, Lake Shore Magnetometer is used for performing VSM measurement as shown in Figure 3.22(a). Based on Faraday's law, an electromagnetic force is generated in a coil when there is a change in flux through the coil. The sample is moved in the proximity of two pickup coil and undergoes sinusoidal motion, i.e., mechanical vibrated as indicated in Figure 3.22(b). The resulting magnetic flux changes induce a voltage in the sensing coils that is proportional to the magnetic moment of the sample. Consequently, the electromagnetic or a superconducting magnet will generate the magnetic field. As the magnetic media is characterized at ambient temperature and moderate level of field strengths, the electromagnet based system is considered for the current context.

The typical hysteresis loop enables the link between the magnetization, M and the applied field, H. The hysteresis loop of graphene film is illustrated in Figure 3.23. Thereupon, the saturation magnetization, $M_s$ is the parameter extracted from the hysteresis loop that is used to characterize the magnetic properties of the sample. The intrinsic saturation is attain at maximum H; and at zero-field, the remanence is reached. The increase and decrease in the external field from positive saturation to negative saturation and back indicates a ferromagnetic hysteresis loop (Figure 3.23*)*.

University of Malaya

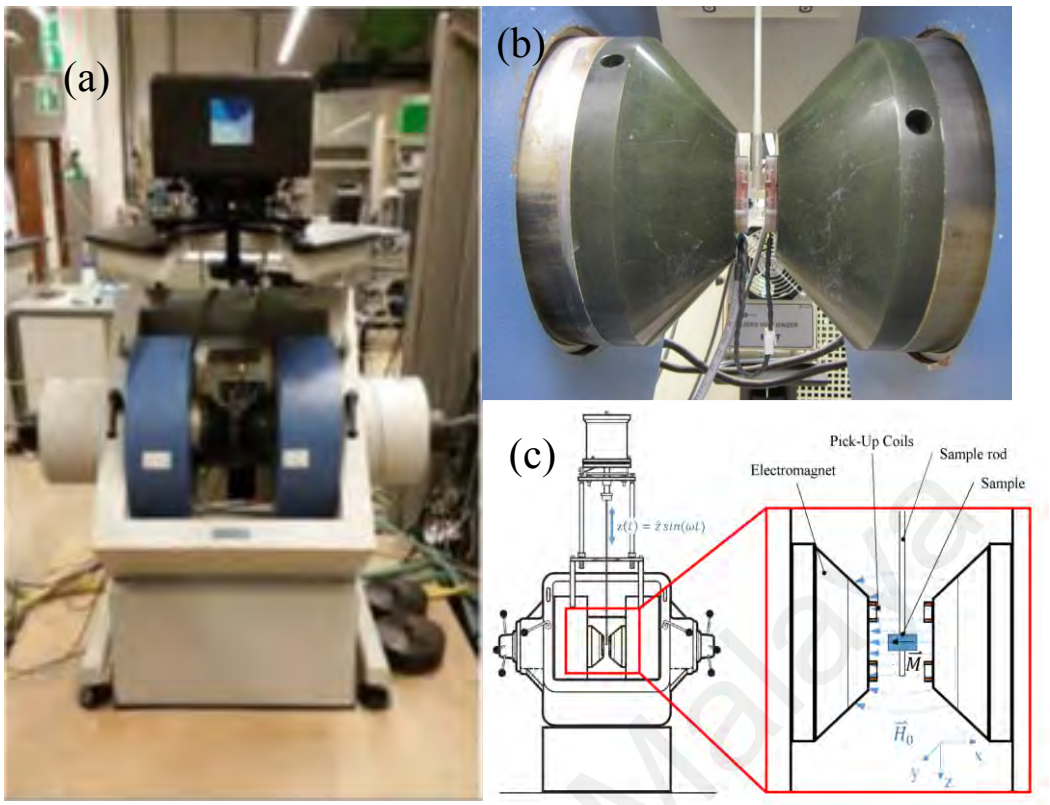


**Figure 3.22: Lakeshore VSM 7400 system. (a) Overview of the setup, (b) Sample holder and pick up coil in between pole pieces and (c) schematic diagram of VSM measurement.**

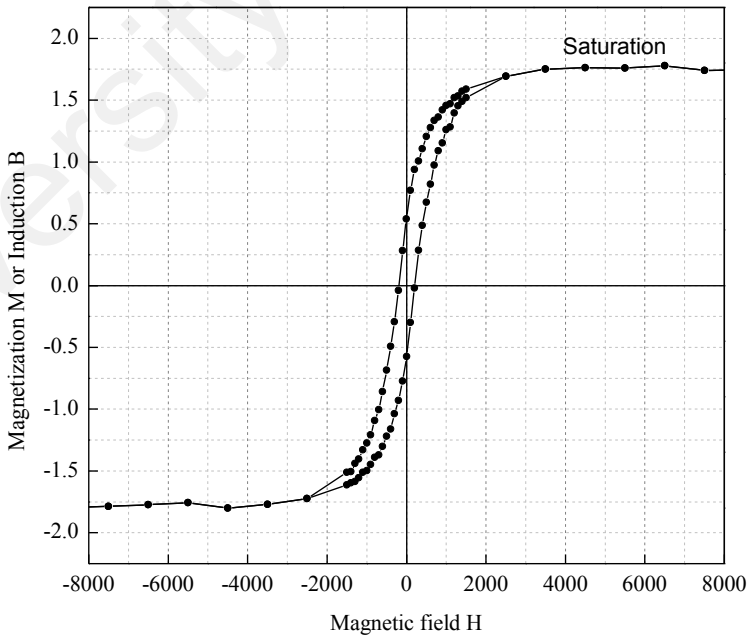


**Figure 3.23: Hysteresis loop of graphene film.**

University of Malaya

# CHAPTER 4: SYNTHESIS OF TRANSFER-FREE GRAPHENE USING NICKEL CATALYST BY PLASMA ENHANCED CHEMICAL VAPOUR DEPOSITION TECHNIQUE

## 4.1 Introduction

This chapter describes the feasibility of using PECVD to obtain transfer-free graphene by applying certain modification of Ni film that is used as a buffer layer. The attributes of Ni film such as low temperature and large area deposition favor its usage in this regard. The modification of the Ni layers is caused by variations in their films thickness and grain size. This first part of this section is further divided into two parts; Firstly, it focuses on the synthesis of Ni films on the $SiO_2$ (111) substrates at different Ni target-to-substrate distances to obtain various Ni film thicknesses. The properties of the Ni films are discussed as a function of the gap distance, where the thickness, grains size, morphological and structural properties of the Ni films are determined from profilometer, FESEM, and XRD analysis, respectively. Secondly, it describes the effects of these Ni thicknesses on the properties of the subsequent transfer-free graphene growth. The structural, morphological and elemental properties of the graphene are determined using Raman spectroscopy, FESEM and HRTEM, and XPS, respectively. The objectives of this work are to synthesize a large-area of transfer-free graphene at low temperature and to investigate the optimized Ni film thickness of growing these graphene films. Moreover, the influence of Ni thickness and grain size on the transfer-free graphene growth is discussed in this chapter.

## 4.2 Effects of Ni Target to Substrate Distance on the Growth of Ni Catalyst

### 4.2.1 Thickness of Ni Films

The variation of Ni thickness sputtered onto $SiO_2$ substrate as a function of Ni target-to-substrate distances ($d_{Ni}$) is shown in Figure 4.1(a). It should be noted that the Ni target



University of Malaya

was placed on the RF powered electrode of the sputtering system. The thicknesses of the films was determined by measuring the average thickness of the Ni films at different spots. The thickness of the films decreased linearly with the increase in $d_{Ni}$. It is evident that the distance between the target and the substrate greatly influence the growth of these Ni films. Since the deposition time is fixed for all depositions, the decrease in the thickness at higher gap distance is mainly due to the decrease in exposure area of the substrate to the increased path outspread of the Ni sputtering beam. Evidence has shown that the $d_{Ni}$ influences the pathway of Ar gas and Ni atoms as the sputtering rate is changed when the value of $d_{Ni}$ is varied (Yasuda, 2004).

The thickness measurement from the profilometer readings were cross-checked against the cross-sectional image from FESEM as shown in Figure 4.1(b). The thickness of the cross-sectional image was determined using the Image J software with the FESEM measurement scale as a reference.

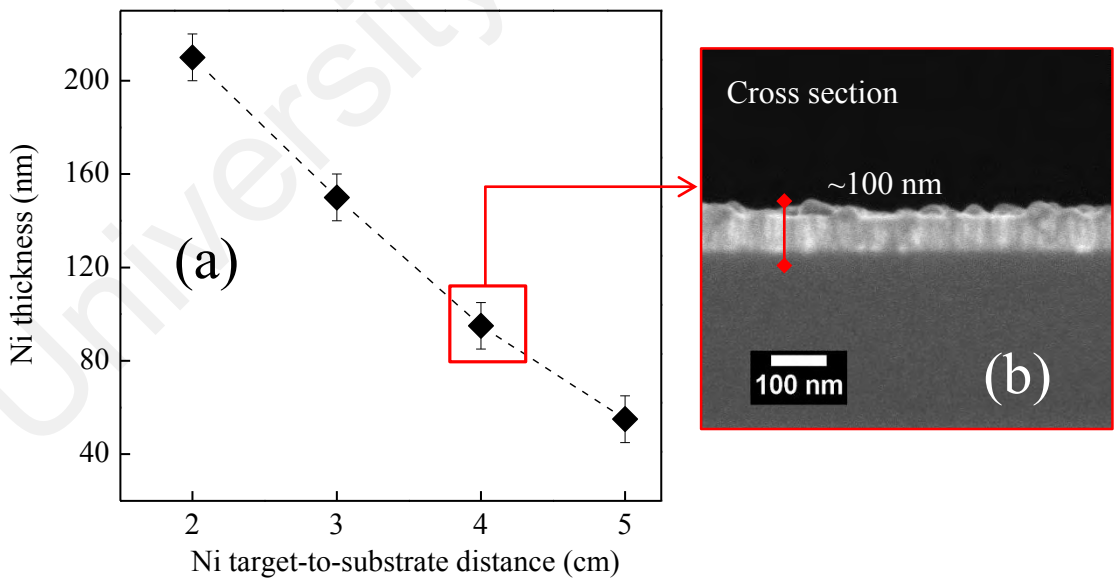


**Figure 4.1: (a) Variation in Ni thickness as a function of electrode distance and (b) cross section of FESEM image of Ni thickness at electrode distance of 4 cm.**

University of Malaya

### 4.2.2 Morphology of the Ni Catalyst Growth

Figure 4.2 demonstrates the FESEM images of Ni films prepared on $SiO_2$ substrate at different Ni target-to-substrate distances. The image indicates that the morphologies of the sputtered Ni were found to be significantly influenced by the $d_{Ni}$. Furthermore, the morphology of all films exhibited nanosize grains. The FESEM image of the Ni film sputtered at $d_{Ni}$ of 5 cm indicates the formation of non-uniform film with the presence of void on the $SiO_2$ substrate. The grains were smaller and unevenly distributed onto the $SiO_2$ substrate, which created a loosely packed film. These Ni grains formed as isolated clusters, which exposed the substrate beneath. The Ni films become denser and compact for the films sputtered at lower $d_{Ni}$ value for the FESEM. The voids disappeared at $d_{Ni}$ of 4, 3, and 2 cm due to large area coverage of Ni sputtered onto the $SiO_2$ substrates at lower gap between the Ni target and the substrates. The denser clusters distribution with larger grains size was formed at $d_{Ni}$ value of 4 cm. Moreover, further decrease in $d_{Ni}$ up to 3 cm resulted in the increase in the cluster size, where it became more compact and well-ordered. Nevertheless, the size distribution of the cluster became uneven with further decrease in the value of $d_{Ni}$ at 2 cm. The results indicate that the formations of sputtered Ni were influenced by the difference in $d_{Ni}$. Importantly, the kinetics of sputtered species arriving at the substrate could be controlled by these $d_{Ni}$, which in turn governs the atom mobility and atomic rearrangement of the Ni (Kar et al., 2008).

University of Malaya

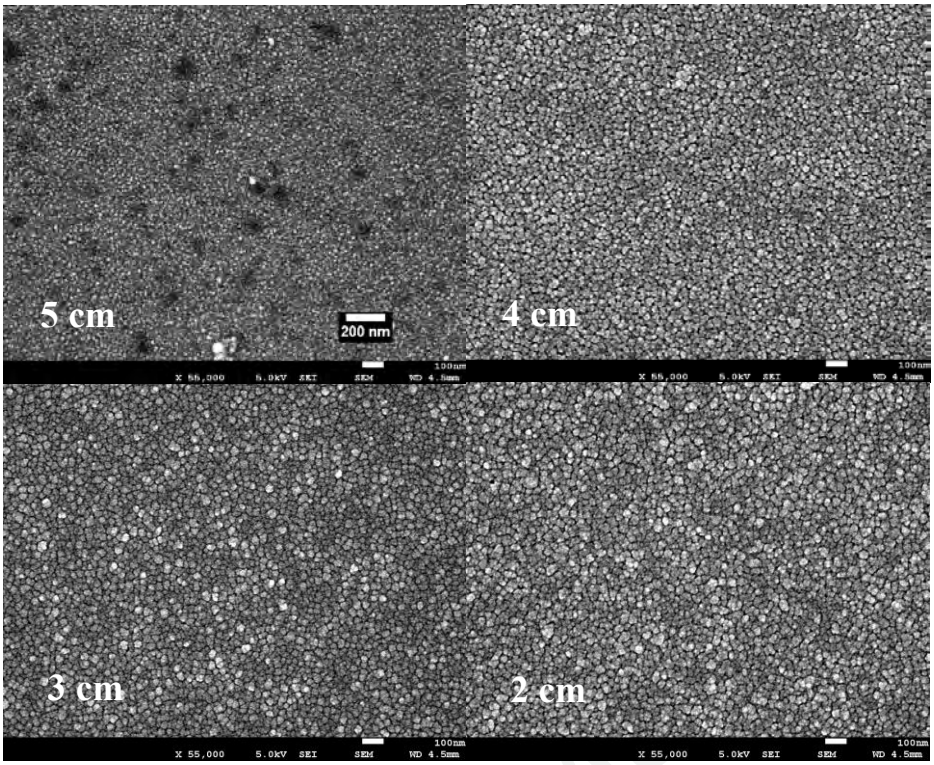


**Figure 4.2: FESEM images of Ni film as a function of Ni target-to-substrate distance at x50 K magnification.**

### 4.2.3 Grain Size and Size Distribution of Ni Catalyst.

The FESEM image of Ni film at high magnification is used for the measurement of the Ni diameter as illustrated in Figure 4.3. The grain size of the Ni catalyst was determined based on the value of the diameter obtained from the FESEM images using the Image J software.

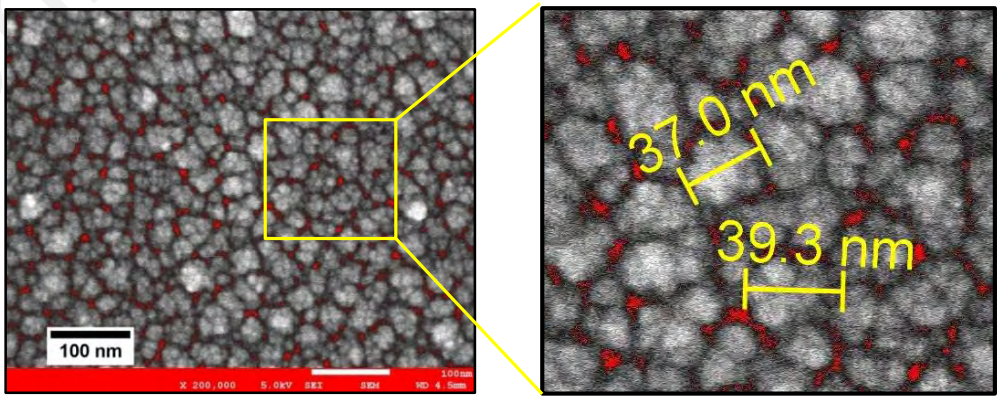


**Figure 4.3: Diameter measurement of Ni grains size using Image J software.**

University of Malaya

A quantitative analysis of the diameter distribution of Ni films is shown in Figure 4.4. The analysis revealed that the mean diameters of Ni clusters were increased with the decrease in $d_{Ni}$. It is notable that the uniformity of the Ni size distribution is as important as the Ni clusters size. The measurement obtained within a Ni films surface area was approximately 0.25±0.05 $\mu m^2$. For the sample prepared at $d_{Ni}$ of 5 cm, smaller Ni clusters were sparsely distributed with uniform size ranging from 5.0±2 nm to 25.0±0.2 nm (with average value of approximately 16.0±0.2 nm). Meanwhile, the sample prepared at $d_{Ni}$ of 4 cm had a very strong shift of the particle size distribution curves and the peaks became wider with the diameter size ranging from 10.0±0.2 nm to 65.0±0.2 nm. This resulted in the significant increase in the average value of the Ni cluster size of approximately 26.0±0.2 nm. This result indicates that the Ni cluster was distributed unevenly onto the substrate. Meanwhile, larger diameter with narrower size ranging from 25.0±0.2 nm to 60.0±0.2 nm for film sputtered at gap distance of 3 cm. This implies that the distribution size of Ni grains was more uniform at this distance. Nevertheless, with further decrease to 2 cm, the mean diameter subsequently decreased with diameter size ranging between 15.0±0.2 nm to 82.0±0.2 nm. Apparently, at gap distance of 2 cm, the distribution size of the Ni grains increased and were not uniform. The explanation and further discussion on the Ni growth with respect to the different distance of Ni target and substrate is elaborated in page 70.

University of Malaya

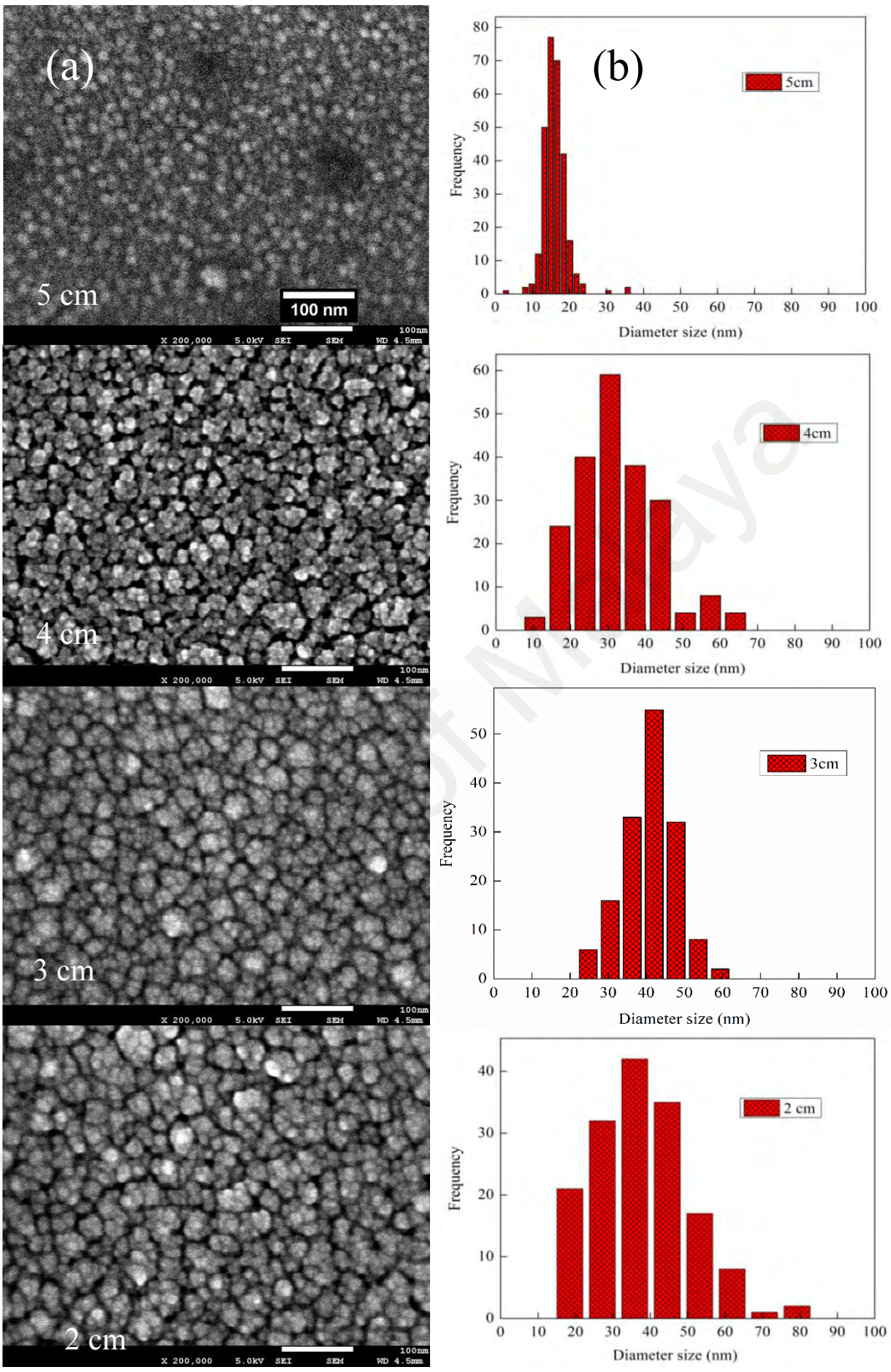


**Figure 4.4: Variation of (a) high magnification FESEM images (x200 K) and (b) size distribution of Ni grains as a function of Ni target-to-substrate.**

Figure 4.5 illustrates the variation of the mean size of the Ni grains as a function of $d_{Ni}$. The mean size of the Ni grains or the mean diameter was calculated based on the grain size distribution plots as illustrated in Figure 4.4. The mean size of the Ni grains was found to be dependent on the $d_{Ni}$, where the grain size increased with decrease in the value of $d_{Ni}$. The increase in the grain size with the decrease in $d_{Ni}$ could be due to the agglomeration of clusters of nano-crystallites.

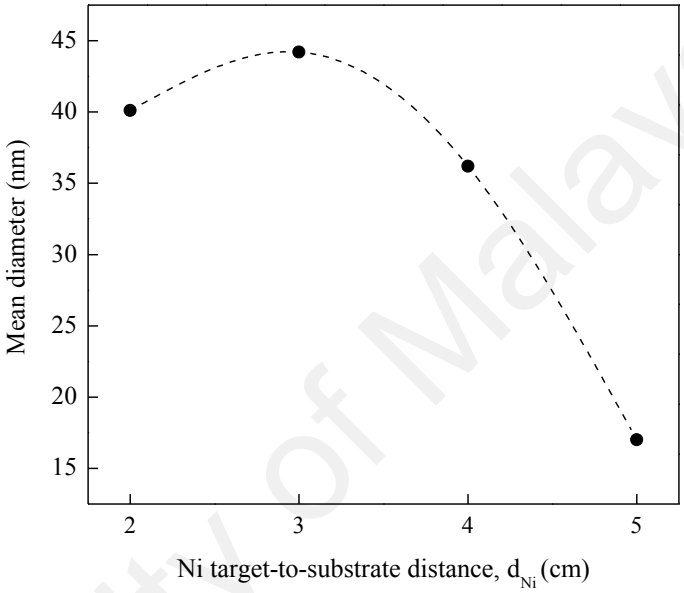


**Figure 4.5: Variation of mean diameter of Ni grains size as a function of Ni target-to-substrate distance.**

### 4.2.4 Crystalline Size of Ni Catalyst

The XRD scans of the Ni films as a function of $d_{Ni}$ are shown in Figure 4.6. The XRD patterns indicate the presence of Ni crystalline peak observed from the diffraction peak at $2\theta$ of approximately 44.5° corresponding to Ni oriented at <111> planes. An additional weak peak at 2θ of approximately 62.9° was attributed to the presence of NiO oriented at 220 planes. This implies that the Ni atoms were able to reach the substrate with sufficient energy during deposition. The higher intensity of the Ni (111) peak compared to NiO (220) indicates that the Ni films were preferred to grow as Ni (111) texture rather than NiO. This could be seen in the variation of Ni and NiO peak intensity at various gap

University of Malaya

distances as shown in Figure 4.7. The low oxide component could be due to the oxygen bonded to the Ni atoms during the sputtering process. The XRD (hkl) indices, FWHM, angle positions, and means crystallite sizes are listed in Table 4.1. The decrease in the Ni target to substrate distance to 3 cm has shown to improve the crystallite orientation along the (111) planes, which is reflected by the decrease in FWHM and corresponding increase in crystallite size. This is due to the increase in the number of crystallite domain as the coverage and thickness increases (El-Kadry et al., 1995).

From the estimated calculation using Scherrer equation (Cullity et al., 1957), the mean crystallite size of the 5 cm gap distance was approximately 17.5±0.1 nm, which was increased to approximately 27.2±0.1 nm at gap distance of 3 cm. Nevertheless, the decrease in gap distance to 2 cm had caused the reduction in the crystallite size to approximately 18.1±0.1 nm. This suggests a suppression of the crystallization as non-uniform size of grains or a certain amount of structural disorder formed at this gap distance.

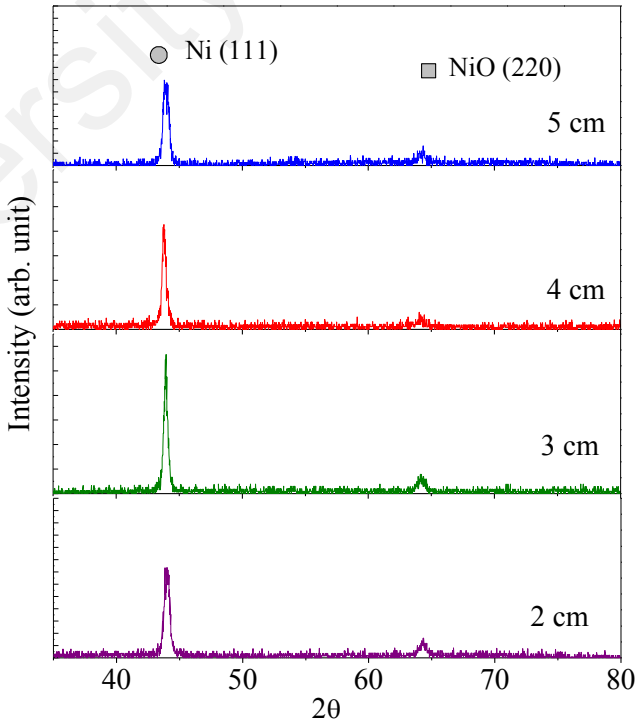


**Figure 4.6: XRD pattern of the Ni films at different thickness.**

University of Malaya

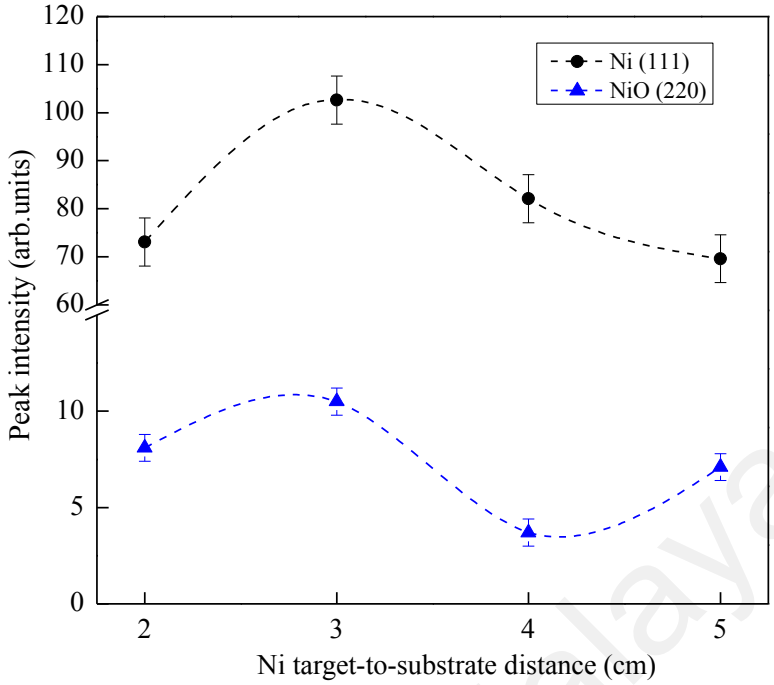


**Figure 4.7: The variation of peak intensity of Ni and NiO XRD peak as a function of Ni target-to-substrate distance.**

**Table 4.1: Phase formation, Miller indices (hkl), FWHM, angle position and mean crystallite sizes as obtained from the principle peaks of the XRD scans.**

| Ni target-to-substrate distance (cm) | Phase (hkl) | FWHM (±0.01 nm) | $2\theta$(°) (±0.1°) | Crystallite size (±0.1 nm) |
|---|---|---|---|---|
| **2** | Ni (111) | 0.47 | 44.0 | 18.1 |
| | NiO (220) | 2.06 | 64.3 | 4.5 |
| **3** | Ni (111) | 0.31 | 43.9 | 27.1 |
| | NiO (220) | 0.66 | 64.2 | 13.9 |
| **4** | Ni (111) | 0.39 | 43.7 | 21.9 |
| | NiO (220) | 3.95 | 63.7 | 2.3 |
| **5** | Ni (111) | 0.49 | 43.9 | 17.5 |
| | NiO (220) | 1.89 | 64.2 | 4.9 |

### 4.2.5 Variation of Mean Diameter and Crystallite Size of Ni Catalyst

A comparison of Ni grain size and crystallite size of the Ni film as a function of $d_{Ni}$ are presented in Figure 4.8. The Ni grain size was determined based on the mean diameter size obtained from FESEM images, while the crystallite size was estimated using Scherrer equation from the most dominant XRD Ni (111) peak. The grain size and crystallite size were increased with the decrease in the electrode distance up to 3 cm, and decreases at

University of Malaya

electrode distance of 2 cm. The variation in both grain and crystallite sizes were similar but the values of crystallite size were slightly lower compared to their corresponding grain sizes. These differences indicate that the grains consist of clusters of crystallites.

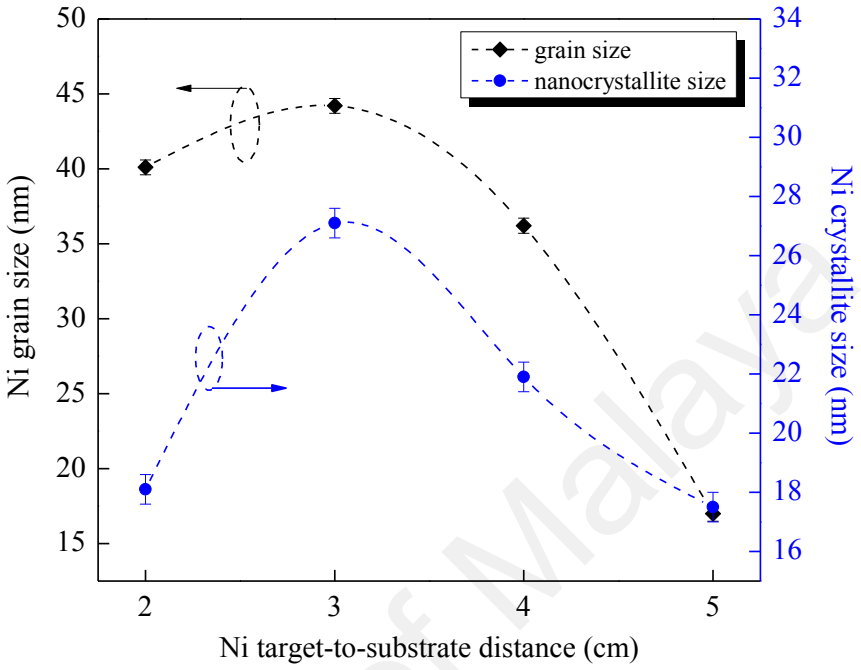


**Figure 4.8: Variation of grain size and nanocrystallite size of Ni at $d_{Ni}$.**

### 4.2.6 Influence of Ni Target to Substrate Distance on the Growth of Ni Catalyst by RF Sputtering Technique

The results demonstrate that the Ni target to substrate distance strongly influenced the growth of the Ni catalyst by RF sputtering. Figure 4.9 illustrates the suggested mechanism on the influence of target to substrate distance ($d_{Ni}$) in the sputtering system on the growth of Ni catalysts. The sputtering process applied for the growth of the Ni catalyst was powered by radio-frequency (RF) of 13.56 MHz. The upper electrode was connected to the RF generator, while the lower electrode was grounded. Ar gas was introduced into the system as the sputtering agent during the growth process. Moreover, the Ar gas was discharged to form the positively charged Ar ions. When the target electrode was negatively biased, the energetic Ar ions moved at high speed towards it and sputtered off Ni atoms from the Ni target. Later, these sputtered Ni atoms were deposited on the $SiO_2$

University of Malaya

substrate placed on the lower electrode. Meanwhile, when the RF electrode was positively biased due to the change in the polarity of the RF power, the Ar ions changed the direction towards the substrate. This allows Ar atoms to bombard the substrate and results in the broken Si-O bonds at the surface. The released O atoms created defects on the substrate surface and acted as nucleation sites for Ni growth. The released O atoms from the broken bonds of the Si-O formed NiO phase in the structure of the Ni films.

The thicknesses of Ni were varied by adjusting the Ni target-to-substrates distance. The changes in the gap distance had affected the sputtering rate by influencing the pathway of the Ar gas and Ni atoms (Yasuda, 2004). At larger gap distance (5 cm), the possibility of Ni atoms colliding with the Ar gas molecules was higher due to the large deposition path, which in turn increased their kinetic energy loss. This condition led to a significant decrease in the mean free path of Ni atoms reaching the substrate (Ishihara et al., 1998; Xu et al., 2001). Moreover, the decrease in electric field due to larger gap distance had lowered the energy of ion bombardment on the Ni surface and $SiO_2$ substrate surface. This resulted in the formation of sparsely distributed defects along with nucleation sites on the $SiO_2$ surface, which in turn resulted in the growth of sparsely distributed smaller size of Ni clusters.

Meanwhile, the lower gap distance increased the thickness of Ni and the Ni clusters sizes. The shorter deposition path due to smaller gap distance reduced the probability of Ni atoms to collide with gas atoms. This condition allowed direct deposition of Ni atom onto the substrate by sputtering the Ni at a particular angle with respect to the target's normal and travel at the same angle in the opposite direction (Kar et al., 2008), which in turn produced more uniform Ni films. Furthermore, lower gap distance promoted the agglomeration of the Ni particles, which created larger cluster size. Consequently, this increased the deposition rate of the Ni film (Andújar et al., 2002).

University of Malaya

The energy of ion bombardment on the Ni surface and $SiO_2$ was higher at the lowest gap distance (2 cm). This led to the higher sputtering effects of Ni atoms and higher bombardment effects on the substrate surface. Thus, this resulted in higher growth of Ni film along with higher Ar bombardment effects on the Ni film surface. This Ar bombardment effects resulted in the formation of smaller Ni clusters and crystallite size with non-uniform Ni island and concurrently induce the formation of some oxygen impurities. The formation of oxygen impurities on the Ni island might also due to the small amount of oxide layer that passivates on the surface of the reused Ni target.

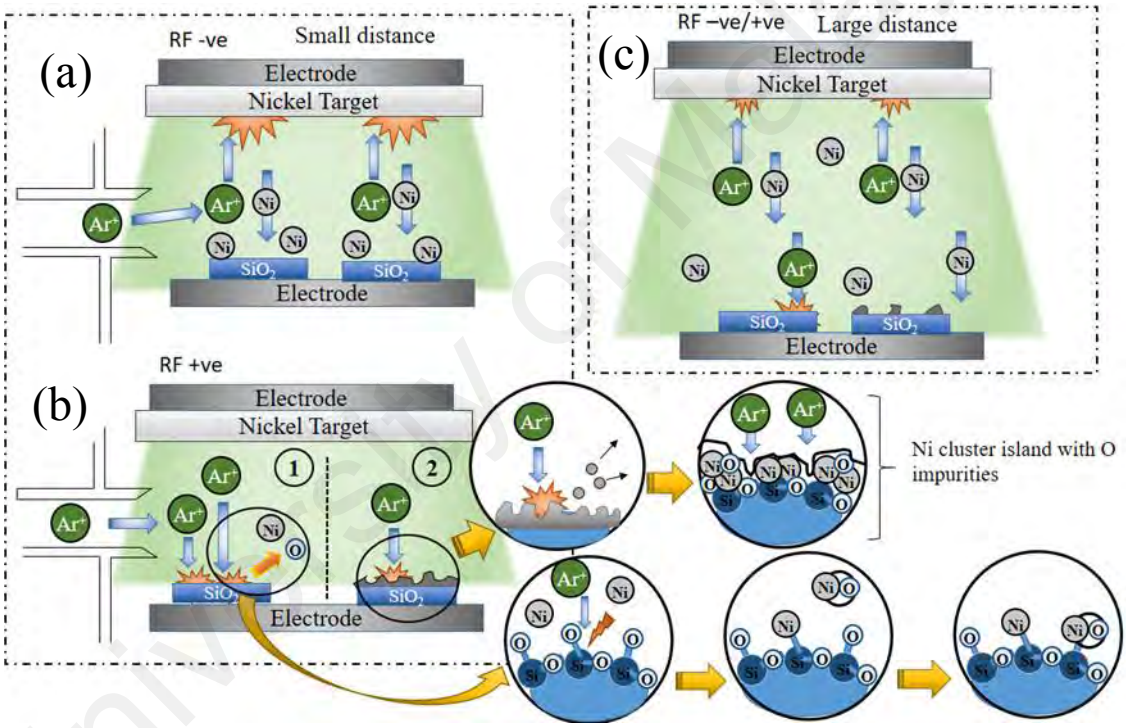


**Figure 4.9: Schematic diagram of Ni sputtering (a) on the Ni target surface and (b) on the substrate surface at small Ni target-to-substrate distance; and (c) at large Ni target-to-substrate distance.**

University of Malaya

## 4.3 Effects of Ni Thickness on the Growth of Transfer-Free Graphene from Plasma Enhanced Chemical Vapour Deposition Technique

In this work, transfer-free graphene films were grown onto Ni layer at various thickness values, which were obtained in the previous section. For ease of reference, the thickness measurements have been rounded to the closest corresponding values including 50 nm, 100 nm, 150 nm and 200 nm. Furthermore, the graphene films that were deposited at the Ni-substrate interfaces, where carbon atoms diffused through these Ni thicknesses and subsequently were formed between these interfaces. It should be noted that the graphene films were formed from the discharged of methane ($CH_4$) and hydrogen ($H_2$) gases using PEVCD at low temperature. In this study, $CH_4$ to $H_2$ gas flow rate, substrate temperature and deposition time were fixed at 10 sccm to 100 sccm, 400 °C and 5 minutes, respectively. In addition, the graphene films were analyzed after the top nickel layers were removed using wet etching process. These films were used to determine the thickness of Ni and properties.

### 4.3.1 Structural Properties of PECVD Transfer-Free Graphene after Ni Etching

The formation of graphene films after the etching of Ni films were investigated by using the Raman spectra of the graphene films as a function of Ni thickness, as shown in Figure 4.10. For all measurement, the incident beam of the laser was normal to the sample surface. The spectra were deconvoluted using standard method with both Gaussian and Lorentzian curve fitting. Two prominent peaks at 1350 and 1580 $cm^{-1}$ were observed for all films, which were typically attributed to D and G bands, respectively (Allen et al., 2009). The G band corresponds to the $E_{2g}$ vibration mode of $sp^2$ carbon atom (Ferrari et al., 2006), while the D band is associated with the disordered arrangement of six-fold aromatic carbon rings (Kim et al., 2005; Lee et al., 2003; Wu et al., 2009). Moreover, two more peaks were observed at 2700 $cm^{-1}$ and 2900 $cm^{-1}$ in the spectra corresponds to 2D

University of Malaya

and D'+G' bands, respectively. The 2D band is related to double-resonant Raman scattering, which is associated with microstructural disorder, crystallinity and number of layers of graphene sheets (Ferrari et al., 2006). The 2D peak intensity and its FWHM are typically used to determine the thickness and number of graphene sheets (Eastman et al., 2014). On the other hand, the D'+G' band is related to the formation of defects in the graphene microstructure.

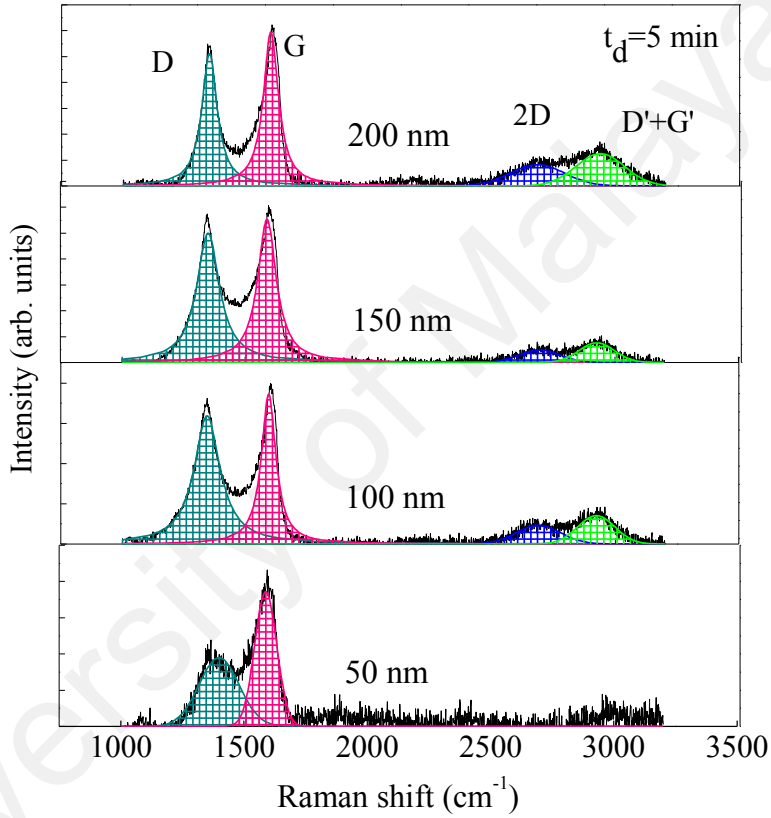


**Figure 4.10: Raman spectra of transfer-free graphene as a function of $d_{Ni}$.**

From the Raman spectra, the $I_D/I_G$ ratio and the FWHM of D and G peak values were calculated using the fittings and the variation of these values as a function of Ni thickness as shown in Figure 4.11. For film grown on Ni thickness of 50 nm, the broad peak values of both D and G bands led to a very high value of their FWHM. The high values together with the decrease in the G peak position and the absence of the 2D peak for this film are typical characteristic of amorphous carbon film. This implies that at low Ni thickness graphene film could not be formed. This is related to the sparse distribution of Ni

University of Malaya

coverage as observed in the previous FESEM image, whereby the exposed $SiO_2$ substrate along the wide separation between the Ni grains allowed the direct deposition of carbon film onto the substrate. Therefore, the results related to the thickness of Ni is disregarded for further discussion.

The D and G bands became narrower with further increase in Ni thickness. As such, the appearance of 2D peaks in the spectra confirmed the formation of graphene films. Nevertheless, low intensities and broad 2D peaks suggest that the films formed were multi-layered graphene. The reduction in the FWHM of D and G values when Ni thickness were increased from 100 to 200 nm indicates the formation of well-ordered graphitic structure of these graphene films with further increase in Ni thickness (Malard et al., 2009b). This is in line with the corresponding decrease in $I_D/I_G$ ratio of the films, which indicates the formation of well-ordered graphene structure. This is attributed to the reduction in the defects of their rings microstructure (Ferrari, 2007; Malard et al., 2009a).

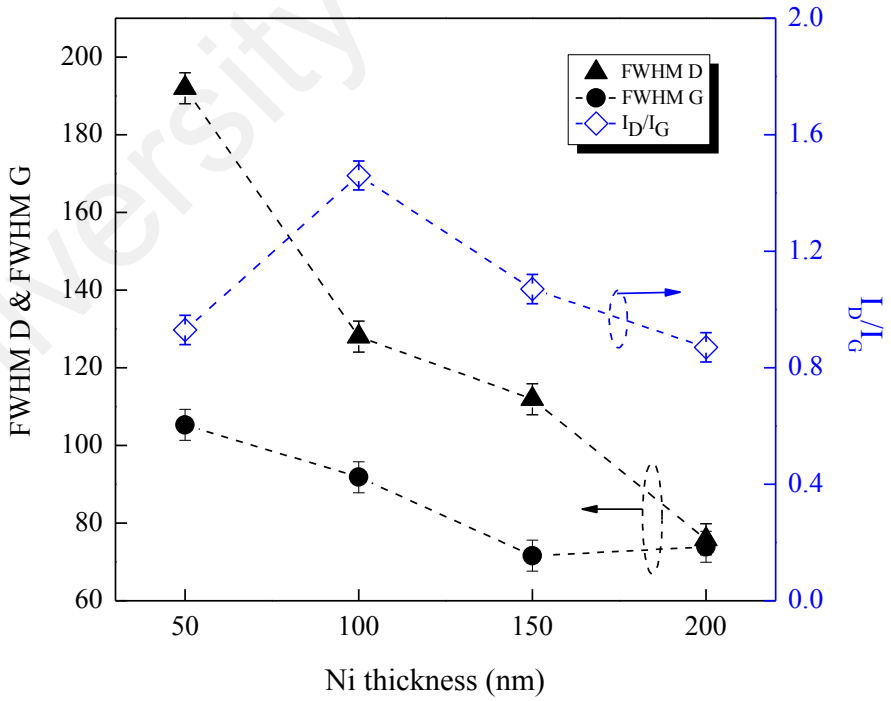


**Figure 4.11: Variation of FWHM D, FWHM G and $I_D/I_G$ obtained from deconvoluted of Raman spectra as a function Ni thickness.**

University of Malaya

The thickness and quality of these graphene films were further investigated using the 2D and D'+G' peaks, which are related to the degree of graphene layers and defects (Srinivas et al., 2010). The variations of FWHM 2D and the value of area under the curve of D'+G' bands are shown in Figure 4.12 and the area can be reflected as a function of Ni thickness. It should be noted that since the films deposited at Ni thickness of 50 nm was identified as an amorphous carbon, this finding was omitted in the subsequent discussion. Moreover, the FWHM of the 2D peak was decreased when the Ni thickness was increased from 100 to 150 nm, suggesting a decrease in a number of graphene layers. Nevertheless, upon increasing the thickness of Ni to 200 nm, the corresponding increase in FWHM of its 2D peak suggests a sudden increase in graphene layers (Ferrari, 2007; Malard et al., 2009a).

There was a significant increase in the D'+G' value with the increase in graphene layer at the highest Ni thickness. This indicates the increase in the films defects. In contrast, apart from its low value of $I_D/I_G$ ratio, the graphene grown at Ni thickness of 150 nm also exhibited the lowest value of D'+G'. This result implies that the film grown on Ni thickness of 150 nm was well-ordered with less defective graphene.

In general, the Raman characteristic of these samples had high and significant D peak intensities, together with the existence of D'+G' peaks. This implies that application of low-temperature PECVD technique could successfully produce transfer-free graphene films though the films were significantly defective.

University of Malaya

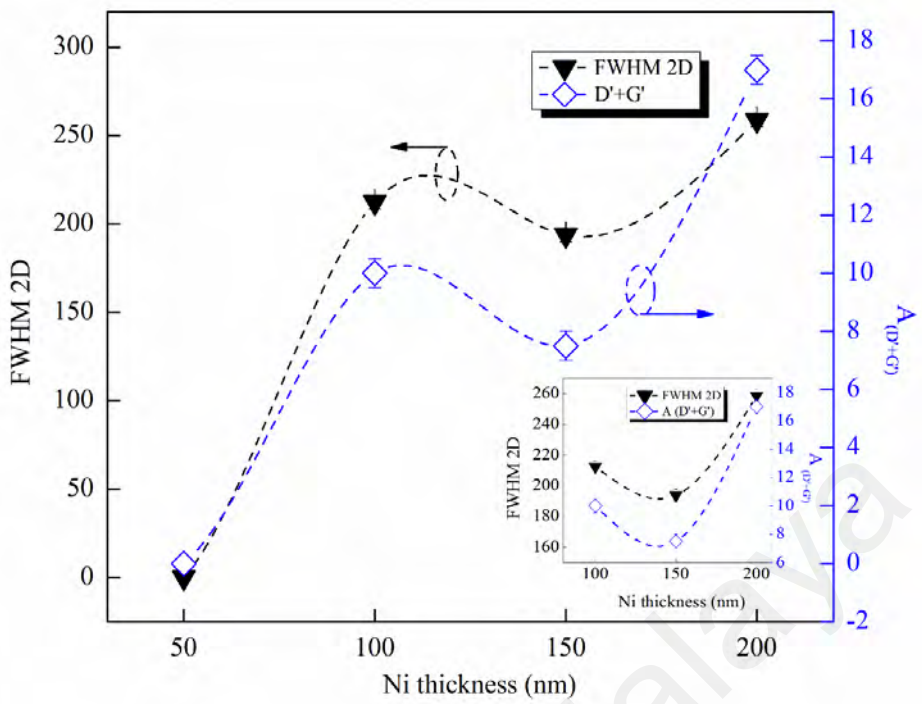


**Figure 4.12: Variation of FWHM 2D and A (D'+G') as a function of Ni thickness. The insert is the variation of FWHM 2D and A $_{(D'+G')}$ is known as a function of Ni thickness ranging from 100 nm to 200 nm.**

### 4.3.2 Morphological Properties of PECVD Transfer-Free Graphene

The morphological properties of the graphene films were studied using FESEM and HRTEM. Thus, the film with the optimized properties obtained from the growth of graphene using Ni thickness of 150 nm (Figure 4.13). The criteria for selection is based on the formation of less defects and well-ordered microstructure of the graphene film. The FESEM image as shown in Figure 4.13(a) displays a darker image that represents the area of the graphene film, while the brighter image represents the exposed substrate. The differences could be seen in Figure 4.13(b) and (c). The film is easily identifiable with the presence of wrinkle as typically observed for graphene sheets (Muhammad et al., 2014). The growth area of the film was very large (>100 μm) despite the presence of short tears in a certain area of the film, which may have occurred during the etching process.

University of Malaya

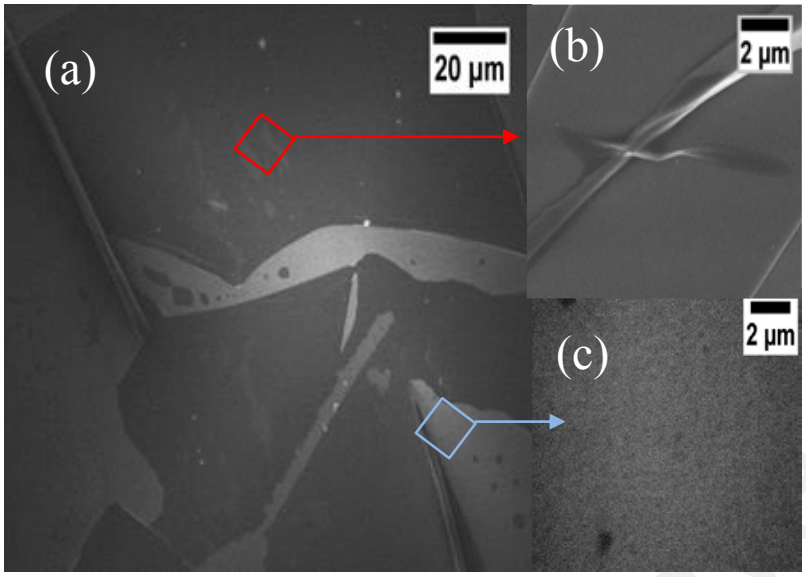


**Figure 4.13: (a) FESEM image of the graphene grown on $SiO_2$ substrate after the Ni etching process. The parts labelled as (b) and (c) indicate the graphene films and the substrate, respectively.**

The HRTEM images of the freestanding graphene layers on standard copper grid is shown in Figure 4.14(a). The high magnification of the HRTEM image in Figure 4.14(b) indicates a multilayered graphene, which was determined by the number of lines at the films edges as marked by a green box. The fringes with an interplanar spacing of 0.37 nm as shown in Figure 4.14(c) matched well with the layered structure of graphene sheets. Additionally, the estimated thickness of the graphene was approximately 5.0±0.4 nm. This HRTEM images indicate that the sheet is formed as few-layered graphene. This is in agreement with the Raman result. Moreover, the Fast Fourier Transform (FFT) image that was performed in the region is indicated by a red box in Figure 4.14(d). The image demonstrates the hexagonal pattern, which reveals the six-fold feature of graphene. Moreover, the corresponding HRTEM image also reveals the honeycomb structure of the graphene sheet.

University of Malaya

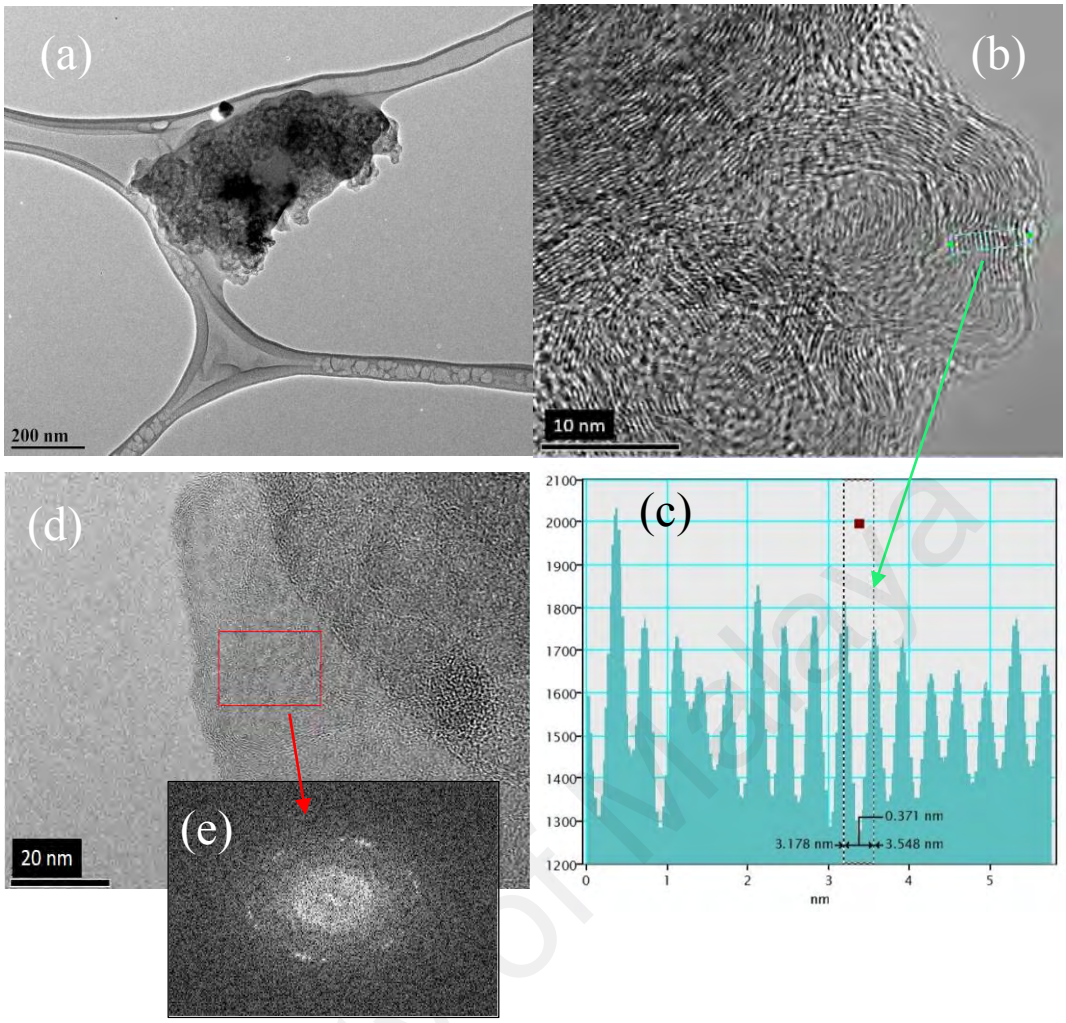


**Figure 4.14: (a) The HRTEM images of the transfer-free graphene on the Cu grid, (b) the high magnification of the HRTEM image, (c) intensity profile along the green box, (d) region of HRTEM image and (e) corresponding FFT image for highlighted part in figure (d).**

### 4.3.3 XPS Depth Profile of PECVD Graphene/Ni/Graphene/$SiO_2$ Sample

The XPS was performed for elucidating the formation process of graphene on Ni film. Figure 4.15 illustrates the XPS depth profile of the Ni/graphene/$SiO_2$ substrate sample prior to Ni catalyst etching. The XPS indicates the evidence of graphene formation at the Ni-$SiO_2$ substrate interface after the deposition process. Moreover, the saturation of Ni atomic concentration at approximately 10 nm indicating that the C started at a depth of approximately lower than 10 nm. This demonstrates the formation of thin layer graphene on top of the Ni film. In addition, the results of XPS depth profile suggests that the majority of carbon atoms were confined deep into the Ni and substrate surface during the

University of Malaya

deposition process to act as a carbon source for graphene formation. Moreover, the C atoms in the Ni matrix displayed high C atoms diffusivity to enable their arrival at the catalyst or substrate interface.

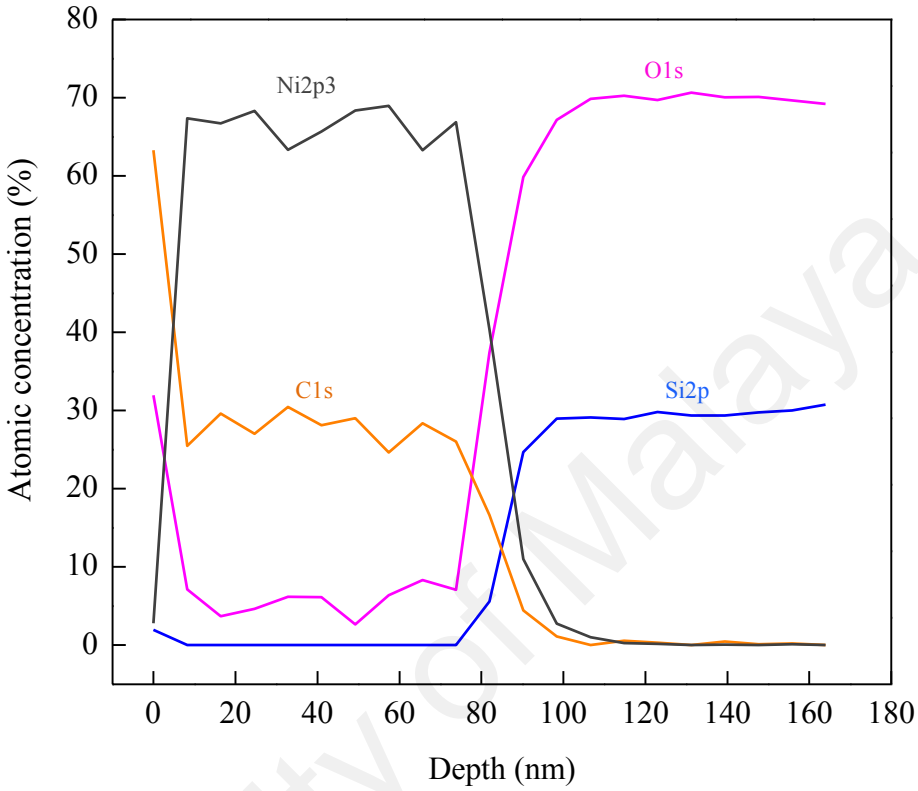


**Figure 4.15: XPS depth profile of Ni/graphene/$SiO_2$ substrate.**

### 4.3.4 The Influence of Ni Thickness on the Growth of PECVD Graphene

The usage of Ni, which acted as catalyst for graphene growth has resulted in successful deposition of transfer-free graphene by PECVD. The high solubility or diffusion of carbon in Ni at low temperature (López et al., 2004) has demonstrated an important factor for the growth of the PECVD transfer-free graphene. Moreover, for low-temperature growth of graphene using Ni, 400 °C is the critical temperature for the carbon to diffuse in or out from the Ni. Additionally, the carbon diffusion is kinetically inhibited at the temperature lower than 400 °C (Lahiri et al., 2011). Peng et. al, in their work on graphene growth of Ni catalyst by radio frequency (RF) PECVD proposed a similar general

University of Malaya

mechanism that was adopted in this study. The mechanism suggested by the authors indicated that the RF plasma is utilized to enhance the decomposition of methane into carbon species and randomly diffused in the interstices of Ni atoms. During the rapid cooling process, the diffused carbon species precipitate and segregate into hexagonal ring structure of graphene (Peng et al., 2013). This mechanism is non-specific in which insufficient information available with regard to this. Nonetheless, based on the diffusion-segregation model proposed by Peng et. al, a growth mechanism and detail explanations on the growth of the transfer-free graphene are described in detail.

The deposition of PECVD graphene on Ni catalyst has been described as a two-step mechanism. Prior to deposition, hydrogen is used for the pre-treatment (cleaning and crystallization) of the Ni. Its interaction with the Ni surface can influence the subsequent $CH_4$ chemisorption kinetics (Losurdo et al., 2011). Furthermore, an improved Ni surface enables availability of more reaction sites for $CH_4$ chemisorption and dissociation.

The first step in the dissociation process to be considered is the dissociative chemisorption of $H_2$ and physisorption of $CH_4$ on surface sites of Ni. The dissociation of the gases was simplified based on the chemistry model proposed by a previous study (Kline et al., 1989), where the electron-electron, electron-ion, and ion-ion collisions are not included in this discussion. For the discharge kinetics, elastic scattering between neutrals are considered and electron impact to $CH_4$ and $H_2$ are considered as according to the reactions (4.1), (4.2) and (4.3), respectively

$$CH_4 + e^- \rightarrow CH_3 + H + e^- \quad (4.1)$$

$$CH_4 + e^- \rightarrow CH_4^+ + e^- + e^- \quad (4.2)$$

$$H_2 + e^- \rightarrow H + H + e^- \quad (4.3)$$



University of Malaya

It should be noted that the sticking coefficient of hydrogen is lower for Ni but $CH_4$ easily physisorbs on the Ni surface due to lower activation energy required for $CH_4$ physisorption on Ni.

The second step is the dehydrogenation of $CH_4$ according to the following reaction:

$$CH_4 + e \rightarrow CH_3 + H \quad (4.4)$$

$$CH_3 + e \rightarrow CH_2 + H \quad (4.5)$$

$$CH_2 + e \rightarrow CH + H \quad (4.6)$$

$$CH \rightarrow C + H \quad (4.7)$$

The dissociation of $CH_4$ molecules resulted in the formation of $CH_3$ radicals, where the dissociative chemisorption of $CH_3$ and H in the reaction (4.4) occurs on top of the Ni surface. As the dissociation continued, the $CH_3$ radicals were formed following the secondary reactions of other $CH_n$. This process usually forms C-C weak bond, in which the C atoms diffused into the Ni layer, where C nucleation and segregation occur.

The important differences between the graphene grown onto Ni surface and transfer-free graphene are the thickness of the Ni layer and the cooling rate of the deposition process. Generally, the thickness of Ni layer for growing graphene on Ni surface is above 200 nm. Meanwhile, for transfer-free graphene, a lower Ni thickness is required to ensure that the C atoms could diffuse deep into these Ni thicknesses and reaching the $SiO_2$ substrate. Moreover, slower cooling rate is preferred suggesting that the excess of diffused carbon atoms will be provided with sufficient energy to precipitate repeatedly. This is important to control the thickness of the graphene formed onto the substrate. The two factors state above are important, where if the Ni thickness is too thick, the diffused

University of Malaya

carbon atom could not reach the substrate. Meanwhile, if the cooling rate is rapid, more carbon atoms will be formed at the bottom of the thin Ni layer.

The influence of Ni thickness on the growth of transfer-free graphene by PECVD is depicted in Figure 4.16. The depicted model formed based on a previous study (Pan et al., 2013). In this work, graphene was grown from the diffusion of C through the nano-crystallite sized Ni grains and formed as nano-crystalline graphene (nc-G). These nc-G are formed as a result of isotropic precipitation of C, which settled down at the interface between the Ni and $SiO_2$ substrate during diffusion. During the deposition, C atoms in the plasma with sufficient activation energy migrate towards both the Ni-free surface (area between Ni grains boundaries and Ni top surface) and Ni/$SiO_2$ interface under the driving force of the C concentration gradient (Kim et al., 2005). The nc-G were initially grown at the interface due to higher mobility of C on the Ni-free surface compared to at the interface. The remaining diffused C atoms precipitated on the top surface of the Ni and at the Ni grains boundaries during the cooling process. For graphene grown at Ni thickness of 50 nm, the C that formed at the Ni surface and its boundaries were linked up with the nc-G that formed on the interface as the Ni layer was too thin. Due to the strong link between the top C layer and nc-G layer, both layers were retained on the $SiO_2$ substrate upon removal of Ni, which resulted in the formation of thick carbon films instead of the nc-G layer alone.

There was no physical link between the C on top of the Ni surface and the nc-G for graphene grown at higher Ni thickness (>50 nm). This is due to the large distance between the Ni surface and the Ni/$SiO_2$ interface at higher Ni thickness. During the etching process, the lack of linkages allows the top layer to be separated from the nc-G. This top layer would eventually float above the acid solution and removed. This allows only the nc-G, which has high adhesion to the $SiO_2$ substrate to be remained.

University of Malaya

It should be noted that the Ni thickness influenced the Ni grain size and the formation of graphene layer that was dependent on the Ni grains boundaries. The increase in the Ni grain size elevated Ni grains boundaries and resulted in lower number of graphene layer. The higher Ni thickness with larger Ni grains size lowered the diffusion rate of C atoms, reaching the Ni/$SiO_2$ interface and reduced the C precipitation rate at the grains boundaries. Consequently, this resulted in lower concentration of C at the $SiO_2$ substrate and the grains boundaries.

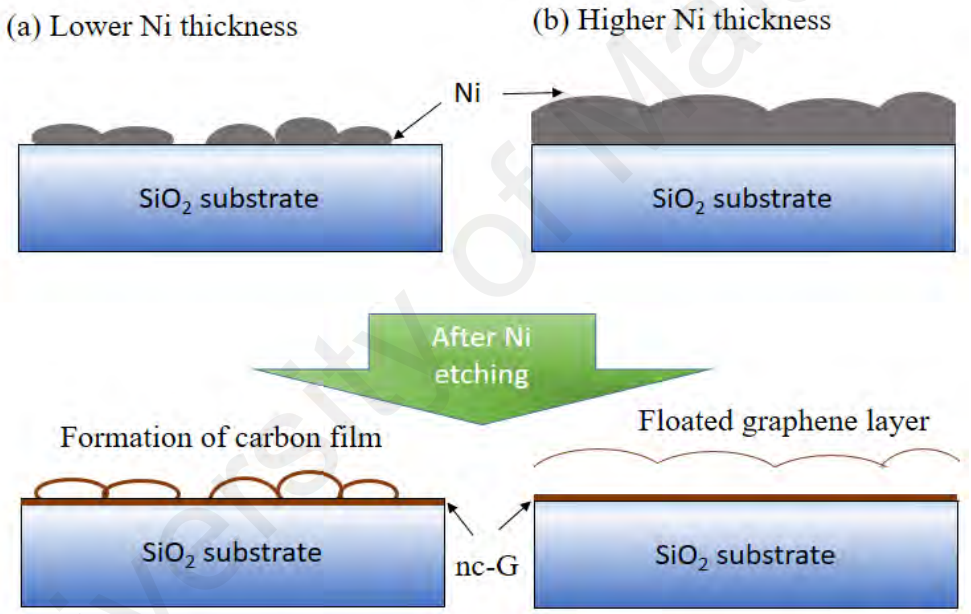


**Figure 4.16: Schematic illustration of the growth model for (a) thin Ni layer with small Ni grains: carbon layer grows around Ni grains and link up with the nc-G layer on the substrate surface, and (b) thick Ni layer with large grains: graphene grows atop of the Ni layer and an nc-G layer formed at the interface of Ni and $SiO_2$ substrate.**

## 4.4 Summary

Transfer-free graphene films were grown from PECVD using Ni catalyst at low temperature. The variation in Ni target to substrate distance, $d_{Ni}$ was found to influence the formation and growth of the Ni films onto the substrate. The higher value of the $d_{Ni}$

University of Malaya

resulted in lower Ni films thickness with smaller diameter size of non-uniform thickness with well-ordered Ni clusters size. The thickness and formation of these Ni grains influenced the growth of graphene onto the $SiO_2$ substrate. The main function of the Ni thickness towards graphene growth is to limit the diffusion of carbon. Consequently, this controls the growth of carbon in the Ni substrate interface. Henceforth, the thickness of the Ni layer and the grains size distribution, which correspond to its grain boundaries are crucial in the graphene formation.

Moreover, lower Ni thickness has resulted in the growth of carbon film, where the high growth rate led to an excessive deposition on the substrate. During additional increase in Ni thickness up to 100 nm, the Ni was sputtered at larger grains size onto $SiO_2$ substrate, where the graphene started to form. Fundamentally, graphene was formed at the best condition at Ni thickness of 150 nm as well-ordered graphene with less defects. This is the result of the formation of well-ordered Ni grains with larger size. Moreover, Ni film limits the growth of graphene at Ni-substrate interface and produces lower number of graphene layers. Nevertheless, at the highest Ni thickness (200 nm), the Ni grains highly bonded with the oxygen, which in turn resulted in growth of highly defective graphene film. The formation of such graphene is anticipated to be correlated with the thickness with higher amount of defects and grains boundaries of the Ni films.

University of Malaya

# CHAPTER 5: SYNTHESIS OF TRANSFER-FREE GRAPHENE USING NICKEL CATALYST FROM HOT-FILAMENT ASSISTED PLASMA ENHANCED CHEMICAL VAPOUR DEPOSITION

## 5.1 Introduction

This chapter describes the improvement of the PECVD transfer-free graphene by applying the addition of hot-filament into the deposition system. The system is henceforth named as HF-PECVD technique. It should be noted that all the following deposition were performed using Ni buffer layer with the thickness of 150 nm, which was optimized in this study.

A total of three studies are presented in this chapter. The first study introduces the deposition of transfer-free graphene film using PECVD with the addition of hot-filament. This is aimed to compare the graphene film without the use of hot-filament as described in Chapter 4. The effects of thermal heat from the hot-filament on the Ni films after the deposition of graphene were determined. Further investigation on the properties of transfer-free graphene film using HF-PECVD technique is presented in regard to their structural, morphological, and chemical properties. The second study investigates the effects of various deposition durations to analyze the improvement of the graphene films.

As such, the structural, chemical bonding, and morphological properties of the graphene were determined using Raman spectroscopy, XPS and HRTEM analysis, respectively. The third study is aimed to investigate the effects of substrate temperature and to strike a balance between graphene quality and low-temperature deposition. In addition, exploratory studies were performed to elucidate whether the substrate temperature could be lowered to maintain or improve the quality of the graphene. The current study is aimed to investigate the optimum quality of transfer-free graphene at the minimum deposition time and low deposition temperature. Moreover, the studies on the

University of Malaya

wettability and magnetic properties of these films are described in regard to their morphological properties, chemical bonding and formation of defects in the films. This chapter describe the improvement of the PECVD transfer-free graphene by employing the addition of hot-filament into the deposition system. The system is henceforth named as hot-filament plasma enhanced chemical vapour deposition (HF-PECVD) technique. It should be noted that all the following deposition were done using Ni buffer layer of thickness 150 nm which was determined as the optimized condition from the previous Chapter 4.

## 5.2 Effects of Thermal Heating on the Morphology, Elemental Depth Profile and Structural Properties of HF-PECVD Transfer-Free Graphene

In this section, transfer-free graphene was deposited using HF-PECVD technique. The filament was placed directly on top of the substrate with a distance approximately of 1 cm to provide higher temperature radiation during the film growth. The filament temperature was fixed at 1600 °C. At this temperature, the heating from the filament failed to cause any gas phase reaction. Nonetheless, it increased the deposition temperature from 400 °C to 620 °C. Additionally, other deposition parameters were fixed similar to the growth of graphene using PECVD as indicated in the previous chapter. The effects of the thermal heating by hot-filament on the morphological, chemical bonding and structural properties of the grown Ni and subsequent growth of graphene were compared with the graphene grown from previous PECVD technique.

### 5.2.1 Morphological Properties of PECVD and HF-PECVD Graphene/Ni before Ni Etching

The surface morphology of the graphene formed on the Ni layer was investigated based on the AFM results. Figure 5.1 illustrates the two-dimensional AFM images of

University of Malaya

graphene deposited on Ni films using PECVD and HF-PECVD technique. The AFM result demonstrates that the film grown from PECVD formed as nanosized clusters of nanocrystalline graphene, while film grown from HF-PECVD exhibited larger size bolder-like cluster. It should be noted that for both deposition, the size of Ni catalyst and dimensions were similar prior to any heat treatment or graphene deposition as illustrated in Figure 5.1. The comparison between the images of raw Ni catalyst and graphene grown using PECVD revealed that the grain size and grains boundaries remained almost identical. This demonstrates that the plasma itself did not influence or change the morphology and structure of the Ni catalyst.

The grains size and boundaries in Ni were significantly increased with the existence of hot-filament in the HF-PECVD system that released heat radiation. In addition, the significant increase in the size occurred due to the tendency of self-assembly of nanocrystal Ni grains at high-temperature. According to a previous study, in the self-assembling process, the nano-sized Ni grains rotate slightly toward each other and agglomerate in group to form large island-like structure that consisted of coalescence of nano-sized grains as seen in Figure 5.1(c) (Sasi et al., 2007). This large island-like structure resulted in larger grains size boundaries.

University of Malaya

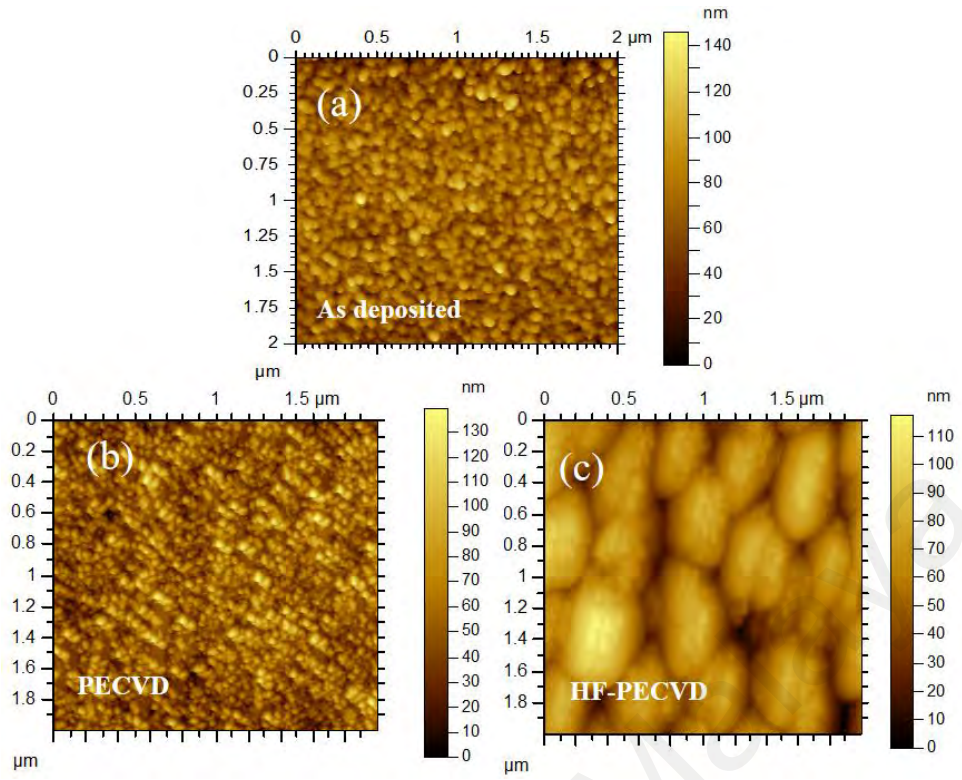


**Figure 5.1: AFM images of (a) as deposited Ni film, and graphene deposited on Ni films before etching using (b) PECVD and (c) HF-PECVD technique.**

Further investigation of both films were carried out using FESEM images. The FESEM images illustrated in Figure 5.2 demonstrate the differences in grains size using two different techniques, namely PECVD and HF-PECVD. The changes in the grain size from nano to micro size for graphene grown from PECVD to HF-PECVD were consistent with the AFM results. Nevertheless, the grains were distinctly separated from each other for sample grown from HF-PECVD. In addition, the cross-sectional images of FESEM were carried out to validate these formations. Interestingly, the FESEM image demonstrates that the graphene growth from HF-PECVD was formed as compact spherical Ni grains or island. In contrast, for graphene grown from PECVD, the Ni was formed as compact films with nano-sized grains boundaries. The results indicate that higher temperature mutates the Ni catalyst. The deformation of these grains is due to the force rotation in response to external stresses exerted upon it by the nearby grains. Moreover, the grain rotation during deformation is accomplished by a microscopic

University of Malaya

dislocation glide on multiple active slip systems in the grains. This condition can also be caused by an extensive grain boundary sliding and diffusion, which results in microscale void between the grains (Ma, 2004).

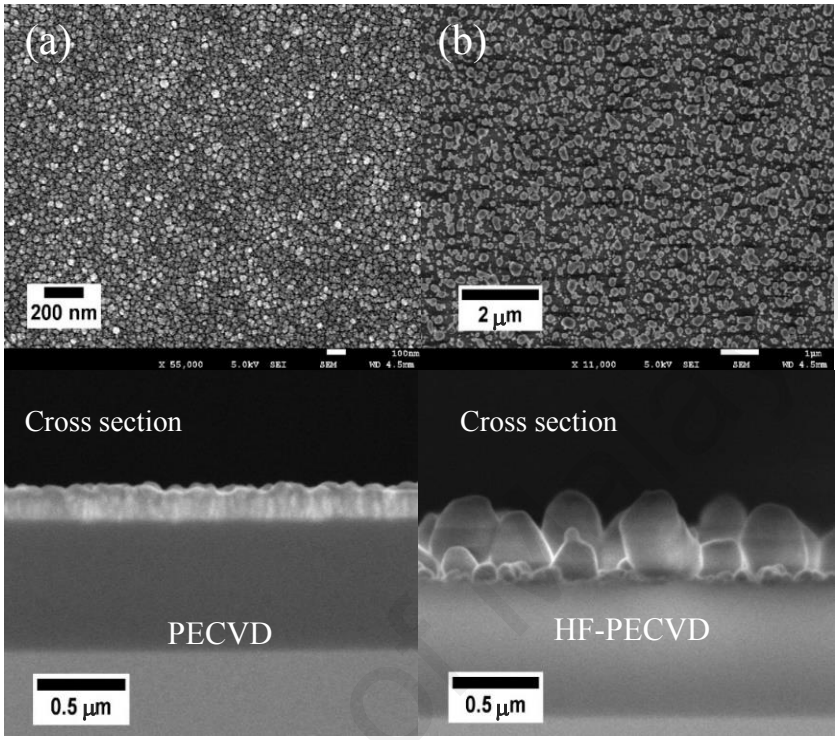


**Figure 5.2: FESEM images of graphene formed using Ni catalyst from (a) HF-PECVD and (b) PECVD technique.**

The EDX mapping were applied to further confirm the component and element distribution as shown in Figure 5.3. The inserted images were the EDX spectroscopy of the samples, which indicate that both films were composed of C, Ni, O and Si elements. Two prominent peaks, which are C and Ni were observed in the EDX spectrum for film grown from PECVD. Meanwhile, Ni element was more pronounced in the spectrum for HF-PECVD film due to the agglomeration of the Ni. The difference between the elemental mapping images could be focused on the distribution of the C and Ni concentration in the films. The images in Figure 5.3(c) and (d) demonstrate that the elements were observed to form uniform PECVD films but selectively congregated towards the Ni for HF-PECVD film. The appearance of the uniformity for PECVD film

could be also attributed to the increased in thickness of graphene films formed, which resulted in higher intensity of C to Ni ratio detected in EDX spectrum analysis. On the other hand, for HF-PECVD film, the C film formed were much thinner and thus congregation of C around the Ni catalyst would provide false impression that the C is concentrated preferentially at the sites of the agglomerated Ni. This is supported by the lower relative peak intensity of the C in EDX spectrum.

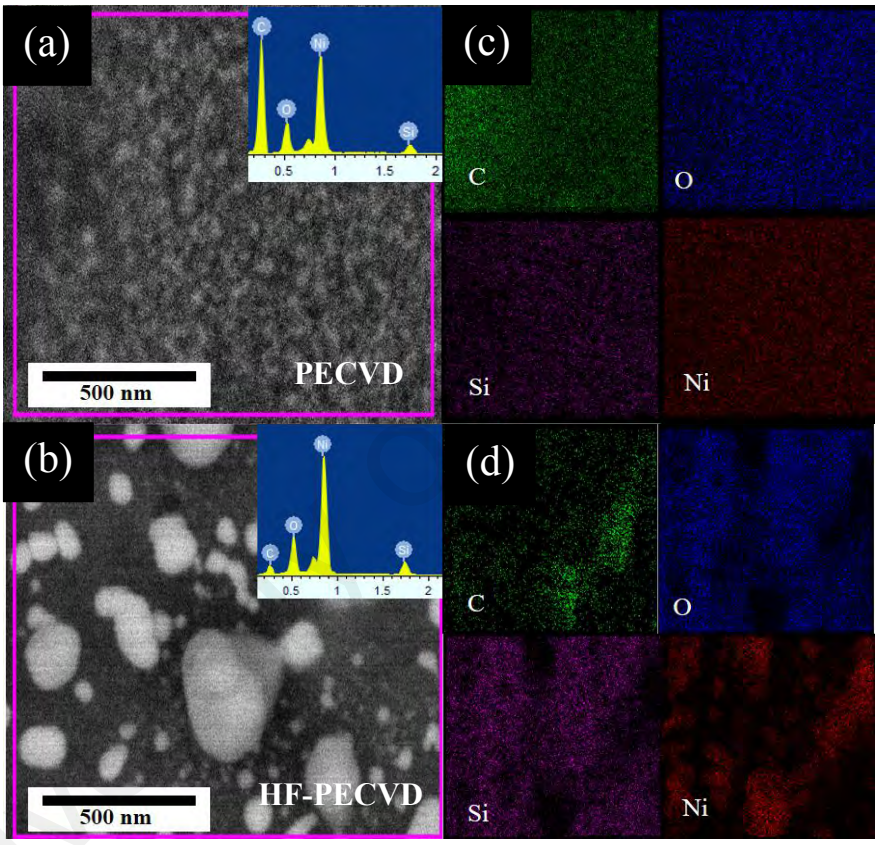


**Figure 5.3: FESEM images and, EDX analysis and mapping of Ni/graphene/$SiO_2$ substrate deposited using (a) PECVD and (b) HF-PECVD.**

### 5.2.2 Elemental Depth Profile of PECVD and HF-PECVD Ni/Graphene/$SiO_2$ Substrate

The XPS was used to study the depth profile of these films as shown in Figure 5.4. The curvature of the concentration depth profiles indicates the formation of the films growth and the presence of the C diffusion process. In addition, the concentration of the

diffused C is dependent on the formation of the Ni. For film deposited from PECVD, the region that each layer of the film was distinct. In particular, the C and Ni within the Ni catalyst layer was found to be consistent and thus indicates that the diffusion of C through the Ni layer was high and uniform across the catalyst. The consistency of the diffused C was due to the compactness and uniform thickness of Ni films formation. The high diffusivity of C into the Ni film resulted in thick graphene.

The concentration profile of C saturates at a depth of 5 nm for the film deposited from HF-PECVD. This indicates that the diffused C under the thickness of Ni layer was less than approximately 5 nm. The depth profile demonstrates that the atomic concentration of the diffused C through the Ni grains for HF-PECVD graphene was smaller than PECVD graphene. Furthermore, the shape of the Ni concentration profile curve was similar to the morphology of the sample displayed in FESEM images as illustrated in Figure 5.4(d) and (e) for both deposition technique. Moreover, the atomic concentration of C reduced as the atomic concentration of Ni was higher. This result suggests that the C atoms is not concentrated within Ni grain due to the presence of large grains boundaries and the deformed shape of the grain. It was evident that the C atoms were preferred to diffuse into the film along the grains boundaries or saturates to cover the surface of the Ni layer.

The results revealed that there were differences in the oxide layer for both film. For the PECVD graphene grown film, the oxide was clearly concentrated on the surface of the Ni catalyst and the $SiO_2$ substrate. A small percentage within the Ni layer suggests formation of contaminant or Ni-O bonding. On the other hand, the profile anomaly for the profile HF-PECVD grown film indicates high oxygen throughout the layers. Nevertheless, the corresponding detection of high Si concentration suggests that signal originated from the substrate, might be due to the penetration of Ni onto $SiO_2$ substrate surface during the annealing with the progress of the agglomeration of Ni films.

University of Malaya

Nevertheless, this also could be due to the irregularity in shape and large grains boundaries that allow small penetration of incident beams towards substrate throughout the measurement.

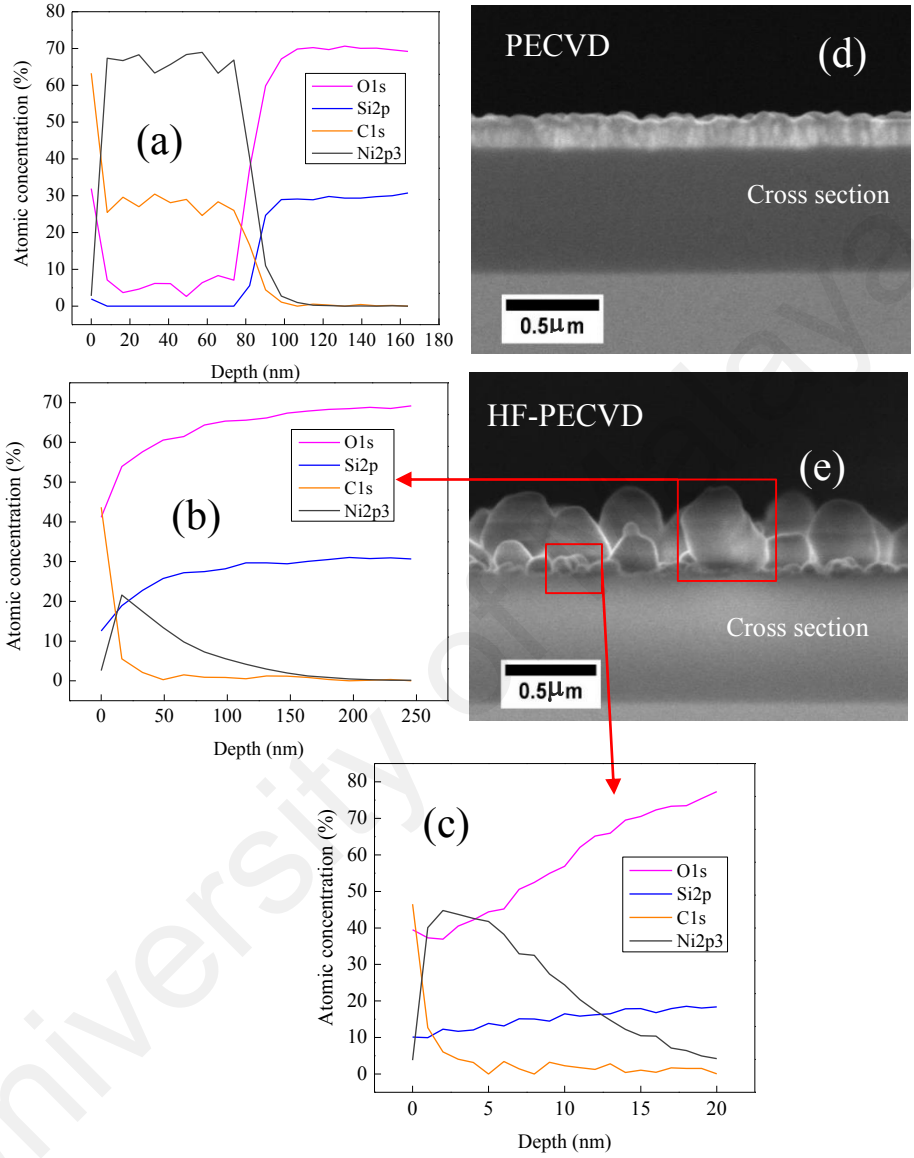


**Figure 5.4: The XPS depth profile of sample deposited from (a) PECVD and, (b) and (c) HF-PECVD. The FESEM images of cross-sectional (a) PECVD and (b) HF-PECVD samples.**

### 5.2.3 XRD Diffraction Pattern of PECVD and HF-PECVD Graphene/Ni Films

The XRD scans of the graphene grown on Ni films from PECVD and HF-PECVD without Ni etching are illustrated in Figure 5.5. For sample grown from PECVD, the

pattern demonstrates the presence of diffraction peak at $2\theta$ of approximately 43.9° and 64.1°, which are corresponding to Ni oriented at 111 plane and NiO oriented at 220 plane, respectively. The Ni peak suggests O contamination of the catalyst, which remarkably disappeared for films grown using HF-PECVD. This may be due to thermal annealing effects of the heat radiation from the hot wire. The finding supports assumption made in previous XPS analysis and demonstrates that there were no O bonded to Ni for the HF-PECVD grown film.

For the film grown from HF-PECVD, the XRD pattern demonstrates Ni crystalline peak at $2\theta$ of approximately 44.2°, 51.6° and 75.9°, which corresponded to the orientation of 111, 200 and 220 planes, respectively. The additional diffraction peak suggests that there was an increase in the structural orientation plane. This could be due to the increase in the grains within the films after the heat treatment from the HF, which changed the Ni morphological and structural orientation.

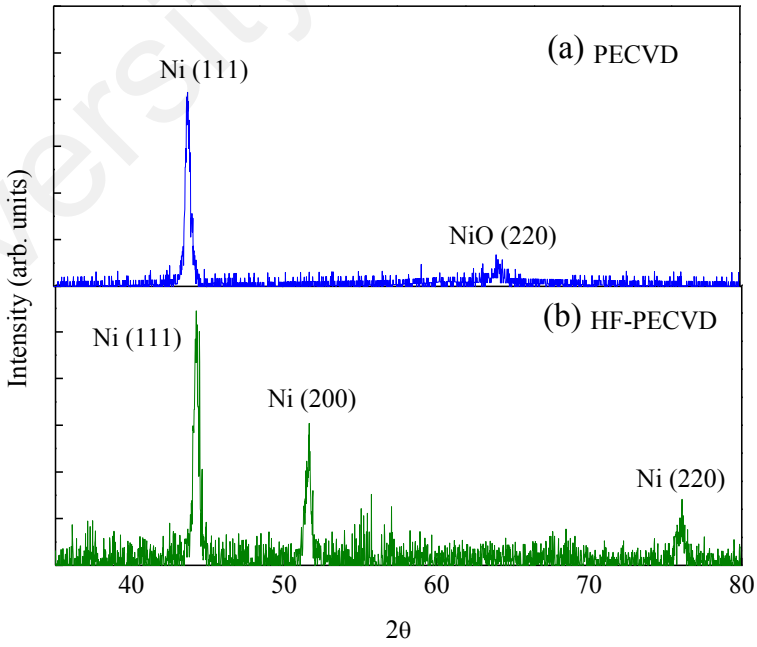


**Figure 5.5: XRD pattern of the graphene grown on Ni films using (a) HF-PECVD and (b) PECVD.**

University of Malaya

### 5.2.4 Structural Properties of PECVD and HF-PECVD Transfer-Free Graphene after Ni Etching

The characteristics and properties of the graphene were then investigated once the Ni layers were etched using wet etching process. The structural properties of the films were studied using Raman scattering. Figure 5.6 demonstrates that the Raman spectra of graphene films grown from PECVD and HF-PECVD. A total of four prominent bands assigned to D, G, 2D, and D'+G' with peaks positioned at 1350 $cm^{-1}$, 1580 $cm^{-1}$, 2700 $cm^{-1}$ and 2900 $cm^{-1}$, respectively were observed for graphene grown from PECVD. Nevertheless, only the D, G and 2D band were found in the spectra for film grown from HF-PECVD. Moreover, the peak corresponded to D'+G' was almost negligible.

The D'+G' band indicates defect activated process similar to the D band, which both bands are elastic scattering of phonon caused by defects. This provided momentum conservation in Raman-process. The absence of the D'+G' band demonstrates an improvement in the structure ordering of the graphene grown from HF-PECVD. This is in agreement with the corresponding decreased in $I_D/I_G$ ratio and FWHM G of the films as listed in Table 5.1. Furthermore, reduction in both $I_D/I_G$ ratio and FWHM G indicates the growth of well-ordered graphitic structured graphene, which attributed to the decrease in the films defects. On the other hand, the reduction in the 2D peak intensity for graphene grown from PECVD is attributed to the increase in number of graphene layers. Consequently, this caused an effective increase in the intensity of the defects peaks as detected by Raman. The defects have shown to cause the deformation of the band structure and breakdown in the second-order spectrum of the graphene (Eastman et al., 2014; Ferrari et al., 2006).

University of Malaya

Thus, the use of HF-PECVD is superior as it produces graphene layers with lower defects and lower number of layers as compared PECVD.

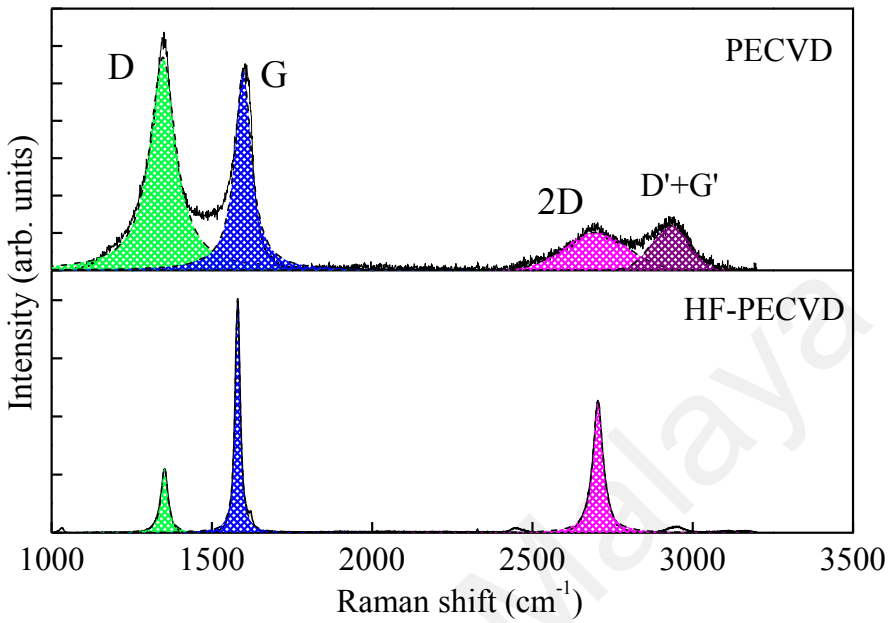


**Figure 5.6: Raman spectra of graphene deposited from HF-PECVD and PECVD.**

**Table 5.1: Peak position and FWHM of D, G, 2D and D'+G' band, and $I_D/I_G$ and $I_{2D}/I_G$.**

| Deposition technique | Raman peak | Peak position | FWHM | $I_D/I_G$ | $I_{2D}/I_G$ |
|---|---|---|---|---|---|
| **PECVD** | D | 1347 | 98 | 1.63 | 0.19 |
| | G | 1597 | 62 | | |
| | 2D | 2697 | 233 | | |
| | D'+G' | 2931 | 141 | | |
| **HF-PECVD** | D | 1352 | 24.9 | 0.35 | 0.56 |
| | G | 1580 | 18.5 | | |
| | 2D | 2704 | 37 | | |

### 5.2.5 Morphological Properties of PECVD and HF-PECVD Transfer-Free Graphene after Ni Etching

The morphology of the transfer-free graphene after Ni etching were analyzed using HRTEM images as shown in Figure 5.7. The images demonstrate the growth of large area graphene produced from both PECVD and HF-PECVD techniques. Nevertheless, both

University of Malaya

films had differences in their formations, where HF-PECVD produced more uniform graphene compared to PECVD graphene film. The non-uniform PECVD graphene film was constructed using the stacking of graphene patches, which resulted in highly wrinkles graphene film. In contrast, graphene formed from HF-PECVD demonstrates the stacking of uniform graphene layers that appeared to be wrinkle-free.

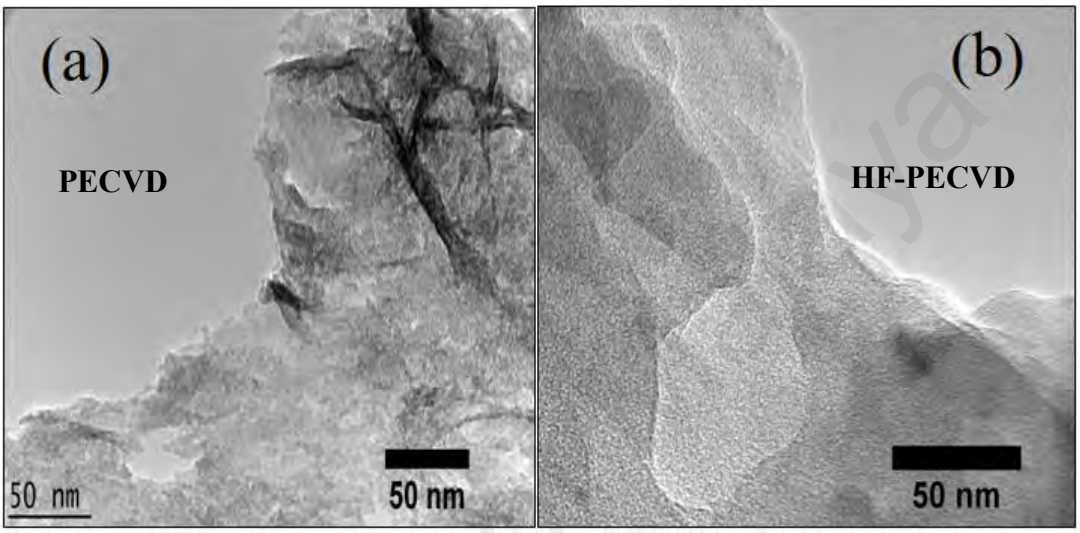


**Figure 5.7: HRTEM images of graphene film deposited from (a) PECVD and (b) HF-PECVD.**

### 5.2.6 The Influence of Thermal Heating on the Growth of Transfer-Free Graphene

This section elucidates the influence of radiant heat transfer on the Ni grains size and grains boundaries towards the growth of transfer-free graphene using PECVD and HF-PECVD techniques. Figure 5.8 illustrates both growth models, where the comparison between the graphene growth using both method are demonstrated. It should be noted that the decomposition reaction was identical for PECVD and HF-PECVD. The effects of the thermal heating produced by the filament on the decomposition of $CH_4$ was insufficient to participate in the gas phase reaction since the filament temperature was too low. Evidence has shown that the temperature should be above 1900 °C for the filament temperature to influence the gas phase reaction (Shimabukuro et al., 2008).

In general, for both PECVD and HF-PECVD graphene growth, high-energy carbon radicals generated in the plasma were accelerated towards the Ni surface and penetrated through the Ni film surface. As a result, the density of dissolved carbon inside the Ni was higher compared to the Ni surface. This led to selective growth at the interface between Ni and $SiO_2$/Si substrate (Li et al., 2016). Nevertheless, the diffusion of these carbons through Ni is usually related to the size of grains and grains boundaries of the Ni films.

The PECVD technique was validated using FESEM and AFM analysis, where the nano-ordered Ni structured film surface indicates the formation of small Ni grains boundaries. Due to these small boundaries, the density of dissolved C inside Ni film was higher than that at the surfaces. Nevertheless, C favoured the area with higher surface energy such as grain boundaries due to the presence of more atomic dangling bonds at these areas that could easily attract carbon atoms. Since these grains boundaries are densely packed, the C atoms tends to congregate or form the edges of the layers along these boundaries when graphene layers are formed between the interfaces of the Ni/$SiO_2$ interface. This led to the formation of wrinkles in the graphene layer after Ni etching as shown in the previous HRTEM image. These wrinkles formations that originated from the graphene patches made the film highly defective as defects usually formed at the graphene edges (Allen et al., 2009; Mattevi et al., 2011).

The growth of well-ordered and less defective graphene were produced when additional heating was applied by the hot filament in the HF-PECVD system. From the AFM and FESEM analysis, the transformation of nano-sized Ni film to the micro-sized island-shaped Ni was correlated with the agglomeration effects of the thin Ni films at high temperature. Furthermore, the XPS result imparted further information, where the increase in temperature caused the reconstructed structure of the films. These micro-sized Ni islands, which corresponds to the increased in the size of Ni boundaries provided large

University of Malaya

surface areas and larger path lengths for lattice diffusion of C atoms. Consequently, this resulted in uniform stacking of graphene layers at the Ni/$SiO_2$ interface (Balluffi et al., 1975). This is due to the selective growth of graphene around the Ni islands and the lower face adjacent of the Ni due to the higher surface energy around these areas. This uniform stacking of C atoms on larger surface area for graphene nucleation resulted in the formation of graphene with lower defect density. In addition, the defects in the graphene sheet can be annealed at higher temperature, which resulted in a thermally activated healing process (Liu et al., 2015). This led to the modification process of defective site, which attributes to the defect healing. Thereupon, the nickel-carbon chemical bonds kept broken and reformed around defected carbon zones at high temperature. This provides a direct interaction needed for the healing.

University of Malaya

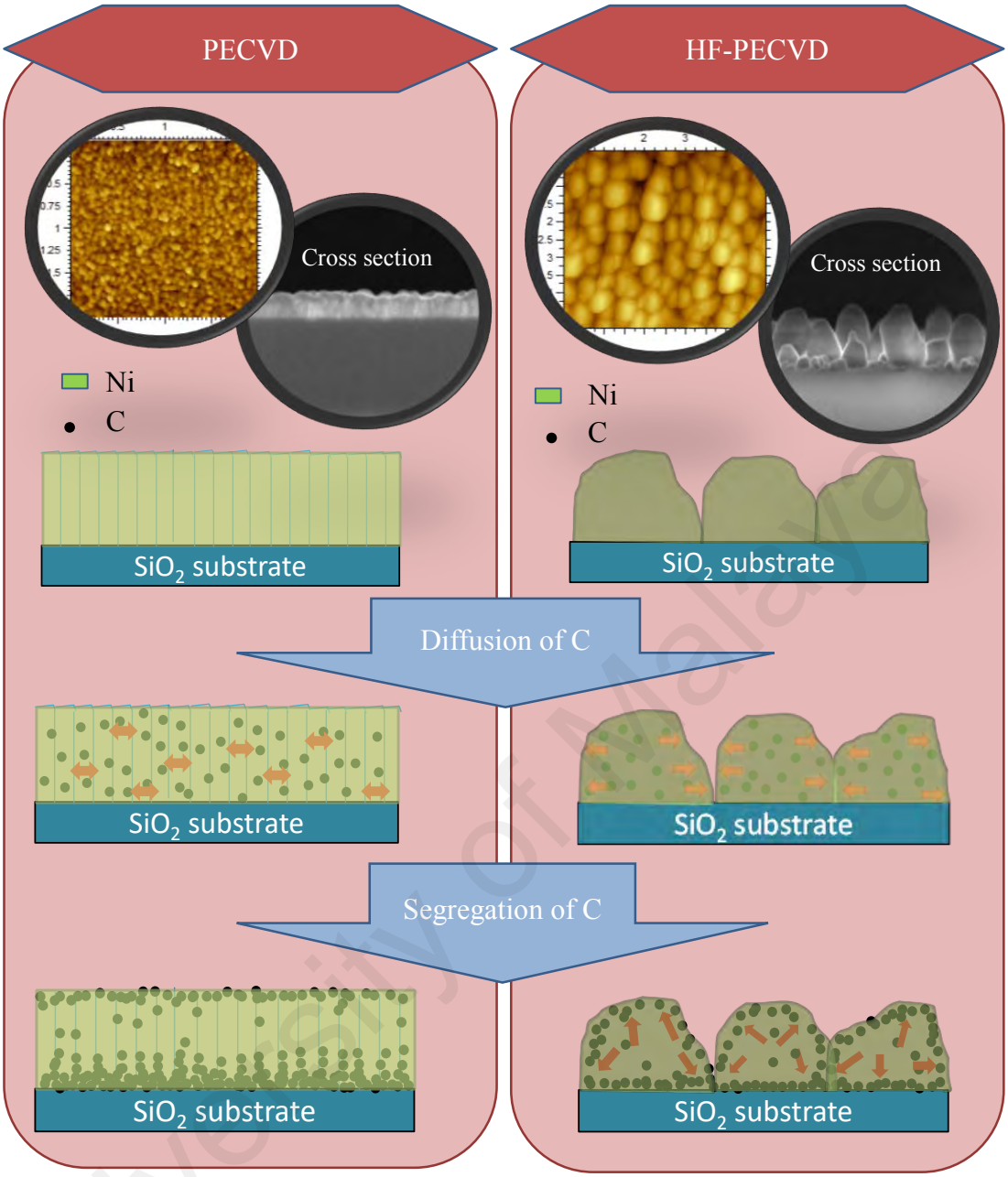


**Figure 5.8: Schematic illustration of the growth model of PECVD and HF-PECVD graphene.**

University of Malaya

## 5.3 Effects of Deposition Time on the Structure, Morphology, Chemical Bonding of HF-PECVD Transfer-Free Graphene

The result in the previous section implies that HF-PECVD technique has shown to be a reliable method in producing good quality transfer-free graphene compared to PECVD technique at low deposition temperature. As such, HF-PECVD technique achieved an improvement in the structural and morphological properties of the grown graphene. Various deposition time (1, 2, 3, 4, and 5 minutes) were applied to extend the study of graphene grown HF-PECVD. As such, the progression of the critical aspects for ideal graphene layer formation such as the number of layers, uniformity and defect density of the growing graphene films were monitored.

### 5.3.1 Structural Properties of the HF-PECVD Transfer-Free Graphene

The Raman spectra of transfer-free graphene layer grown on the substrate at different deposition time are illustrated in Figure 5.9. Three graphene characteristic peaks were observed at approximately 1350 $cm^{-1}$, 1580 $cm^{-1}$ and 2700 $cm^{-1}$ corresponding to the D, G and 2D peak, respectively. This result indicates that graphene could be produced at shorter deposition time (e.g., 1 minute).

The variation in $I_{2D}/I_G$ ratios as a function of deposition time is shown in Figure 5.10. The $I_{2D}/I_G$ and corresponding the relative 2D peak intensity decreased as the deposition time increased. In general, the 2D peak was generated by second-order zone-boundary phonon scattering, where it was sensitive to the c-axis stacking of graphene layer (Ferrari, 2007). The 2D bands were formed using the same phonon that were scattered twice (forward or backward scattering) to provide momentum conservation. The increase in the number of layer will have a great influence on the possible transition due to the amount of interacting layers. As a results, the Raman signal intensity was shielded. Thus, the

University of Malaya

decrease in $I_{2D}/I_G$ ratio demonstrates that the number of graphene layers were increased almost linearly with deposition time.

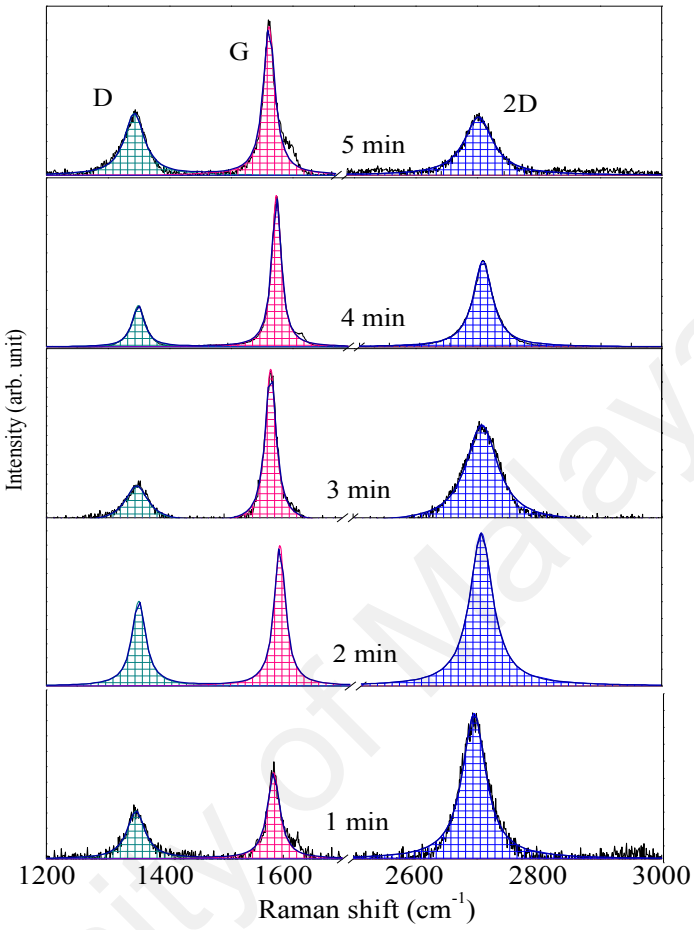


**Figure 5.9: Raman spectra of graphene films as a function of deposition time.**

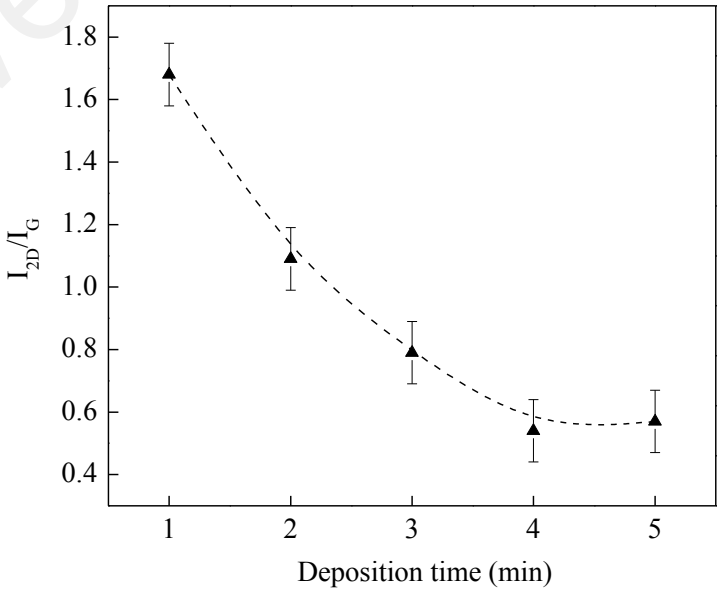


**Figure 5.10: $I_{2D}/I_G$ ratio of graphene as a function of deposition time.**

University of Malaya

The FWHM of the 2D band is an important factor for investigating the thickness of graphene layer. The FWHM 2D indicates the split width of the energy band due to the number of graphene layers, which influenced the interlayer distance of the phonon scattering. The variation in the FWHM 2D of the graphene films as a function of deposition time is shown in Figure 5.11. As the deposition time was increased, the FWHM 2D band increased. In addition, if the interlayer distance decreases, the split width of the energy band becomes larger. This results in an increase in the 2D band line-width for larger number of graphene layer (Ferrari et al., 2006; Herziger, 2015; Malard et al., 2009a; Venezuela et al., 2011).

The deposition time increased the 2D peak position redshift to higher frequency with the increasing number of layers as shown in Figure 5.11. The 2D peak frequency shift may be caused by the interaction between $SiO_2$ substrate and the bottom layer of graphene. Based on the double resonance theory (Herziger, 2015; Venezuela et al., 2011), this interaction is considered as an environmental effect. Therefore, it caused the red shift in the average 2D band peak frequency to be observed when the number of graphene layers increased.

University of Malaya

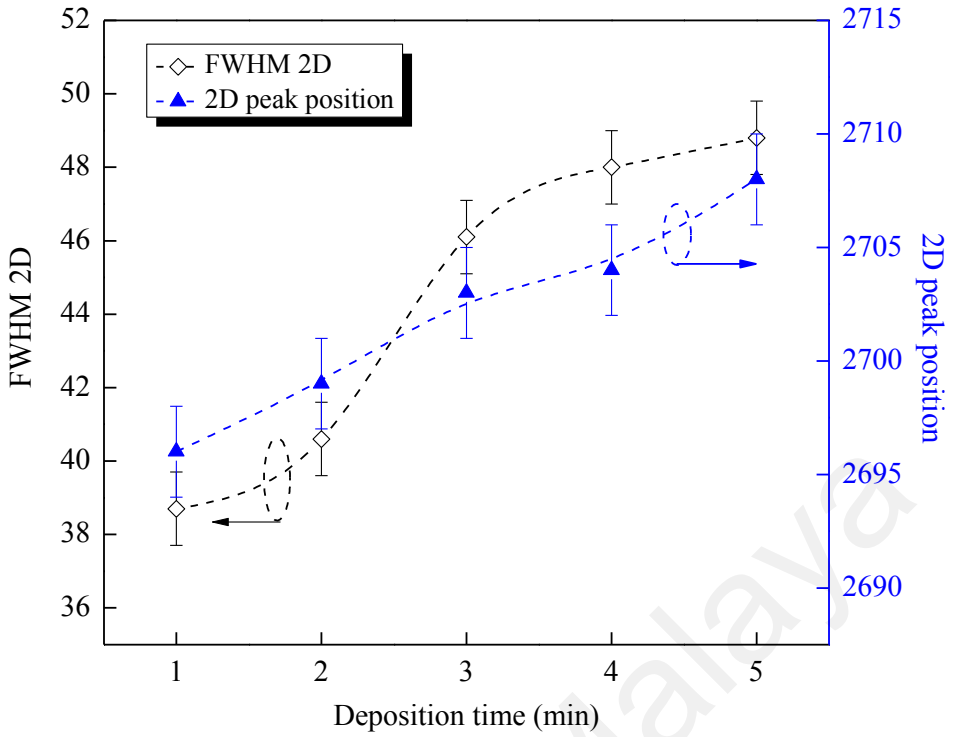


**Figure 5.11: The variation of FWHM 2D of graphene films as a function of deposition time.**

### 5.3.2 Morphological Properties of HF-PECVD Transfer-Free Graphene

The thickness and number of graphene layers were analyzed based on the HRTEM images. Figure 5.12 illustrates the HRTEM images of graphene after the graphene sheets were transferred onto Cu TEM grid. The grey and white fringes at the films edges represent different layers, where the number of graphene layers for each sample were approximated directly from the fringes. The results indicate that the variation in the growth time produced bilayer, trilayer and multilayer graphene. The number of layers was proportional to the deposition time. In addition, shorter deposition time limited the diffusion of C through the Ni layer, where it could be used to control the number of layer and the uniformity of the graphene.

The results of this study were consistent with the previous Raman results. Moreover, the further increase in the deposition time increased the number of graphene layers. Nevertheless, as the growth time increased, the average intensity of the D peak slightly

University of Malaya

decreased as shown in Figure 5.12(f). This result indicates that more complete growth of graphene was formed at higher growth rate from the stacking graphene. Similarly, Liu et al. suggested that in the single layer graphene, vacancy defects favored to coalesce into larger vacancy holes. On the other hand, in multi-layer graphene, the vacancies tend to concentrate in a single hole in one of its layer through both intra- and inter-layer migrations as illustrated in Figure 5.13. The vacancy inter-layer migration is facilitated by the interaction of defects in the neighboring layers (Liu, 2014). Thus, this might not reflect that the number of defects in lower number of layered graphene was higher than the multilayered graphene, instead, the defects in the former was more significant in terms of defects-layer ratio.

University of Malaya

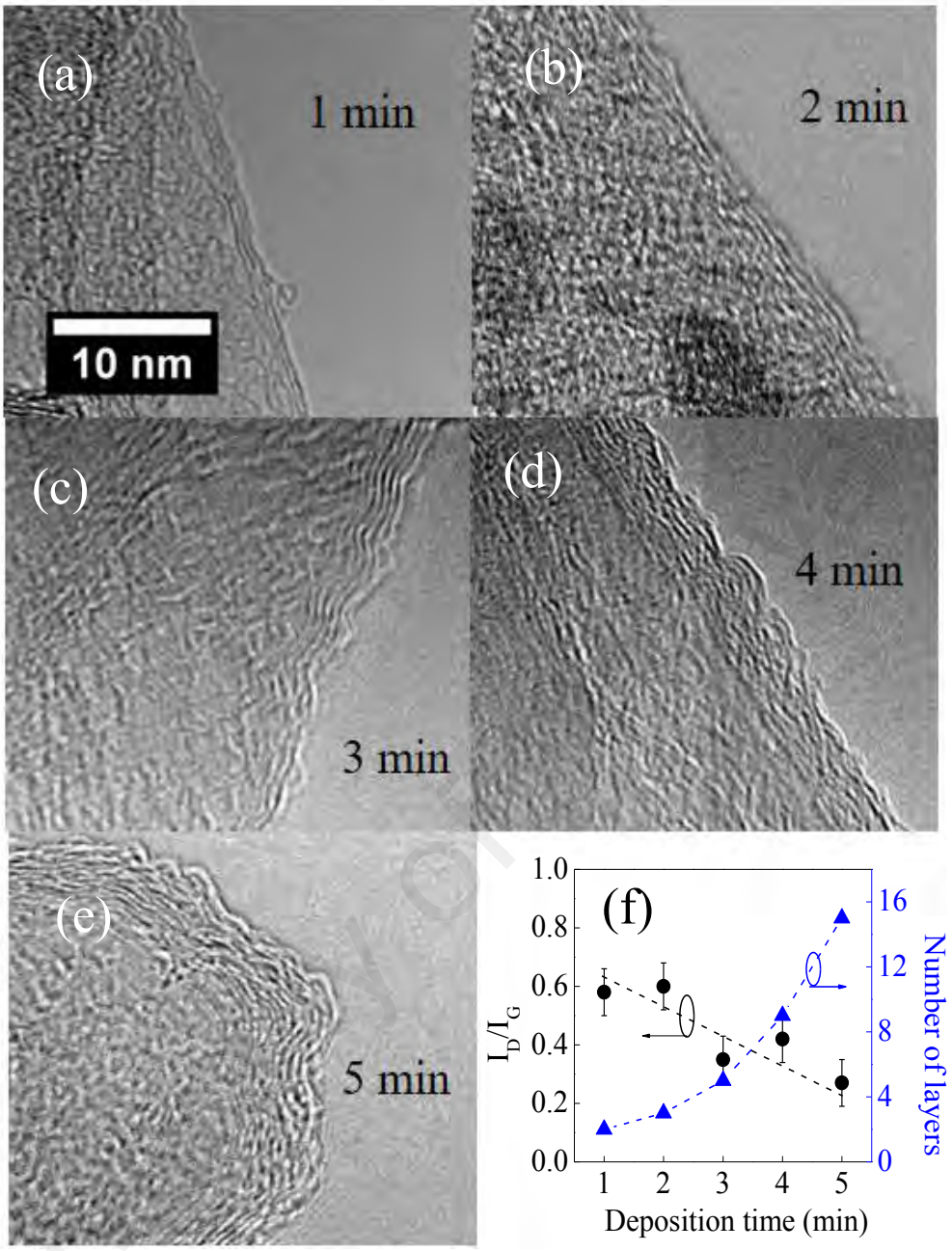


**Figure 5.12: High-resolution TEM images of graphene grown at (a) 1 minute, (b) 2 minutes, (c) 3 minutes, (d) 4 minutes, (e) 5 minutes and (f) variation of $I_D/I_G$ ratio of graphene films as a of deposition time.**

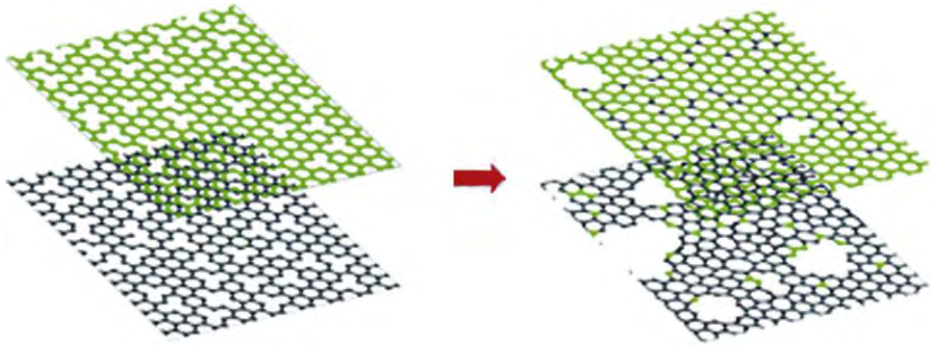

**Figure 5.13: A diagram of vacancy migration between graphene layers and the self-healing of other layers (Liu et al., 2015).**

### 5.3.3 Chemical Bonding of HF-PECVD Transfer-Free Graphene Films

The XPS was used to validate the Raman finding, where chemical composition of the graphene could be determined. Figure 5.14 demonstrates a wide range XPS spectra in the binding energy ranging from 0 to 1200 eV of the graphene films as a function of deposition time. From the XPS spectra, the main chemical components were identified as C 1s, O 1s, Si 2s and Si 2p. By excluding the Si peak that originates from the substrate, the constituents of these films were C and O. In addition, the absence of Ni peak in the spectra for all films demonstrated that the catalyst was successfully etched away using the wet etching technique.

The C1s high-resolution XPS scans for these graphene films are shown in Figure 5.15. The C1s spectra were explicitly deconvoluted into five components corresponding to C $sp^2$, C-OH, C-O, C=O, and C-C=O with respective binding energies of 284.6 eV, 285.7 eV, 286.6 eV, 287.5 eV and 288.7 eV. The Shirley's background subtraction was carried out prior to deconvolution. Moreover, the background spectra deformation was due to inelastic scattering event that photoelectron underwent as they were transported from the point of excitation to the samples surface. As a consequence, this resulted in the inelastic background intensity. The oxygen-related components of the deconvoluted peak indicates a certain degree of oxidization, which is most likely originated from residual oxygen in

University of Malaya

the low-vacuum closed chamber. The primary peak corresponding to $sp^2$ C-C network that appeared at 283.8 eV to 284 eV progressively shifted to higher binding energy as the growth time was reduced. This blue shift in the binding energy indicates an increased in graphitic nature of the film (284.4 eV) that detected the formation of $sp^2$ C–C network of the grown film as growth time decreases.

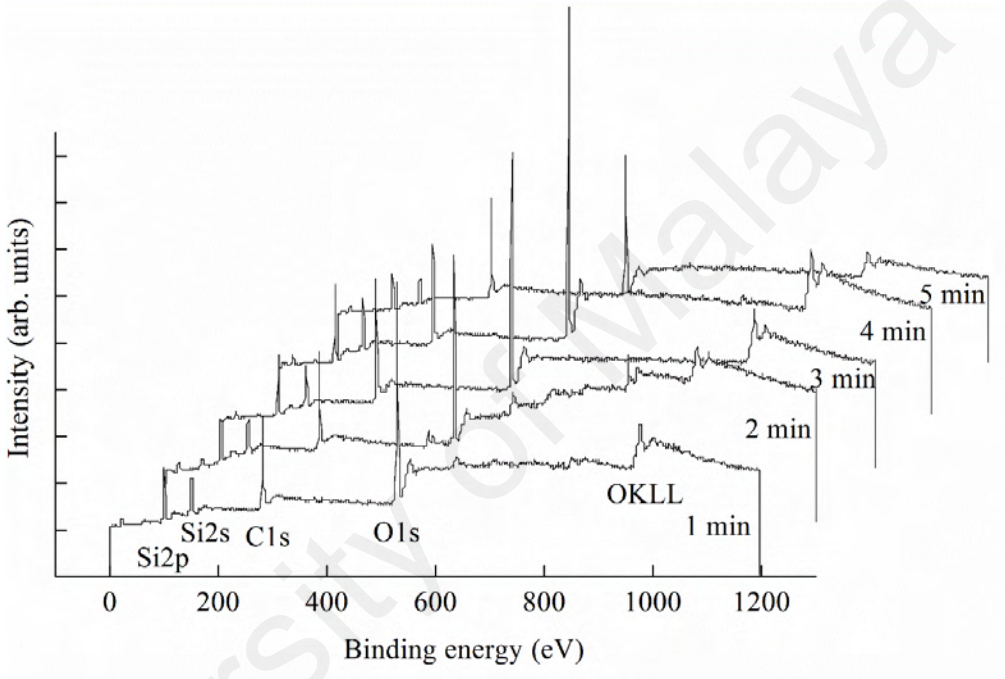


**Figure 5.14: General scan for the graphene grown on $SiO_2$ substrate at different deposition time.**

University of Malaya

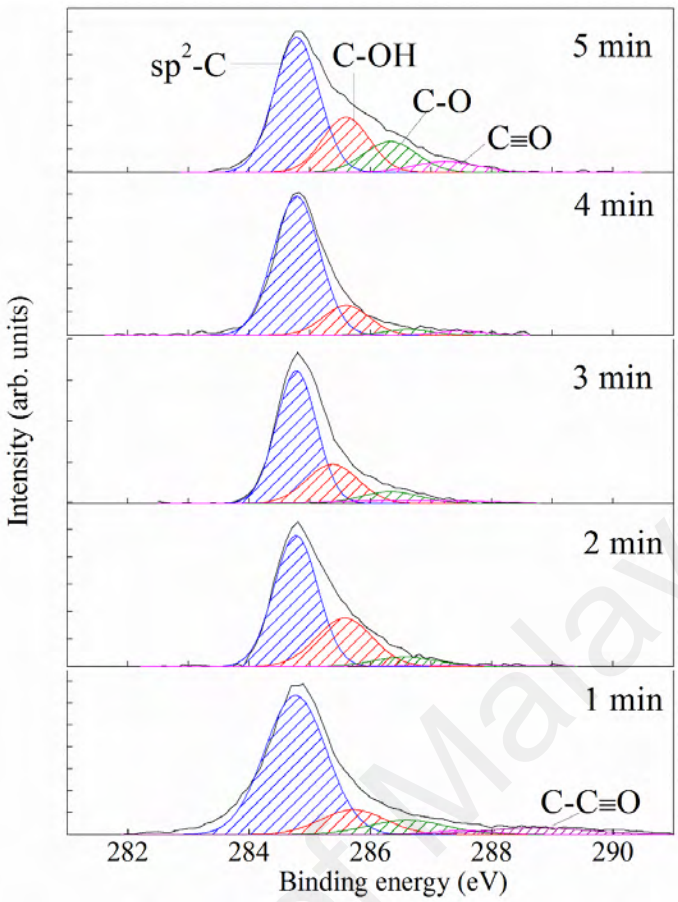


**Figure 5.15: High-resolution XPS scan for C 1s core level peak of transfer-free graphene.**

Figure 5.16 demonstrates the variation of $sp^2$-C to C-O bonds ratio and percentage of C bonded with O component. The $sp^2$-C content decreased as the deposition time increased, while the percentage of C bonded to O components increased as the deposition time increased. It is well-known that defects associated with dangling bonds should enhance the reactivity of graphene. Numerous simulations suggested that hydroxyl, carboxyl, or other groups could be easily attracted to vacancy-type defects (Herziger, 2015; Malard et al., 2009b). These simulations also suggested that the increase in carbon bonded to oxygen content would follow the decrease in the content of the ordered ring structures or an increase in defective rings, permitting the bonding of oxygen to these C or defects sites. Nonetheless, it should be noted that the previous Raman result demonstrated the opposite trend, whereby $I_D/I_G$ decreased with an increase in the deposition time. The decreased $I_D/I_G$ indicates the decrease in defects in the rings

University of Malaya

structure, which is contradictory to the decrease in an ordered ring structures. An increase in the area of the edges due to higher number of graphene layers and corresponding increase in dangling bonds formed along this edges allowed O to be easily bonded as post-deposition contaminant. Thus, the two contradicting ratios in both XPS and Raman results generated distinct interpretation of the graphene defects could be clearly resolved.

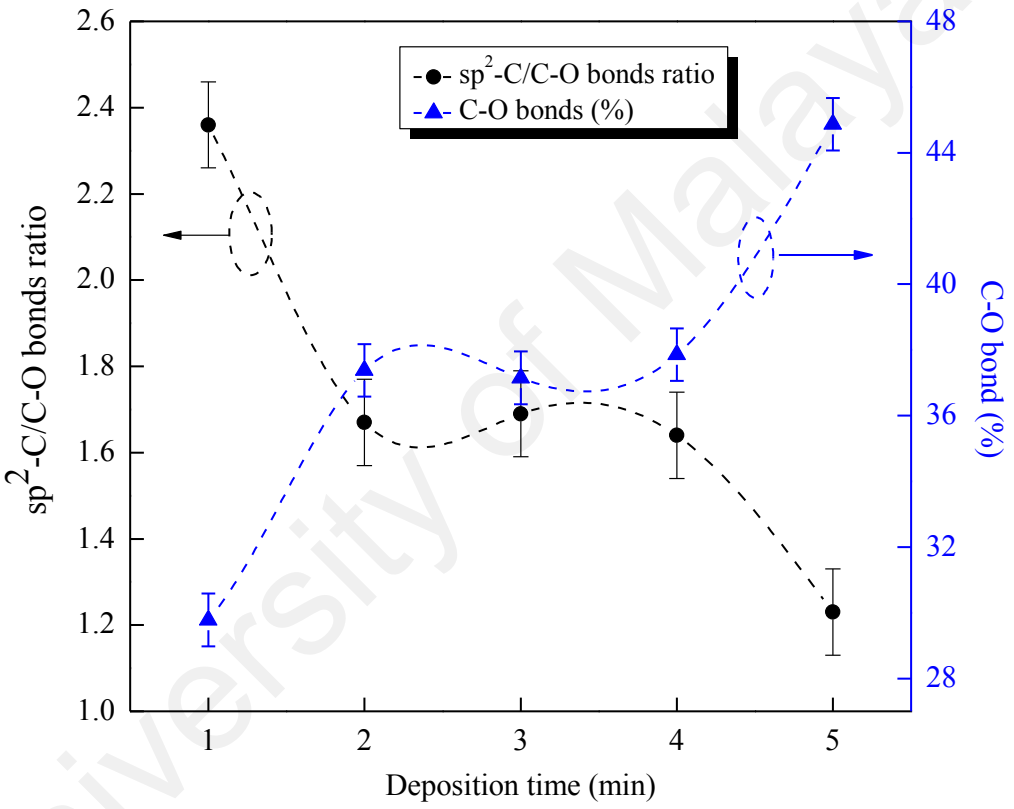


**Figure 5.16: Variation of $sp^2$-C to C-O bonds ratio and percentage of C bonded with O content in the graphene films at different time.**

### 5.3.4 Uniformity of HF-PECVD Transfer-Free Graphene Growth

The sample deposited at 1min was used for the Raman mapping analysis. The sample exhibited the lowest number of graphene layers with lowest defects. The Raman mapping image is shown in Figure 5.17. The variation in color codings represent different film thickness that corresponded the different number of graphene layers.

University of Malaya

The Raman shift for the selected spots highlighted as I, II and III in the image were included in the Figure 5.17 (I-III). The respective $I_{2D}/I_G$ ratio and FWHM values of these spots were as follows: spot (I) 0.6; 55 $cm^{-1}$; spot (II) 0.9; 49 $cm^{-1}$ and spot (III) 1.7; 45 $cm^{-1}$. The spots at I, II and III represent multi-layered (yellow), tri-layered (red) and bi-layered (green) graphene, respectively (Malard et al., 2009a). This results indicate that the graphene film formed mainly consists of tri-layered graphene with patches of bi-layered or multilayered regions. Thus, it is consistent with the previous Raman and HRTEM results. Furthermore, the FWHM values are confined within a narrow range from 45 $cm^{-1}$ to 55 $cm^{-1}$. There were no significant differences between both low defect density and uniform defects distribution throughout the film.

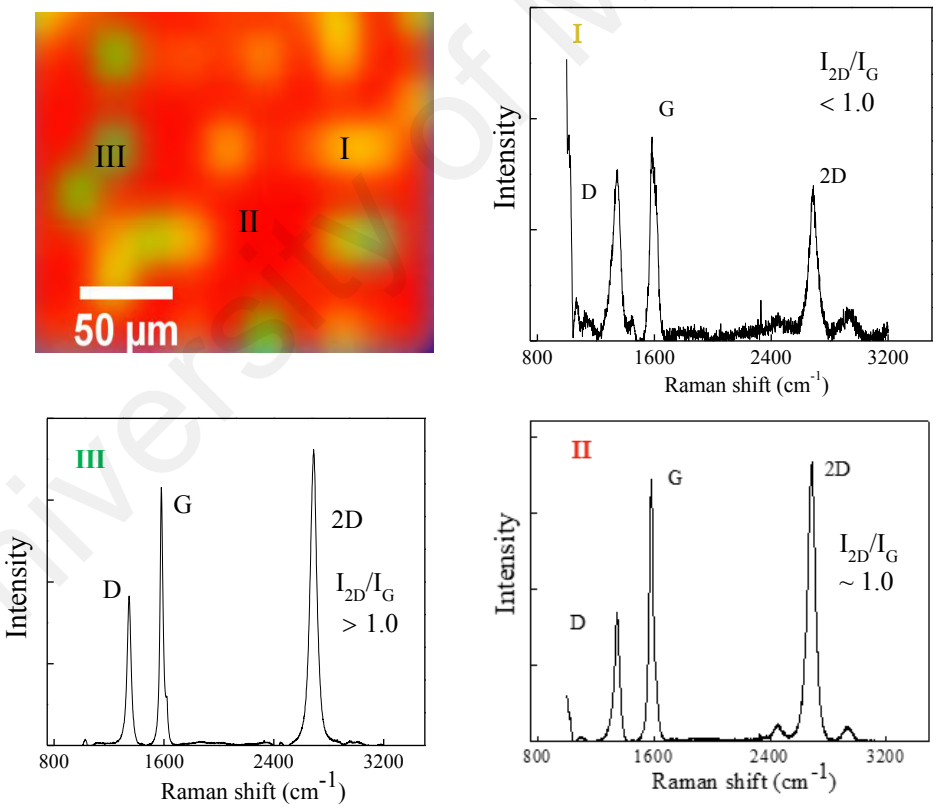


**Figure 5.17: The Raman mapping of graphene film deposited at deposition time of 1 min.**

University of Malaya

## 5.4 Effects of Substrate Temperature on the Structure, Morphology, Chemical Bonding of HF-PECVD Transfer-Free Graphene

A previous study has shown that the variation in deposition time could be used to control the number of graphene layer and their structural properties. Moreover, limiting the deposition time decreased the deposition rate and reduced the number of layers. The deposition time was fixed at 1 minute for the HF-PECVD technique, as this was determined as the best condition. In the previous sections, the deposition temperature was maintained at 400°C, while for this investigation the temperature points were varied in decreasing pattern, which were ranging from 400 °C to 100 °C. The aim of this section is to determine a balance or compromise between the quality of the graphene film and the low deposition temperature limit. Furthermore, the properties of these films in regard to the changes in substrate temperature affected the wettability and magnetic properties of the films.

### 5.4.1 Structural Properties of HF-PECVD Transfer-Free Graphene

The Raman spectra of graphene grown on $SiO_2$ substrates as a function of substrate temperature is shown in Figure 5.18. Three prominent peaks located at approximately 1350 $cm^{-1}$, 1580 $cm^{-1}$ and 2700 $cm^{-1}$ assigned to D, G and 2D band, respectively, were clearly observed for all samples. In addition, samples deposited below $T_S$ of 400 °C a D'+G' band located at 2900 $cm^{-1}$ appeared, while the intensity of D peak appeared to increase as $T_S$ decreased. The variation in D'+G' and the D peak intensity indicates that as $T_S$ decreased the defects in the corresponding film increased leading to lower quality graphene film.

University of Malaya

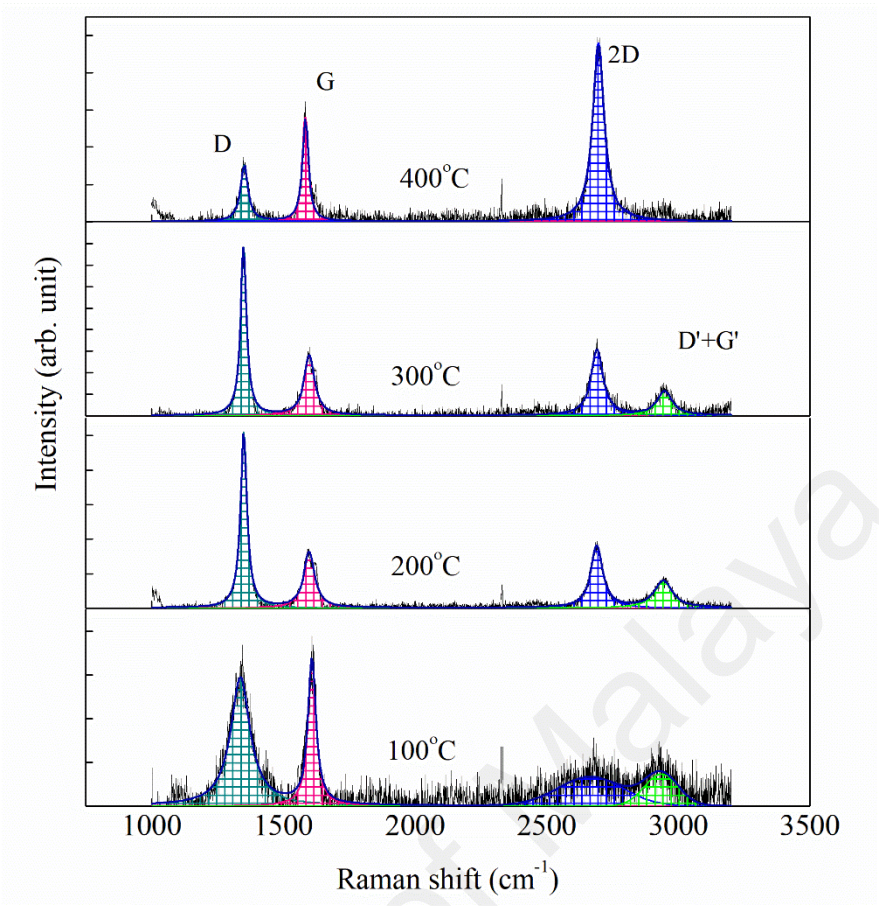


**Figure 5.18: The Raman spectra of graphene film as a function of substrate temperature.**

The intensity ratio of relevant peaks namely the $I_D/I_G$ and $I_{2D}/I_G$ was analyzed. The variation in $I_D/I_G$ ratio as a function of $T_S$ is shown in Figure 5.19. In general, $I_D/I_G$ value provides the nature of ring structure and lattice distortion of the graphene film (Hsieh et al., 2009). The gradual increase in $I_D/I_G$ ratio with decrease in $T_S$ value indicates the decreasing size of in-plane $sp^2$ domain. This implies that the partial disordered structure in the films increases at lower temperature. Furthermore, less ordered graphene film with lower number of six-fold rings structures might be formed at film grown at $T_S$ lower than 400 °C as the impinging C atoms or ions in growing surface loss more energy (Liu et al., 2012) at the lower substrate temperature.

On the other hand, monotonic decrease in the $I_{2D}/I_G$ values with the decrease in $T_S$ indicates the increase in number of graphene layers. As such, graphene deposited at $T_S$ of

University of Malaya

400 °C exhibited the highest value of $I_{2D}/I_G$ of approximately 1.6, which is categorized as tri-layered graphene. As the $I_{2D}/I_G$ ratio becomes smaller than particular value, the film could be categorized as multilayered graphene (Gupta et al., 2006; Venezuela et al., 2011; Zhang et al., 2010). This result supports the fact that the graphene deposited at lower $T_S$ produced higher number of graphene layers, which is inconsistent with result of previous studies using common PECVD synthesis. As such, many studies indicated that the film thickness increased with the increase in temperature (Schauer, 2007; Shimabukuro et al., 2008). This contradicting result might be due to the variations in growth mechanisms, where the Ni buffer layers play important roles in this regard. The Ni surface can catalyze the dissociation of C-C bonds and promote its diffusion even at low deposition temperature (Du et al., 2005). The C atoms can be transported through the Ni layer primarily along the Ni grain boundaries towards the Ni-$SiO_2$ interface (Balluffi et al., 1975; Fisher, 1951), whereby the growth of graphene is related to the Ni grain size. In relation to this, the size of Ni grains is considered to be largest at $T_S$ of 400 °C, which increased the surface area for nucleation of graphene. This, in turn, produces well-ordered graphene structure with lower number of layers, and thus forms better quality graphene (Kwak et al., 2012).

It should be noted that the results in this section is different from the study on the effects of the deposition time with the increase in the number of graphene layers, where there was a reduction in the disorder of the overall films. Nonetheless, this could be explained by the reduction in the energy of the C active species on the surface of the growing films. Consequently, this would reduce the penetration depth of this species, which in the case of the deposition time benefits to remove the disorder and dangling bonds within the film.

University of Malaya

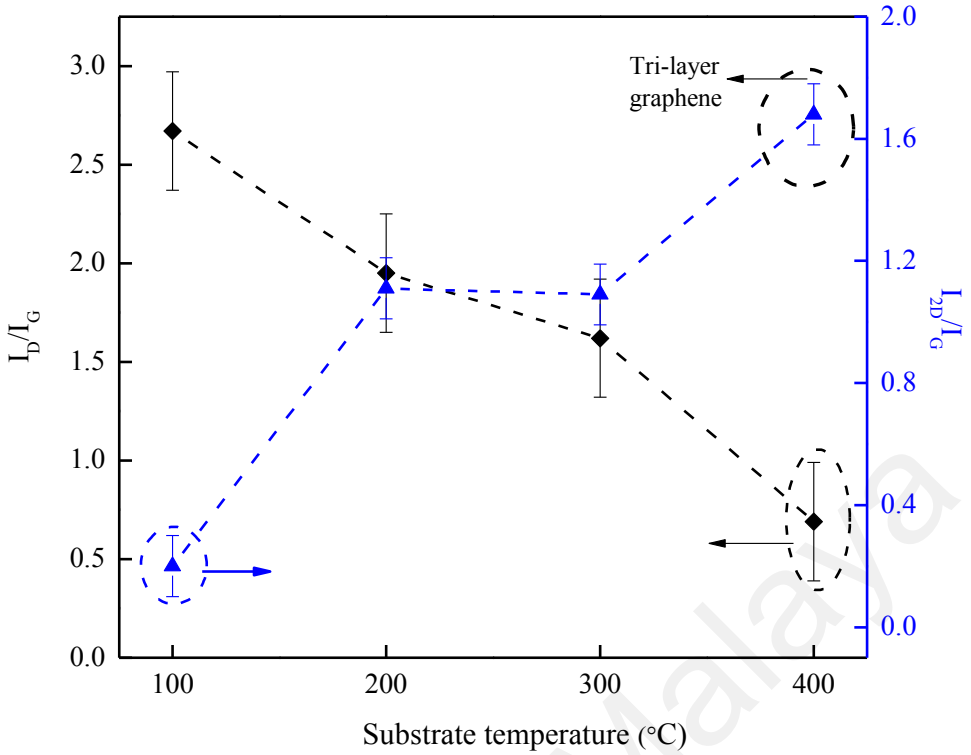


**Figure 5.19: Ratio intensity of D to G peak, and 2D to G peak of Raman spectra.**

### 5.4.2 Morphological Properties of HF-PECVD Transfer-Free Graphene

The HRTEM images of selected samples were captured to verify the number of graphene layers as predicted previously by the Raman result. Figure 5.20 illustrates HRTEM images of the graphene deposited at two different $T_S$, which were 400 °C and 200 °C. The graphene film deposited at $T_S$ of 200 °C was captured to represents the films grown at $T_S$ below than 400 °C. The high-magnification HRTEM images demonstrate clear illustration of the fringes along the films edges. These fringes represent the number of graphene layers. It is clearly visible that the graphene grown at $T_S$ of 400 °C were made up of tri-layered graphene, while the one deposited at $T_S$ 200 °C were made up of multi-layered graphene. This is in agreement with the Raman results and the predicted $I_{2D}/I_G$ value ranges. Moreover, the film deposited at $T_S$ 100 °C and 300 °C should also be made up of multilayered graphene.

University of Malaya

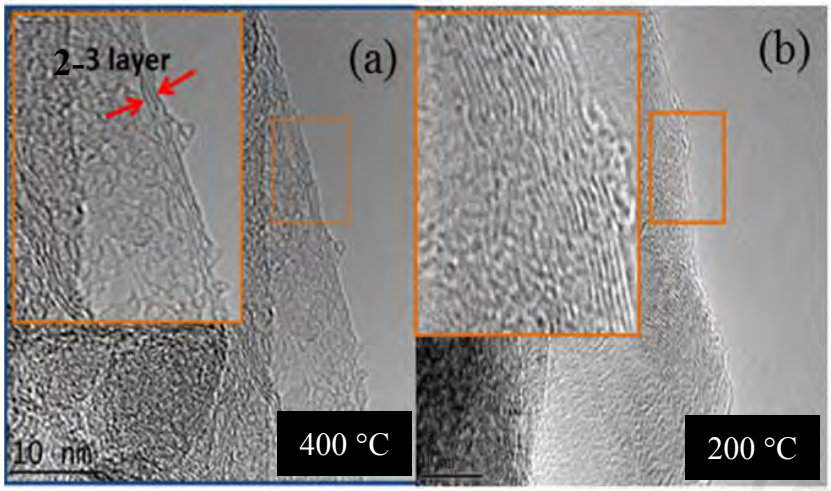


**Figure 5.20: HRTEM image of graphene at $T_S$ of (a) 400 °C and (b) 200 °C.**

### 5.4.3 Chemical Bonding of HF-PECVD Transfer-Free Graphene

The chemical compositions of the transfer-free graphene films deposited at various $T_S$ were analyzed using XPS. The XPS wide scan spectra for the deposited graphene films as a function of $T_S$ is shown in Figure 5.21. From the XPS scan, the absence of Ni peaks demonstrates that the catalyst was successfully removed. Consequently, this evidenced that the etching process of the Ni using HCl was executed well for all set of samples.

The C1s band of XPS spectra ranging from 282 eV to 288 eV as a function of $T_S$ is shown in Figure 5.22. The spectra consists of different overlapping of C bond centered at different binding energy and were deconvoluted using four Gaussian fitting curves on a Shirley background. These curves represent $sp^2$-C, C-OH, C-O and C≡O bond with binding energies centered at 284.6 eV, 285.7 eV, 286.6 eV and 287.5 eV, respectively (Castelaín et al., 2012; Shen et al., 2012; Wang et al., 2010). For all samples, the intensities of the $sp^2$-C bond had the dominant peak in their corresponding spectra. Furthermore, the $sp^2$-C bonding shifted to higher binding energy as $T_S$ was reduced. This indicates reduction in graphitic C=C bonding in the films (Paredes et al., 2009). This is supported by the value of the $sp^2$-C to C-O bonding ratio, where the ratios were calculated from the relative areas deduce from the curve fitting. In addition, the value of $sp^2$-C/C-O

University of Malaya

bond ratio decreased with the decrease in $T_S$ as presented in Figure 5.23. The decrease in the $sp^2$C/C-O bond ratio and energy shift in $sp^2$-C occurred due to the decrease in graphitic structure. This indicates that the $sp^2$ networks eventually become an unstable configuration as $T_S$ is decreased. Moreover, it is also anticipated that the hybridization of $sp^2$ network, which requires high energy is hindered by the insufficiency of the lower temperature as $T_S$ is decreased. This trend is in agreement with the corresponding increase in the $I_D/I_G$ ratio at lower $T_S$ in Raman analysis.

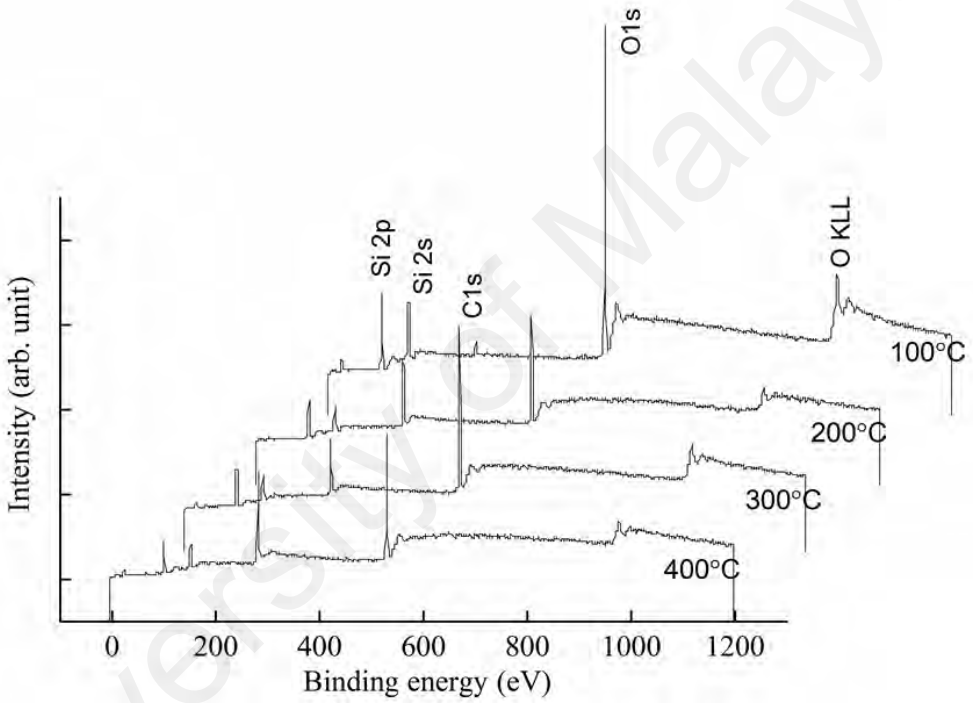


**Figure 5.21: General scan for the graphene grown on $SiO_2$ substrate at different substrate temperature.**

University of Malaya

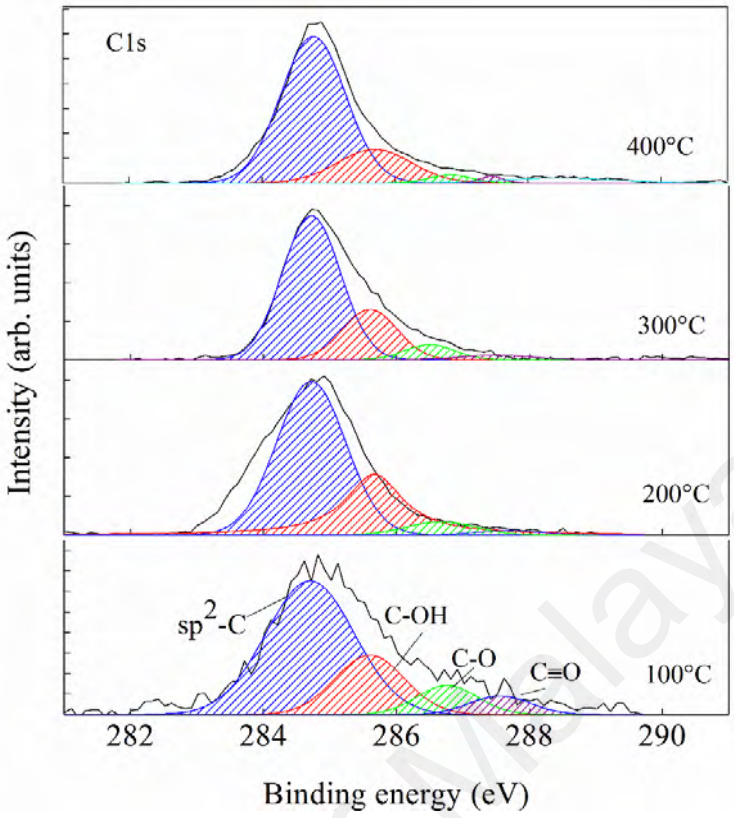


**Figure 5.22: High-resolution XPS scan for C 1s core level peak of transfer-free graphene.**

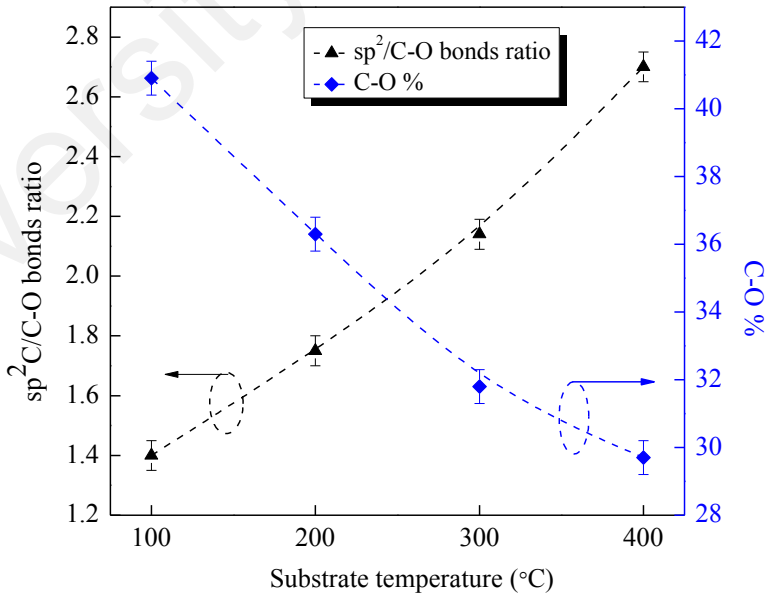


**Figure 5.23: The area ratio of $sp^2$-C to C bonded to O peak and percentage of oxygenated bond as a function of substrate temperature.**

University of Malaya

The studies on the role of O content in graphene films are crucial for the generation of a finite energy gap in the graphene structure. This leads to the changes in characteristic in the films (Nourbakhsh et al., 2010). The variation in the O content in the films that is calculated from the C1s spectra is displayed in Figure 5.23. Apparently, C-O increased almost linearly with the decrease in $T_S$ reaching a maximum value at $T_S$ of 100 °C, whereby an additional peak corresponding to C≡O bondings with binding energy centered at 287.5 eV appeared. The characteristics of O bonding were also evident from O1s spectra as shown in Figure 5.24. These spectra were deconvoluted for three corresponding bonds, namely hydroxides, C-OH/C-O, and C-C=O/O-C=O bonds centered at binding energy of 531.8 eV, 532.9 eV and 534 eV, respectively (Lim et al., 1990; Rosenthal et al., 2010; Yang et al., 2009). The most prominent bond existed was in the form of C-OH or C-O bond. The increase in the oxygenated functional group in the film as the $T_S$ decreases indicates that the bond length and bond disorder in C network were higher at lower temperature (Paul et al., 2008). Since C dissociation at the surface of the growing film are instegated by the repeated transfer of energy from energetic electron as well as neutral gas atoms, the reduction of surface temperature would reduce their energy as well as the dissociation (Hazra et al., 2010). This, inturn, would lead to the imperfection of the hexagonal graphene formation, which may produce some sites that form five- or seven-membered rings (Kudin et al., 2008; Vlassiouk et al., 2011). These disordered structures and defects would be mostly formed at the edges of stacked graphenes sheet that are produced from films with high number of graphene layers.

University of Malaya

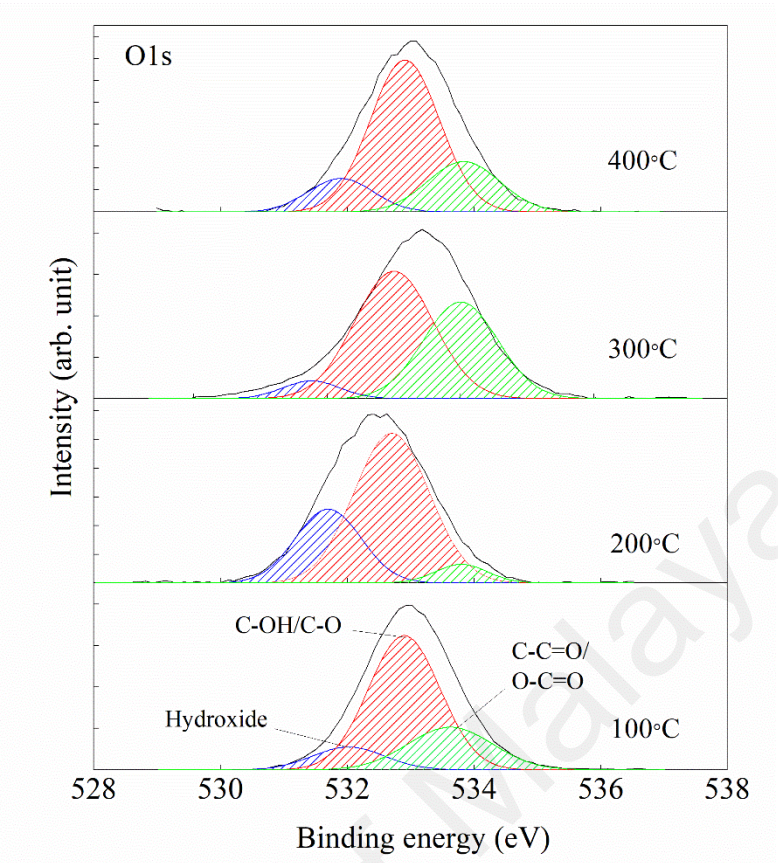


**Figure 5.24: High-resolution XPS scan for O 1s core level peak of transfer-free graphene.**

University of Malaya

## 5.5 Role of Substrate Temperature on the Hydrophobicity and Magnetic Properties of Graphene

### 5.5.1 Influence of Morphology and Chemical Bonding on the Contact Angle and Wetting Properties of the Graphene Film

This section discusses the wettability of the graphene film by performing the water $C_A$ measurement in terms of surface morphology and their chemical bonding. The films obtained by varying substrate temperature ($T_S$) from the previous section were used. The contact angle ($C_A$) measurements with their corresponding water droplet images are shown in Figure 5.25. In addition, the figure includes the films corresponding to FESEM images. The bare $SiO_2$ substrate exhibited hydrophilic surface with $C_A$ of approximately 65.4°. The $C_A$ increased to 66.5° for graphene deposited at $T_S$ of 100 °C, in which the value of the $C_A$ was the closest to the $SiO_2$ substrate. For the film grown at $T_S$ of 200 °C, the value of $C_A$ was increased drastically to 102.4° and decreased to 80.1° and 83.8° for film grown at $T_S$ of 300 °C and 400 °C, respectively. The FESEM images of the films demonstrate that the apparent surface area of the graphene as a contact surface between water droplet and the films surface. From the FESEM image, film grown at $T_S$ of 100 °C exhibited smooth and flat film surface, which indicates the highest number of stacking layers in the previous analysis. Furthermore, the water tends to spread easily on the film surface as the graphene film had smooth surface morphology. The FESEM images demonstrated that the densely wrinkled graphene with porous-like structure film were formed for film grown at $T_S$ of 200 °C and 300 °C. The film surface structure created an air gap or air pocket to allow air trap. It also provided a floating force to resist water penetration and thus inducing water repellency. This resulted in the increase in $C_A$ value for both films ($T_S$ = 200 °C and 300 °C) and had the highest $C_A$ value (102.4°) for film

University of Malaya

grown at $T_S$ of 200 °C, in which the value was relatively high for the PECVD graphene growth ( Kim et al., 2014; Shih et al., 2013).

Apart from the surface area of the graphene, the chemical bonding of the films also contributed to the changes in the films wettability. This demonstrates through the variation in $C_A$ value and C-OH bonding of the graphene film (Figure 5.26). Furthermore, the link between the C-OH bonding and $C_A$ is illustrated in Figure 5.27. The O-H bonding in the films could influence the polarity of the water molecules as well as the $C_A$ of the films. In addition, the film with high O-H content could create polar regimes, which attracts H ions from the water molecules. This could increase the surface energy and wettability that induce hydrophilic behavior ($C_A$<90), which mirrored by the $C_A$ of the film. In contrast, for $T_S$ of 200 °C, the value of $C_A$ was the highest, which corresponded to the lowest value of C-OH bonding in the film. The lower inclusion of C-OH content in the film, reduced the chemical attachment of the films to the water molecule and hence improved its hydrophobic properties. Therefore, this film is categorized as hydrophobic.

The film grown at $T_S$ of 400 °C demonstrated an increased in the $C_A$ with the value of ~83.8° even though it has smooth films surface with lower number of layers. The increase in the $C_A$ might be due to the decrease in surface tension as the number of layer decreases. The lower number of layer led to the lower van der Waals interaction between water and film due to the elimination of closer graphitic planes, and, thus increased the $C_A$ value. Moreover, the well-ordered structure of $sp^2$-C of the film exhibited weak polarity and created non-polar regime in the films, which in turn decreased the attraction of polar water molecules. This result supports the computed calculation of surface-tension values reported by Chih et. al., where water tends to be stagnant at lower number of graphene layer, and dampened the film surface with low value of surface tension. Ultimately, this increased the total surface free energy and thus resulted in increase in $C_A$ value.

University of Malaya

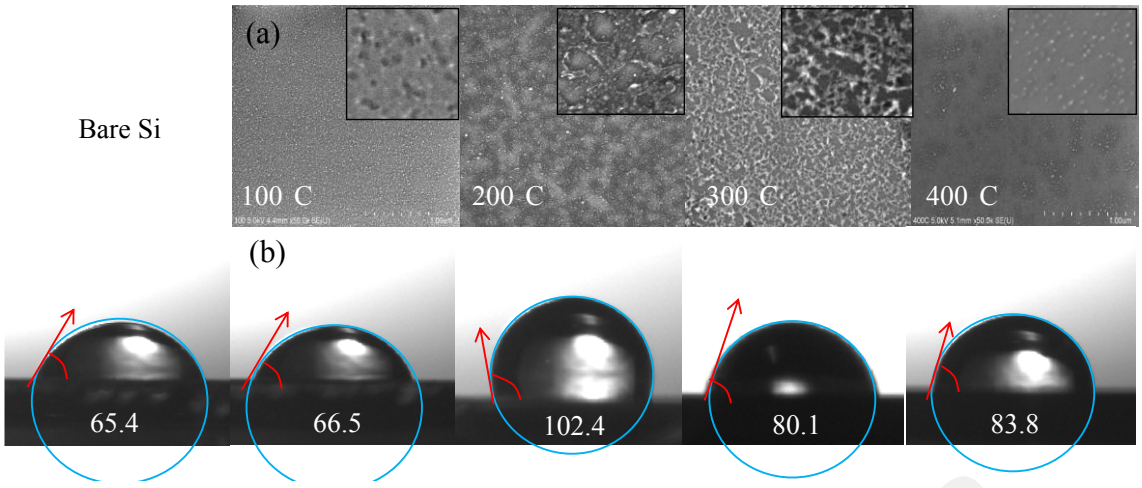


**Figure 5.25: FESEM images of the graphene surfaces deposited as a function of substrate temperature with high magnification of the FESEM, and (b) water contact angle, $\theta_W$ and corresponded image of water droplet on graphene films.**

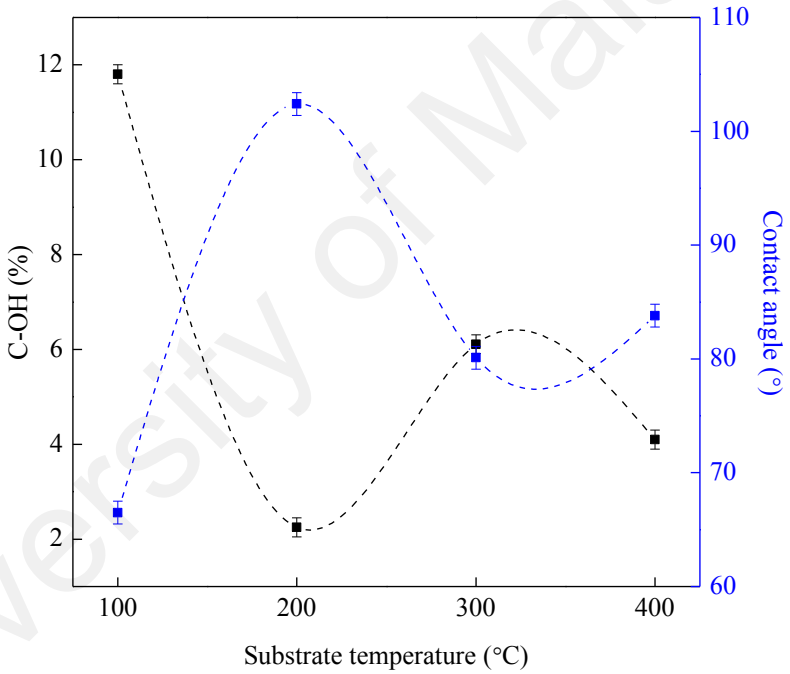


**Figure 5.26: The variation in C-OH content and water contact angle values of graphene film as a function of substrate temperature.**

University of Malaya

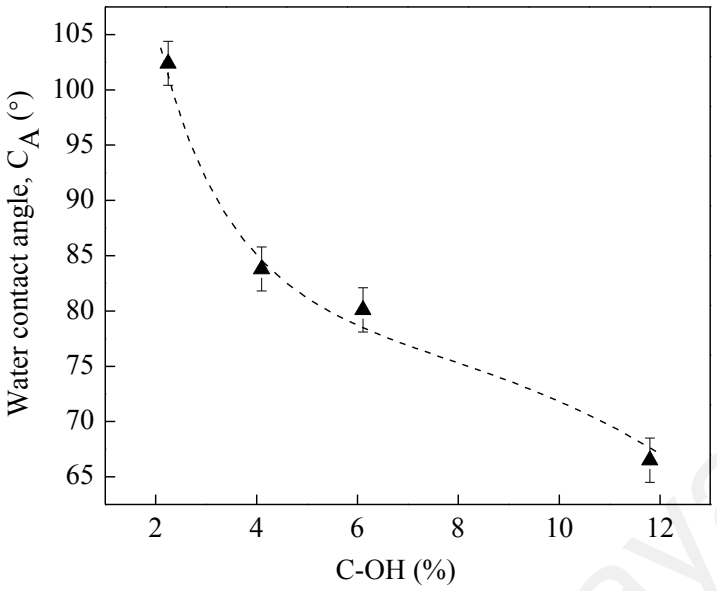


**Figure 5.27: Variation in water contact angle of graphene as a function of C-OH bonding.**

### 5.5.2 Defect-induced Magnetic Properties of Graphene: A Study of the Influence of Substrate Temperature

The defects in graphene have local magnetic moments, which induce magnetic ordering within its films. Thus, this section discusses the influence of defects in the graphitic network to the magnetism for graphene. $T_S$ value was used as a parameter for this study as defects vary for the films produced at different $T_S$ values. The magnetic properties of the films were measured at room temperature using Lakeshore vibrating sample magnetometer (VSM) in which Lakeshore VSM software was used for the analysis. As reference, the magnetic properties of a $SiO_2$/Si blank substrate were measured to eliminate substrate background. The findings indicated that the blank substrate produced a hysteresis loop of absolute diamagnetism as shown in Figure 5.28.

Figure 5.29 and Figure 5.30 illustrate the hysteresis loop of graphene deposited at different $T_S$ before and after subtracting the linear diamagnetic substrate background, respectively. The films apparently demonstrated ferromagnetism behavior as observed in

University of Malaya

the enlarged hysteresis loops in Figure 5.31. From these hysteresis loop, the saturation magnetization ($M_S$) of the films were determined.

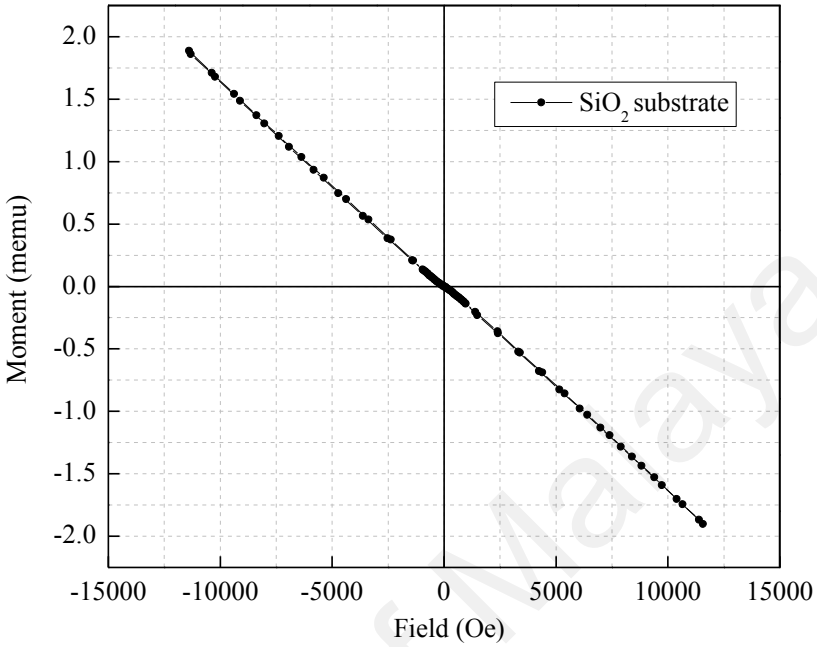


**Figure 5.28: Magnetization hysteresis loop for bare $SiO_2$/Si substrate.**

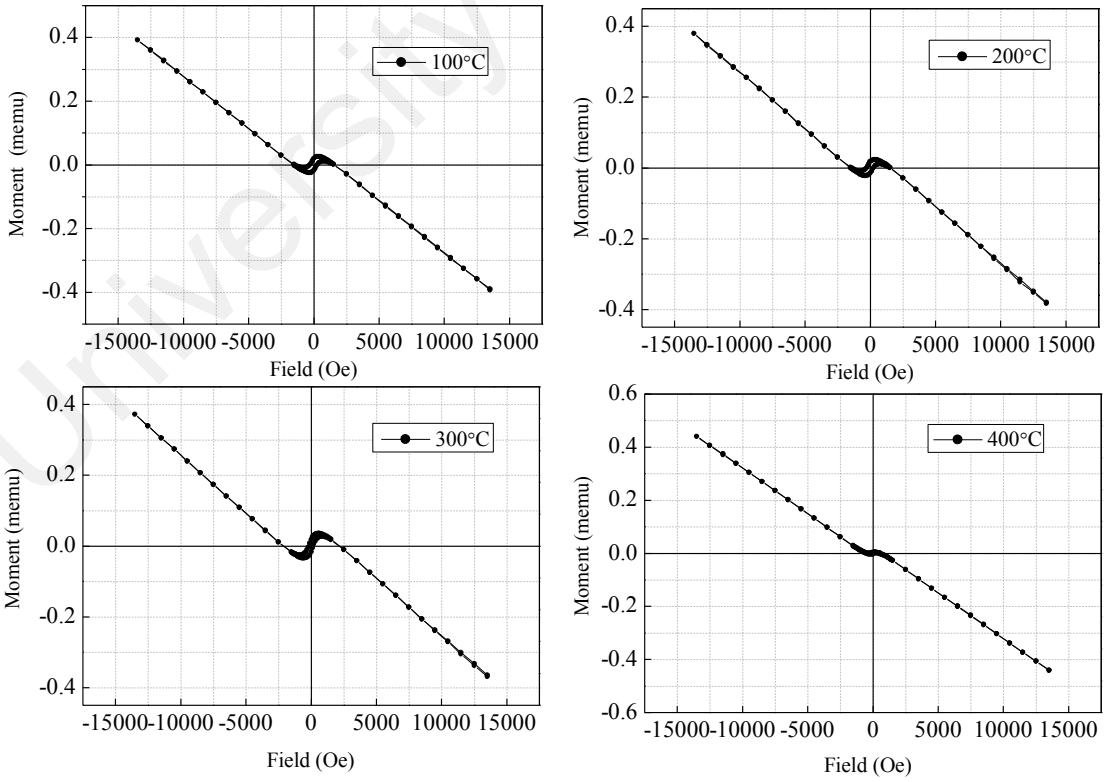


**Figure 5.29: Hysteresis loop of graphene deposited at different substrate temperature before substrate background.**

University of Malaya

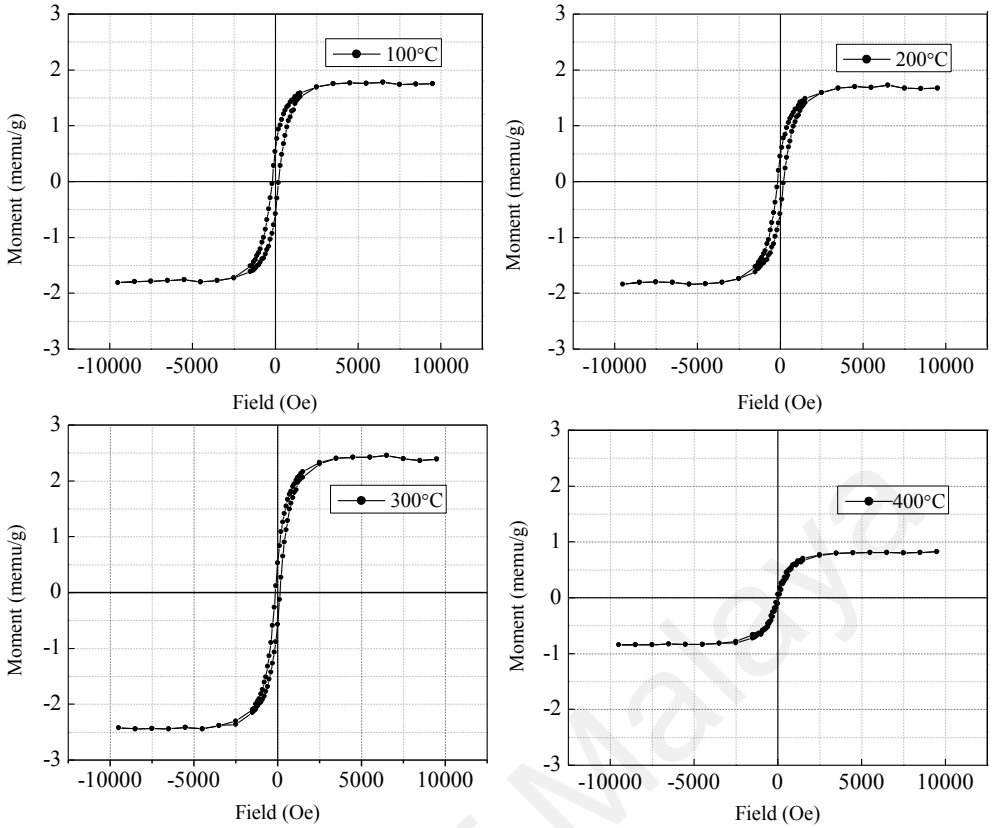


**Figure 5.30: Hysteresis loop after the subtraction of the diamagnetic background divided.**

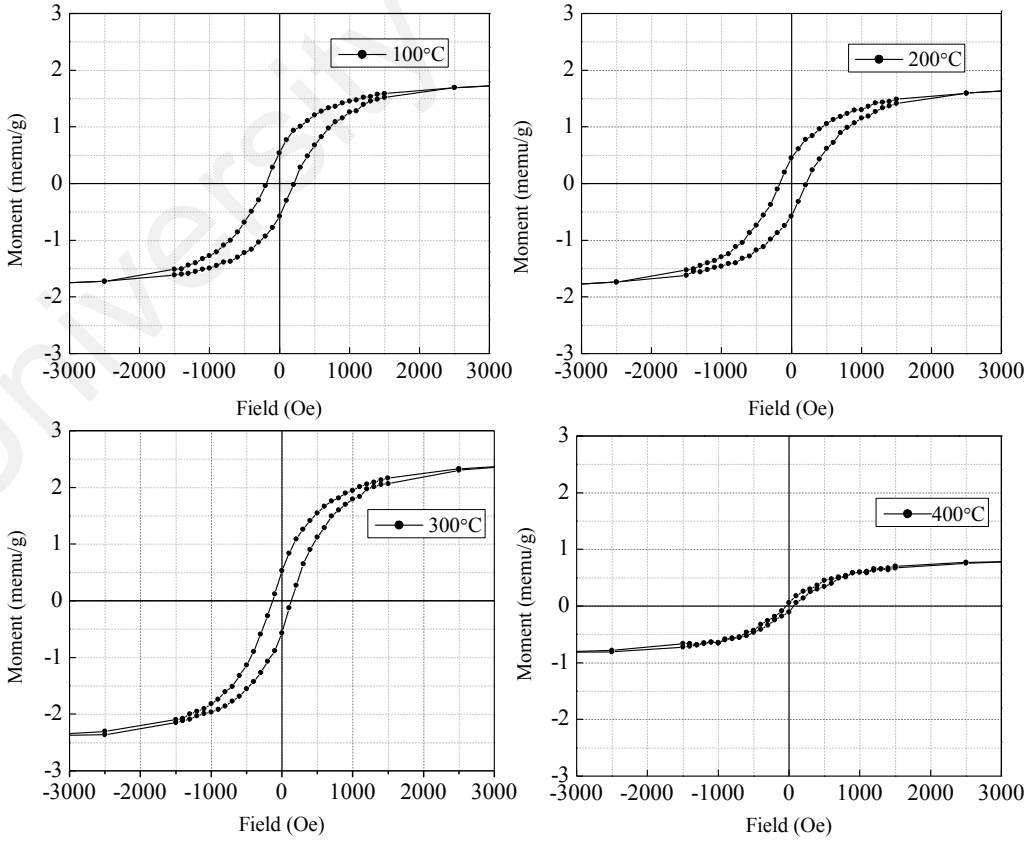


**Figure 5.31: Magnetization hysteresis loops for graphene at different Ts.**

University of Malaya

The observed ferromagnetism indicates that these graphene films had intrinsic magnetic behavior. The saturation magnetization of the films is shown in Figure 5.32. This magnetic behavior is attributed to vacancy defects and ultra-long defective edges. Hence, in general, the defects in graphene could possibly induce magnetic response due to localized unpaired spins caused by the unpaired electrons from the C atom. As such, these magnetization values could be equivalent to the number of unpaired electrons of these atoms. The lattice vacancies generate localized electronic states and magnetic moments due to the hybridization of $p_z$ orbitals in the $\pi$ band (Yazyev, 2010). Unlike adatoms, vacancies immobile at room temperature and cannot form cluster. Nevertheless, their contribution to magnetism is expected to be similar to that of adatoms as the defects led to the formation of localized states energies corresponding to vanishing density of state (Neto et al., 2009). Based on the theoretical calculation performed by Yazyev and Helm, the vacancy defects in the same sublattice has induced ferromagnetic ordering and the calculated magnetic moments are estimated at 1.12-1.53 $\mu$B per vacancy defects based on the defect concentration (Yazyev et al., 2007). Nevertheless, the ferromagnetic of the magnetization is not directly proportionate to the defects formed in our samples as indicated in Figure 5.33. The graph represents the correlation between $I_D/I_G$ ratio and magnetic saturation as a function of $T_S$. Even though graphene deposited at lower $T_S$ (100 °C and 200 °C), it had higher $I_D/I_G$ ratio, which corresponds to higher defects, indicating low magnetic properties. This may imply that the defects in these films may be non-magnetic produced as double vacancies, chemically terminated dangling bonds, Stone-Wales defects and similar non-magnetic defective sites (López-Sancho et al., 2009). In addition, multiple-atom vacancies can be viewed as an ensemble of neighboring single-atoms vacancies, which change the number of atoms and thus produce a net magnetic moment.

University of Malaya

The saturation magnetization value was increased for film deposited at $T_S$ of 300 °C. The non-uniform growth of graphene as seen in its previous FESEM image (Figure 5.25) resulted in the exposure of graphene edges. The defective edges that normally formed zigzag-edge, absorbed H and led to the formation of spin-polarized band at Fermi level (Wang et al., 2008). The H atoms that were bonded to the edges may passivate $\sigma$ dangling bonds and saturating $\pi$ orbital and induced magnetic moments, thus led to the increase in saturation magnetization. A remarkable decreased in the saturation magnetization value was observed with further increase in $T_S$ (400 °C). This is due to the significant reduction in films defects at higher deposition temperature. At this temperature, both vacancy defects and ultra-long defective edges were reduced and resulted in the lower magnetic effects of the films.

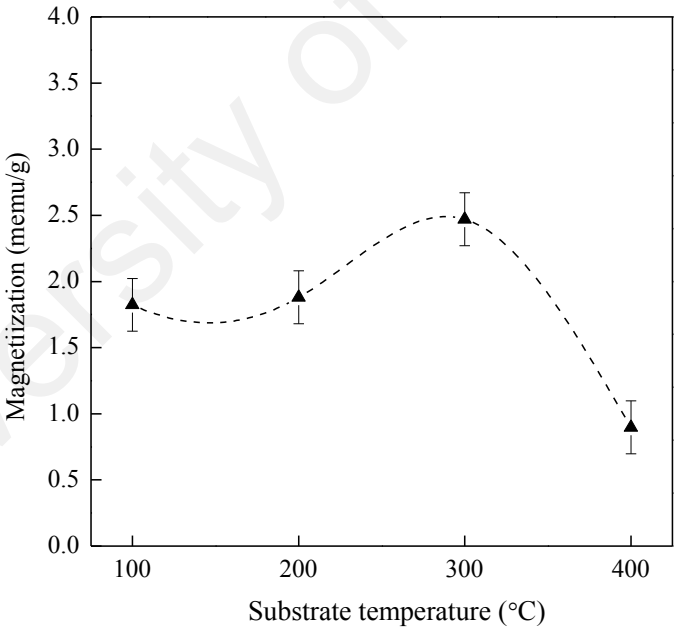


**Figure 5.32: Saturation magnetization of films as a function of substrate temperature.**

University of Malaya

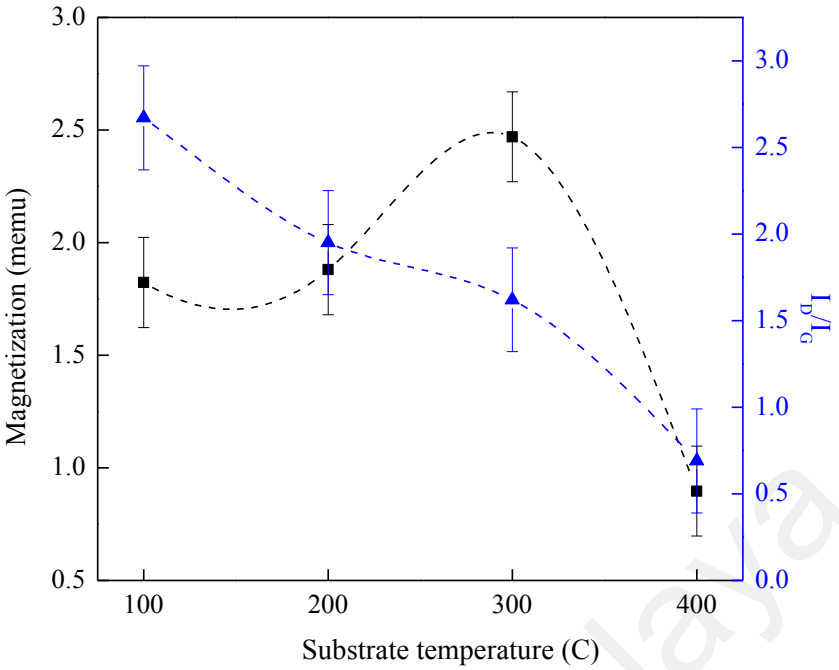


**Figure 5.33: Saturation magnetization and $I_D/I_G$ ratio of graphene as a function of substrate temperature.**

## 5.6 Summary

Transfer-free graphene were synthesized via HF-PECVD using Ni catalyst at relatively low temperature of 620 °C. Furthermore, the addition of hot-filament to the PECVD system influenced the formation of graphene growth as the morphology and size of the Ni grains changed. The increase in temperature from the radiant heat of the filament changed the Ni grains from nano-sized to micro-sized and reduced the formation of Ni grains boundaries. This resulted in the formation of better quality of graphene as compared to graphene grown from PECVD system alone. The reduction in the deposition time decreased the number of graphene layers, where there were increase in the defects of films. This is due to the limitation of C diffused through the Ni layers. In addition, the decrease in substrate temperature, which was lower than $T_S$ of 400 °C resulted in the defective graphene. The morphology of the graphene film grown at $T_S$ of 200 °C demonstrated the characteristic of hydrophobic with high contact angle value of 102.4°.

University of Malaya

Moreover, vacancy defects and highly defects formed at the edges influenced the magnetic properties of the graphene films.

University of Malaya

# CHAPTER 6: CONCLUSION AND SUGGESTION FOR FUTURE WORK

## 6.1 Conclusion

To the best of the author's knowledge, this is the first study that investigated on the fabrication of transfer-free graphene using nickel catalyst via HF-PECVD. The transfer-free graphene films with large surface area were successfully produced from $CH_4$ and $H_2$ mixture at low temperature of approximately 400 °C on $SiO_2$ substrates. In the first part of this work, transfer-free graphene was produced using PECVD at different thickness of Ni films. In this regard, various electrode distance values were used to study the thickness and grains size of the Ni films, which contributed to the growth of graphene films. The effects were varied according to the diffusion and precipitation rate of C atoms towards $Ni/SiO_2$ interface and grains boundaries, respectively. Moreover, the formation of higher growth rate of C atoms onto the substrate due to strong linkage between the top C layer and nc-G layer resulted in the formation of thick carbon film. On the other hand, the separation of the linkage due to higher Ni thickness resulted in the formation of graphene. The separation of the top layer and the nc-G layer were performed in the acid solution. Though this technique successfully produced large area of transfer-free graphene at low temperature, the high-intensity of D peak and significant observation of D'+G' peak in the Raman spectra demonstrated that the grown graphene films were defective.

In the second part of this work, hot-filament was introduced into the PECVD system, where it is named as HF-PECVD. The deposition parameters were fixed similar to the growth of graphene using PECVD except the deposition temperature, which was increased to 620 °C. In the matter of this, the increase in temperature was related to the radiant heat from the hot-filament located above the sample. In this study, Ni film with thickness of 150 nm was chosen as it produced graphene with less defects in the first part of this study. Fundamentally, the radiant heat from the hot-filament strongly affected the

University of Malaya

morphological, structure and chemical bonding properties of the Ni films and the formation of graphene layers. Furthermore, the size of Ni grains indicated remarkable increase for the graphene grown using HF-PECVD, while the Ni grains size remained the same as bare Ni films for graphene grown from PECVD system. The increased in size of the grains due to the agglomerations resulted in larger grains size boundaries. Moreover, due to the thermal annealing effects of the heat radiation from the hot-filament, the O contamination of the Ni catalyst disappeared. Thus, both effects led to the growth of more uniform and better quality of graphene as the films were wrinkle-free and the defects activated band of D'+G' were disappeared. Moreover, the decrease in both $I_D/I_G$ ratio and FWHM G indicated the formation of well-ordered graphitic structured graphene that were corresponded to the decrease in defects of films. This is because the small Ni grains size led to the formation of wrinkled graphene due to the tendency of C atoms to congregate or form at the edges along the Ni boundaries. Besides, the O contamination in the catalyst affected the quality of grown graphene by increasing the defects in the graphitic networks. In addition, the findings demonstrated that the number of graphene layers were reduced and graphitic structure of the graphene was improved as the deposition time decreased. Consequently, the decrease in number of graphene layers reduced the area of graphene edges, which corresponded to the dangling bonds that allowed O to be easily bonded as post-deposition contaminant.

Different substrate temperature points had significant effects on the graphene films properties. The current study indicated that 400 °C was the optimum substrate temperature for growing a good quality of transfer-free graphene. On the other hand, reduction in the substrate temperature revealed variation in D'+G' band as well as the D peak intensity, which corresponded to the increase in defects and leading to lower quality graphene films. This is due to the impinging C atoms or ions in growing surface caused the loss of higher energy at substrate temperature lower than 400 °C, which in turn formed

University of Malaya

more disordered graphene film with lower number of six-fold rings structures. Moreover, the graphitic C=C bonding in the films decreased as the substrate temperature decreased, which corresponded to the shift of $sp^2$-C bond to higher binding energy in XPS spectra. The increase in the films defects, however, correlated to the increase in the number of graphene layers and O content in the graphene films as the substrate temperature decreased. Graphene film with $T_S$ of 200 °C indicated the highest $C_A$ value of 102.4°. Furthermore, the stacking of graphene layers formed from the multilayered graphene created films surface structure with air pocket to allow air trap. This provided floating force to resist water penetration and in turn water repellency. Besides the surface structure of the film, the lowest value of C-OH bonding in the films lowered the chemical attachment of the film to the water molecule and hence improved the hydrophobic properties. Moreover, the non-uniform growth that exposed the graphene edges for film grown at $T_S$ of 300 °C demonstrated an increase in magnetic response attributed to the ultra-long defective edge. The defective edges absorbed the H and led to the passivation of $\sigma$ dangling bonds and caused the $\pi$ orbital saturated. The presence of a vacancy (due to the defective edge) creates unsaturated $sp^2$ or $\pi$ orbital in the neighboring atoms. This situation leads to the reconstruction of lattice where each sigma-dangling bond is passivated with one hydrogen atom. Therefore, a single atomic vacancy with full hydrogen termination of sigma-dangling bonds and additional hydrogen passivation of the extended $\pi$ state at one of the vacancy's monohydrogenated carbon atoms is characterized by complete quenching of low-energy localized states. Subsequently, this resulted in the increase in saturation magnetization value.

In summary, transfer-free graphene produced from hot-filament PECVD exhibited better quality graphene as compared to PECVD. This is due to the enhancement in structure, morphology and chemical bonding of the graphene films. The number of layer and defects in the graphene films could be improved by reducing the deposition time.



University of Malaya

Essentially, towards producing better quality of transfer-free graphene at low temperature, the defects found in the film could be an advantage for enhancing the hydrophobicity and magnetic properties of the graphene films.

## 6.2 Future Work

The growth of transfer-free graphene using HF-PECVD is a promising technique for the synthesis of graphene films. Moreover, the low-temperature synthesis led to the growth of graphene on various substrates. In light of this, future studies should focus on many other aspects pertaining to this technique for a better understanding and application. Therefore, the following suggestions are proposed for future investigations:

- Additional characterization methods to investigate the graphene film such as hardness, electrical and optical properties.
- Synthesis of transfer-free graphene on the transparent substrate such as quartz to measure the transparency of the graphene films for transparent electrode application.
- Focusing on the study of synthesis defects-free of transfer-free graphene using HF-PECVD to enhance the electrical properties of the graphene films.
- Producing large scale of defect-free monolayer transfer-free graphene using HF-PECVD technique at relatively low deposition temperature.

University of Malaya

## REFERENCES


Adams, D. J., Gröning, O., Pignedoli, C. A., Ruffieux, P., Fasel, R., & Passerone, D. (2012). Stable ferromagnetism and doping-induced half-metallicity in asymmetric graphene nanoribbons. *Physical Review B, 85*(24), 245405.

Allen, M. J., Tung, V. C., & Kaner, R. B. (2009). Honeycomb carbon: A review of graphene. *Chemical Reviews, 110*(1), 132-145.

An, S., Lee, G.-H., Jang, S. W., Hwang, S., Lim, S. H., & Han, S. (2016). A facile method for the synthesis of transfer-free graphene from co-deposited nickel–carbon layers. *Carbon, 109*, 154-162.

Ando, T., Nakanishi, T., & Saito, R. (1998). Berry's phase and absence of back scattering in carbon nanotubes. *Journal of the Physical Society of Japan, 67*(8), 2857-2862.

Andriotis, A. N., Menon, M., Sheetz, R. M., & Chernozatonskii, L. (2003). Magnetic properties of $C_{60}$ polymers. *Physical Review Letters, 90*(2), 026801.

Andújar, J. L., Pino, F. J., Polo, M. C., Pinyol, A., Corbella, C., & Bertran, E. (2002). Effects of gas pressure and r.f. power on the growth and properties of magnetron sputter deposited amorphous carbon thin films. *Diamond and Related Materials, 11*(3–6), 1005-1009.

Ansari, N., Nazari, F., & Illas, F. (2014). Line defects and induced doping effects in graphene, hexagonal boron nitride and hybrid BNC. *Physical Chemistry Chemical Physics, 16*(39), 21473-21485.

Bae, S., Kim, H., Lee, Y., Xu, X., Park, J.-S., Zheng, Y., . . . Song, Y. I. (2010). Roll-to-roll production of 30-inch graphene films for transparent electrodes. *Nature Nanotechnology, 5*(8), 574-578.

Balluffi, R., & Bkakely, J. (1975). Special aspects of diffusion in thin films. *Thin Solid Films, 25*(2), 363-392.

Baskin, Y., & Meyer, L. (1955). Lattice constants of graphite at low temperatures. *Physical Review, 100*(2), 544.

Berger, C., Song, Z., Li, T., Li, X., Ogbazghi, A. Y., Feng, R., . . . First, P. N. (2004). Ultrathin epitaxial graphite: 2D electron gas properties and a route toward graphene-based nanoelectronics. *The Journal of Physical Chemistry B, 108*(52), 19912-19916.

Cao, L., Jones, A. K., Sikka, V. K., Wu, J., & Gao, D. (2009). Anti-icing superhydrophobic coatings. *Langmuir, 25*(21), 12444-12448.

Castelaín, M., Martínez, G., Merino, P., Martín-Gago, J. Á., Segura, J. L., Ellis, G., & Salavagione, H. J. (2012). Graphene functionalisation with a conjugated poly (fluorene) by click coupling: Striking electronic properties in solution. *Chemistry-A European Journal, 18*(16), 4965-4973.


University of Malaya

Červenka, J., Katsnelson, M., & Flipse, C. (2009). Room-temperature ferromagnetism in graphite driven by two-dimensional networks of point defects. *Nature Physics, 5*(11), 840-844.

Chae, S. J., Güneş, F., Kim, K. K., Kim, E. S., Han, G. H., Kim, S. M., . . . Park, M. H. (2009). Synthesis of large-area graphene layers on poly-nickel substrate by chemical vapor deposition: Wrinkle formation. *Advanced Materials, 21*(22), 2328-2333.

Charlier, J.-C., Gonze, X., & Michenaud, J.-P. (1994). First-principles study of the stacking effect on the electronic properties of graphite (s). *Carbon, 32*(2), 289-299.

Chen, J., Guo, Y., Wen, Y., Huang, L., Xue, Y., Geng, D., . . . Liu, Y. (2013). Two-stage metal-catalyst-free growth of high-quality polycrystalline graphene films on silicon nitride substrates. *Advanced Materials, 25*(7), 992-997.

Chen, J., Wen, Y., Guo, Y., Wu, B., Huang, L., Xue, Y., . . . Liu, Y. (2011). Oxygen-aided synthesis of polycrystalline graphene on silicon dioxide substrates. *Journal of the American Chemical Society, 133*(44), 17548-17551.

Chen, X., Akinwande, D., Lee, K.-J., Close, G. F., Yasuda, S., Paul, B. C., . . . Wong, H.-S. P. (2010). Fully integrated graphene and carbon nanotube interconnects for gigahertz high-speed CMOS electronics. *IEEE Transactions on Electron Devices, 57*(11), 3137-3143.

Coraux, J., Engler, M., Busse, C., Wall, D., Buckanie, N., Zu Heringdorf, F.-J. M., . . . Michely, T. (2009). Growth of graphene on Ir (111). *New Journal of Physics, 11*(2), 023006.

Coraux, J., N 'Diaye, A. T., Busse, C., & Michely, T. (2008). Structural coherency of graphene on Ir (111). *Nano letters, 8*(2), 565-570.

Cullity, B. D., & Weymouth, J. W. (1957). Elements of X-ray Diffraction. *American Journal of Physics, 25*(6), 394-395.

De Arco, L. G., Zhang, Y., Kumar, A., & Zhou, C. (2009). Synthesis, transfer, and devices of single-and few-layer graphene by chemical vapor deposition. *IEEE Transactions on Nanotechnology, 8*(2), 135-138.

De Martino, A., Dell'Anna, L., & Egger, R. (2007). Magnetic confinement of massless Dirac fermions in graphene. *Physical Review Letters, 98*(6), 066802.

Dikin, D. A., Stankovich, S., Zimney, E. J., Piner, R. D., Dommett, G. H., Evmenenko, G., . . . Ruoff, R. S. (2007). Preparation and characterization of graphene oxide paper. *Nature, 448*(7152), 457-460.

Du, C., & Pan, N. (2005). CVD growth of carbon nanotubes directly on nickel substrate. *Materials Letters, 59*(13), 1678-1682.

University of Malaya

Eastman, M., Hedinger, D., Qian, W., Hudson, W., Jiang, B., & Jiao, J. (2014). Raman spectroscopy and band structure of Pd-hybridized multilayer graphene. *Carbon, 68*, 687-694.

El-Kadry, N., Ashour, A., & Mahmoud, S. A. (1995). Structural dependence of d.c. electrical properties of physically deposited CdTe thin films. *Thin Solid Films, 269*(1–2), 112-116.

Ellis, A. V., Vijayamohanan, K., Goswami, R., Chakrapani, N., Ramanathan, L., Ajayan, P. M., & Ramanath, G. (2003). Hydrophobic anchoring of monolayer-protected gold nanoclusters to carbon nanotubes. *Nano Letters, 3*(3), 279-282.

Emtsev, K. V., Bostwick, A., Horn, K., Jobst, J., Kellogg, G. L., Ley, L., . . . Röhrl, J. (2009). Towards wafer-size graphene layers by atmospheric pressure graphitization of silicon carbide. *Nature Materials, 8*(3), 203-207.

Falicov, L., Pierce, D. T., Bader, S., Gronsky, R., Hathaway, K. B., Hopster, H. J., . . . Salamon, M. (1990). Surface, interface, and thin-film magnetism. *Journal of Materials Research, 5*(6), 1299-1340.

Feng, L., Zhang, Z., Mai, Z., Ma, Y., Liu, B., Jiang, L., & Zhu, D. (2004). A super-hydrophobic and super-oleophilic coating mesh film for the separation of oil and water. *Angewandte Chemie International Edition, 43*(15), 2012-2014.

Ferrari, A., Meyer, J., Scardaci, V., Casiraghi, C., Lazzeri, M., Mauri, F., . . . Roth, S. (2006). Raman spectrum of graphene and graphene layers. *Physical Review Letters, 97*(18), 187401.

Ferrari, A. C. (2007). Raman spectroscopy of graphene and graphite: disorder, electron–phonon coupling, doping and nonadiabatic effects. *Solid State Communications, 143*(1), 47-57.

Ferrari, A. C., Meyer, J., Scardaci, V., Casiraghi, C., Lazzeri, M., Mauri, F., . . . Roth, S. (2006). Raman spectrum of graphene and graphene layers. *Physical Review Letters, 97*(18), 187401.

Ferro, Y., Teillet-Billy, D., Rougeau, N., Sidis, V., Morisset, S., & Allouche, A. (2008). Stability and magnetism of hydrogen dimers on graphene. *Physical Review B, 78*(8), 085417.

Fisher, J. C. (1951). Calculation of diffusion penetration curves for surface and grain boundary diffusion. *Journal of Applied Physics, 22*(1), 74-77.

Frank, S., Poncharal, P., Wang, Z., & De Heer, W. A. (1998). Carbon nanotube quantum resistors. *Science, 280*(5370), 1744-1746.

Garcia, J. M., He, R., Jiang, M. P., Kim, P., Pfeiffer, L. N., & Pinczuk, A. (2011). Multilayer graphene grown by precipitation upon cooling of nickel on diamond. *Carbon, 49*(3), 1006-1012.

Gass, M. H., Bangert, U., Bleloch, A. L., Wang, P., Nair, R. R., & Geim, A. (2008). Free-standing graphene at atomic resolution. *Nature Nanotechnology, 3*(11), 676-681.

University of Malaya

Goerbig, M. (2011). Electronic properties of graphene in a strong magnetic field. *Reviews of Modern Physics, 83*(4), 1193-1243.

Guinea, F., Neto, A. C., & Peres, N. (2006). Electronic states and Landau levels in graphene stacks. *Physical Review B, 73*(24), 245426.

Gupta, A., Chen, G., Joshi, P., Tadigadapa, S., & Eklund, P. (2006). Raman scattering from high-frequency phonons in supported n-graphene layer films. *Nano Letters, 6*(12), 2667-2673.

Haering, R. (1958). Band structure of rhombohedral graphite. *Canadian Journal of Physics, 36*(3), 352-362.

Haldane, F. D. M. (1988). Model for a quantum Hall effect without Landau levels: Condensed-matter realization of the" parity anomaly". *Physical Review Letters, 61*(18), 2015-2018.

Han, J. T., Kim, S. Y., Woo, J. S., & Lee, G. W. (2008). Transparent, conductive, and superhydrophobic films from stabilized carbon nanotube/silane sol mixture solution. *Advanced Materials, 20*(19), 3724-3727.

Hass, J., De Heer, W., & Conrad, E. (2008). The growth and morphology of epitaxial multilayer graphene. *Journal of Physics: Condensed Matter, 20*(32), 323202.

Hass, J., Feng, R., Millan-Otoya, J., Li, X., Sprinkle, M., First, P. N., . . . Berger, C. (2007). Structural properties of the multilayer graphene/4 H−Si C (000 $1^{-}$) system as determined by surface x-ray diffraction. *Physical Review B, 75*(21), 214109.

Hazra, K., Rafiee, J., Rafiee, M., Mathur, A., Roy, S., McLauhglin, J., . . . Misra, D. (2010). Thinning of multilayer graphene to monolayer graphene in a plasma environment. *Nanotechnology, 22*(2), 025704.

Hernandez, Y., Nicolosi, V., Lotya, M., Blighe, F. M., Sun, Z., De, S., . . . Gun'Ko, Y. K. (2008). High-yield production of graphene by liquid-phase exfoliation of graphite. *Nature Nanotechnology, 3*(9), 563-568.

Hiramatsu, M., Shiji, K., Amano, H., & Hori, M. (2004). Fabrication of vertically aligned carbon nanowalls using capacitively coupled plasma-enhanced chemical vapor deposition assisted by hydrogen radical injection. *Applied Physics Letters, 84*(23), 4708-4710.

Hsieh, C.-T., & Chen, W.-Y. (2011). Water/oil repellency and work of adhesion of liquid droplets on graphene oxide and graphene surfaces. *Surface and Coatings Technology, 205*(19), 4554-4561.

Hsieh, C.-T., Chen, W.-Y., & Wu, F.-L. (2008). Fabrication and superhydrophobicity of fluorinated carbon fabrics with micro/nanoscaled two-tier roughness. *Carbon, 46*(9), 1218-1224.

Hsieh, C.-T., Lin, Y.-T., Lin, J.-Y., & Wei, J.-L. (2009). Synthesis of carbon nanotubes over Ni-and Co-supported $CaCO_3$ catalysts using catalytic chemical vapor deposition. *Materials Chemistry and Physics, 114*(2), 702-708.

University of Malaya

Huang, H., Chen, W., Chen, S., & Wee, A. T. S. (2008). Bottom-up growth of epitaxial graphene on 6H-SiC (0001). *ACS Nano, 2*(12), 2513-2518.

Humplik, T., Lee, J., O'hern, S., Fellman, B., Baig, M., Hassan, S., . . . Karnik, R. (2011). Nanostructured materials for water desalination. *Nanotechnology, 22*(29), 292001.

Ishihara, M., Li, S., Yumoto, H., Akashi, K., & Ide, Y. (1998). Control of preferential orientation of AlN films prepared by the reactive sputtering method. *Thin Solid Films, 316*(1), 152-157.

Jorio, A., Dresselhaus, M., Saito, R., & Dresselhaus, G. (2011). *Raman spectroscopy in graphene related systems*. Weinheim: Wiley-VCH Verlag.

Kar, J., Mukherjee, S., Bose, G., & Tuli, S. (2008). Effect of inter-electrode spacing on structural and electrical properties of RF sputtered AlN films. *Journal of Materials Science: Materials in Electronics, 19*(3), 261-265.

Karu, A. E., & Beer, M. (1966). Pyrolytic formation of highly crystalline graphite films. *Journal of Applied Physics, 37*(5), 2179-2181.

Katsnelson, M., & Novoselov, K. (2007). Graphene: New bridge between condensed matter physics and quantum electrodynamics. *Solid State Communications, 143*(1-2), 3-13.

Kim, G. T., Gim, S. J., Cho, S. M., Koratkar, N., & Oh, I. K. (2014). Wetting-transparent graphene films for hydrophobic water-harvesting surfaces. *Advanced Materials, 26*(30), 5166-5172.

Kim, K.-E., Kim, K.-J., Jung, W. S., Bae, S. Y., Park, J., Choi, J., & Choo, J. (2005). Investigation on the temperature-dependent growth rate of carbon nanotubes using chemical vapor deposition of ferrocene and acetylene. *Chemical Physics Letters, 401*(4), 459-464.

Kim, K. S., Zhao, Y., Jang, H., Lee, S. Y., Kim, J. M., Kim, K. S., . . . Hong, B. H. (2009). Large-scale pattern growth of graphene films for stretchable transparent electrodes. *Nature, 457*(7230), 706-710.

Kline, L. E., Partlow, W. D., & Bies, W. E. (1989). Electron and chemical kinetics in methane rf glow-discharge deposition plasmas. *Journal of Applied Physics, 65*(1), 70-78.

Koskinen, P., Malola, S., & Häkkinen, H. (2008). Self-passivating edge reconstructions of graphene. *Physical Review Letters, 101*(11), 115502.

Kotakoski, J., Krasheninnikov, A., & Nordlund, K. (2006). Energetics, structure, and long-range interaction of vacancy-type defects in carbon nanotubes: Atomistic simulations. *Physical Review B, 74*(24), 245420.

Krasheninnikov, A., Lehtinen, P., Foster, A., & Nieminen, R. (2006). Bending the rules: contrasting vacancy energetics and migration in graphite and carbon nanotubes. *Chemical Physics Letters, 418*(1-3), 132-136.

University of Malaya

Kudin, K. N., Ozbas, B., Schniepp, H. C., Prud'Homme, R. K., Aksay, I. A., & Car, R. (2008). Raman spectra of graphite oxide and functionalized graphene sheets. *Nano Letters, 8*(1), 36-41.

Kwak, J., Chu, J. H., Choi, J.-K., Park, S.-D., Go, H., Kim, S. Y., . . . Yoon, E. (2012). Near room-temperature synthesis of transfer-free graphene films. *Nature Communications, 3*, 645-652.

Lahiri, J., Lin, Y., Bozkurt, P., Oleynik, I. I., & Batzill, M. (2010). An extended defect in graphene as a metallic wire. *Nature Nanotechnology, 5*(5), 326-329.

Lahiri, J., Miller, T. S., Ross, A. J., Adamska, L., Oleynik, I. I., & Batzill, M. (2011). Graphene growth and stability at nickel surfaces. *New Journal of Physics, 13*(2), 025001.

Latil, S., & Henrard, L. (2006). Charge carriers in few-layer graphene films. *Physical Review Letters, 97*(3), 036803.

Lee, Y., Bae, S., Jang, H., Jang, S., Zhu, S.-E., Sim, S. H., . . . Ahn, J.-H. (2010). Wafer-scale synthesis and transfer of graphene films. *Nano Letters, 10*(2), 490-493.

Lee, Y. T., Kim, N. S., Park, J., Han, J. B., Choi, Y. S., Ryu, H., & Lee, H. J. (2003). Temperature-dependent growth of carbon nanotubes by pyrolysis of ferrocene and acetylene in the range between 700 and 1000 C. *Chemical Physics Letters, 372*(5), 853-859.

Lehtinen, P., Foster, A. S., Ayuela, A., Krasheninnikov, A., Nordlund, K., & Nieminen, R. M. (2003). Magnetic properties and diffusion of adatoms on a graphene sheet. *Physical Review Letters, 91*(1), 017202.

Lehtinen, P., Foster, A. S., Ma, Y., Krasheninnikov, A., & Nieminen, R. M. (2004). Irradiation-induced magnetism in graphite: a density functional study. *Physical Review Letters, 93*(18), 187202.

Li, M., Liu, D., Wei, D., Song, X., Wei, D., & Wee, A. T. S. (2016). Controllable synthesis of graphene by plasma-enhanced chemical vapor deposition and its related applications. *Advanced Science, 3*(11), 1600003.

Li, X., Cai, W., An, J., Kim, S., Nah, J., Yang, D., . . . Tutuc, E. (2009). Large-area synthesis of high-quality and uniform graphene films on copper foils. S*cience, 324*(5932), 1312-1314.

Li, X., Magnuson, C. W., Venugopal, A., Tromp, R. M., Hannon, J. B., Vogel, E. M., . . . Ruoff, R. S. (2011). Large-area graphene single crystals grown by low-pressure chemical vapor deposition of methane on copper. *Journal of the American Chemical Society, 133*(9), 2816-2819.

Li, X., Zhu, Y., Cai, W., Borysiak, M., Han, B., Chen, D., . . . Ruoff, R. S. (2009). Transfer of large-area graphene films for high-performance transparent conductive electrodes. *Nano Letters, 9*(12), 4359-4363.

University of Malaya

Liang, Z., Xu, Z., Yan, T., & Ding, F. (2014). Atomistic simulation and the mechanism of graphene amorphization under electron irradiation. *Nanoscale, 6*(4), 2082-2086.

Lim, A., & Atrens, A. (1990). ESCA studies of nitrogen-containing stainless steels. *Applied Physics A: Materials Science & Processing, 51*(5), 411-418.

Liu, L., Gao, J., Zhang, X., Yan, T., & Ding, F. (2014). Vacancy inter-layer migration in multi-layered graphene. *Nanoscale, 6*(11), 5729-5734.

Liu, L., Qing, M., Wang, Y., & Chen, S. (2015). Defects in graphene: generation, healing, and their effects on the properties of graphene: a review. *Journal of Materials Science & Technology, 31*(6), 599-606.

Liu, N., Fu, L., Dai, B., Yan, K., Liu, X., Zhao, R., . . . Liu, Z. (2010). Universal segregation growth approach to wafer-size graphene from non-noble metals. *Nano Letters, 11*(1), 297-303.

Liu, Z., Tang, J., Kang, C., Zou, C., Yan, W., & Xu, P. (2012). Effect of substrate temperature on few-layer graphene grown on Al 2 O 3 (0001) via direct carbon atoms deposition. *Solid State Communications, 152*(11), 960-963.

López-Sancho, M. P., de Juan, F., & Vozmediano, M. A. (2009). Magnetic moments in the presence of topological defects in graphene. *Physical Review B, 79*(7), 075413.

López, G., & Mittemeijer, E. (2004). The solubility of C in solid Cu. *Scripta Materialia, 51*(1), 1-5.

Losurdo, M., Giangregorio, M. M., Capezzuto, P., & Bruno, G. (2011). Graphene CVD growth on copper and nickel: Role of hydrogen in kinetics and structure. *Physical Chemistry Chemical Physics, 13*(46), 20836-20843.

Lotya, M., Hernandez, Y., King, P. J., Smith, R. J., Nicolosi, V., Karlsson, L. S., . . . McGovern, I. (2009). Liquid phase production of graphene by exfoliation of graphite in surfactant/water solutions. *Journal of the American Chemical Society, 131*(10), 3611-3620.

Luo, Z., Lu, Y., Singer, D. W., Berck, M. E., Somers, L. A., Goldsmith, B. R., & Johnson, A. C. (2011). Effect of substrate roughness and feedstock concentration on growth of wafer-scale graphene at atmospheric pressure. *Chemistry of Materials, 23*(6), 1441-1447.

Ma, E. (2004). Watching the nanograins roll. *Science, 305*(5684), 623-624.

Macháč, P., Hejna, O., & Slepička, P. (2017). Graphene growth by transfer-free chemical vapour deposition on a cobalt layer. *Journal of Electrical Engineering, 68*(1), 79-82.

Malard, L. M., Pimenta, M. A., Dresselhaus, G., & Dresselhaus, M. S. (2009a). Raman spectroscopy in graphene. *Physics Reports, 473*(5–6), 51-87.

University of Malaya

Malard, L. M., Pimenta, M. A., Dresselhaus, G., & Dresselhaus, M. S. (2009b). Raman spectroscopy in graphene. *Physics Reports, 473*(5), 51-87.

Mattevi, C., Kim, H., & Chhowalla, M. (2011). A review of chemical vapour deposition of graphene on copper. *Journal of Materials Chemistry, 21*(10), 3324-3334.

McCann, E., & Fal'ko, V. I. (2006). Landau-level degeneracy and quantum Hall effect in a graphite bilayer. *Physical Review Letters, 96*(8), 086805.

Meyer, J. C., Kisielowski, C., Erni, R., Rossell, M. D., Crommie, M., & Zettl, A. (2008). Direct imaging of lattice atoms and topological defects in graphene membranes. *Nano Letters, 8*(11), 3582-3586.

Miao, C., Zheng, C., Liang, O., & Xie, Y.-H. (2011). Chemical vapor deposition of graphene *Physics and Applications of Graphene-Experiments*: InTech.

Min, W. L., Jiang, B., & Jiang, P. (2008). Bioinspired Self-Cleaning Antireflection Coatings. *Advanced Materials, 20*(20), 3914-3918.

Mohsin, A., Liu, L., Liu, P., Deng, W., Ivanov, I. N., Li, G., . . . Xiao, K. (2013). Synthesis of millimeter-size hexagon-shaped graphene single crystals on resolidified copper. *ACS Nano, 7*(10), 8924-8931.

Muhammad Hafiz, S., Ritikos, R., Whitcher, T. J., Md Razib, N., Bien, D. C. S., Chanlek, N., . . . Huang, N. M. (2014). A practical carbon dioxide gas sensor using room-temperature hydrogen plasma reduced graphene oxide. *Sensors and Actuators B: Chemical, 193*, 692-700.

Natesan, K., & Kassner, T. (1973). Thermodynamics of carbon in nickel, iron-nickel and iron-chromium-nickel alloys. *Metallurgical Transactions, 4*(11), 2557-2566.

Neto, A. C., Guinea, F., Peres, N. M., Novoselov, K. S., & Geim, A. K. (2009). The electronic properties of graphene. *Reviews of Modern Physics, 81*(1), 109-162.

Neto, A. C., Kotov, V. N., Nilsson, J., Pereira, V. M., Peres, N. M., & Uchoa, B. (2009). Adatoms in graphene. *Solid State Communications, 149*(27), 1094-1100.

Nourbakhsh, A., Cantoro, M., Vosch, T., Pourtois, G., Clemente, F., van der Veen, M. H., . . . Sels, B. F. (2010). Bandgap opening in oxygen plasma-treated graphene. *Nanotechnology, 21*(43), 435203.

Novoselov, K. S., Geim, A. K., Morozov, S., Jiang, D., Zhang, Y., Dubonos, S. a., . . . Firsov, A. (2004). Electric field effect in atomically thin carbon films. S*cience, 306*(5696), 666-669.

Novoselov, K. S., Jiang, Z., Zhang, Y., Morozov, S., Stormer, H. L., Zeitler, U., . . . Geim, A. K. (2007). Room-temperature quantum Hall effect in graphene. *Science, 315*(5817), 1379-1379.

Obraztsov, A., Obraztsova, E., Tyurnina, A., & Zolotukhin, A. (2007). Chemical vapor deposition of thin graphite films of nanometer thickness. *Carbon, 45*(10), 2017-2021.

University of Malaya

Obraztsov, A. N. (2009). Chemical vapour deposition: Making graphene on a large scale. *Nature Nanotechnology, 4*(4), 212-213.

Othman, M., Ritikos, R., Muhammad Hafiz, S., Khanis, N. H., Abdul Rashid, N. M., & Abdul Rahman, S. (2015). Low-temperature plasma-enhanced chemical vapour deposition of transfer-free graphene thin films. *Materials Letters, 158*, 436-438.

Pan, G., Li, B., Heath, M., Horsell, D., Wears, M. L., Al Taan, L., & Awan, S. (2013). Transfer-free growth of graphene on $SiO_2$ insulator substrate from sputtered carbon and nickel films. *Carbon, 65*, 349-358.

Paredes, J. I., Villar-Rodil, S., Solís-Fernández, P., Martínez-Alonso, A., & Tascon, J. (2009). Atomic force and scanning tunneling microscopy imaging of graphene nanosheets derived from graphite oxide. *Langmuir, 25*(10), 5957-5968.

Paul, R., Das, S., Dalui, S., Gayen, R., Roy, R., Bhar, R., & Pal, A. (2008). Synthesis of DLC films with different $sp^2/sp^3$ ratios and their hydrophobic behaviour. *Journal of Physics D: Applied Physics, 41*(5), 055309.

Peng, K.-J., Wu, C.-L., Lin, Y.-H., Liu, Y.-J., Tsai, D.-P., Pai, Y.-H., & Lin, G.-R. (2013). Hydrogen-free PECVD growth of few-layer graphene on an ultra-thin nickel film at the threshold dissolution temperature. *Journal of Materials Chemistry C, 1*(24), 3862-3870.

Peng, Z., Yan, Z., Sun, Z., & Tour, J. M. (2011). Direct growth of bilayer graphene on $SiO_2$ substrates by carbon diffusion through nickel. *ACS Nano, 5*(10), 8241-8247.

Peres, N., Guinea, F., & Neto, A. C. (2006). Electronic properties of disordered two-dimensional carbon. *Physical Review B, 73*(12), 125411.

Piscanec, S., Lazzeri, M., Mauri, F., Ferrari, A., & Robertson, J. (2004). Kohn anomalies and electron-phonon interactions in graphite. *Physical Review Letters, 93*(18), 185503.

Qi, J., Zheng, W., Zheng, X., Wang, X., & Tian, H. (2011). Relatively low temperature synthesis of graphene by radio frequency plasma enhanced chemical vapor deposition. *Applied Surface Science, 257*(15), 6531-6534.

Rafiee, J., Mi, X., Gullapalli, H., Thomas, A. V., Yavari, F., Shi, Y., . . . Koratkar, N. A. (2012). Wetting transparency of graphene. *Nature Materials, 11*(3), 217-222.

Reina, A., Jia, X., Ho, J., Nezich, D., Son, H., Bulovic, V., . . . Kong, J. (2008). Large area, few-layer graphene films on arbitrary substrates by chemical vapor deposition. *Nano Letters, 9*(1), 30-35.

Reina, A., Thiele, S., Jia, X., Bhaviripudi, S., Dresselhaus, M. S., Schaefer, J. A., & Kong, J. (2009). Growth of large-area single-and bi-layer graphene by controlled carbon precipitation on polycrystalline Ni surfaces. *Nano Research, 2*(6), 509-516.

Rosenthal, D., Ruta, M., Schlögl, R., & Kiwi-Minsker, L. (2010). Combined XPS and TPD study of oxygen-functionalized carbon nanofibers grown on sintered metal fibers. *Carbon, 48*(6), 1835-1843.

University of Malaya

Ruffieux, P., Gröning, O., Bielmann, M., Mauron, P., Schlapbach, L., & Gröning, P. (2002). Hydrogen adsorption on $sp^2$-bonded carbon: Influence of the local curvature. *Physical Review B, 66*(24), 245416.

Sansotera, M., Navarrini, W., Resnati, G., Metrangolo, P., Famulari, A., Bianchi, C. L., & Guarda, P. A. (2010). Preparation and characterization of superhydrophobic conductive fluorinated carbon blacks. *Carbon, 48*(15), 4382-4390.

Sasi, B., & Gopchandran, K. (2007). Nanostructured mesoporous nickel oxide thin films. *Nanotechnology, 18*(11), 115613.

Schabel, M. C., & Martins, J. L. (1992). Energetics of interplanar binding in graphite. *Physical Review B, 46*(11), 7185-7188.

Schauer, J.-C. (2007). *PECVD-deposition and characterisation of C-Si thin film systems on metals*. (Doctoral dissertation). Retrived from http://www-brs.ub.ruhr-uni-bochum.de/netahtml/HSS/Diss/SchauerJanineChristina/diss

Semenoff, G. W. (1984). Condensed-matter simulation of a three-dimensional anomaly. *Physical Review Letters, 53*(26), 2449-2452.

Shelton, J., Patil, H., & Blakely, J. (1974). Equilibrium segregation of carbon to a nickel (111) surface: A surface phase transition. *Surface Science, 43*(2), 493-520.

Shen, J., Li, T., Long, Y., Shi, M., Li, N., & Ye, M. (2012). One-step solid state preparation of reduced graphene oxide. *Carbon, 50*(6), 2134-2140.

Shi, F., Niu, J., Liu, J., Liu, F., Wang, Z., Feng, X. Q., & Zhang, X. (2007). Towards understanding why a superhydrophobic coating is needed by water striders. *Advanced Materials, 19*(17), 2257-2261.

Shih, C.-J., Strano, M. S., & Blankschtein, D. (2013). Wetting translucency of graphene. *Nature Materials, 12*(10), 866-869.

Shimabukuro, S., Hatakeyama, Y., Takeuchi, M., Itoh, T., & Nonomura, S. (2008). Preparation of carbon nanowall by hot-wire chemical vapor deposition and effects of substrate heating temperature and filament temperature. *Japanese Journal of Applied Physics, 47*(11), 8635-8640.

Slonczewski, J., & Weiss, P. (1958). Band structure of graphite. *Physical Review, 109*(2), 272-279.

Son, Y.-W., Cohen, M. L., & Louie, S. G. (2006). Energy gaps in graphene nanoribbons. *Physical Review Letters, 97*(21), 216803.

Srinivas, G., Zhu, Y., Piner, R., Skipper, N., Ellerby, M., & Ruoff, R. (2010). Synthesis of graphene-like nanosheets and their hydrogen adsorption capacity. *Carbon, 48*(3), 630-635.

Sutter, P., Sadowski, J. T., & Sutter, E. (2009). Graphene on Pt (111): Growth and substrate interaction. *Physical Review B, 80*(24), 245411.

University of Malaya

Sutter, P. W., Flege, J.-I., & Sutter, E. A. (2008). Epitaxial graphene on ruthenium. *Nature Materials, 7*(5), 406-411.

Thomsen, C., & Reich, S. (2000). Double resonant Raman scattering in graphite. *Physical Review Letters, 85*(24), 5214-5217.

Tian, W., Zhang, X., Chen, Z., & Ji, H. (2016). A review of graphene on NEMS. *Recent Patents on Nanotechnology, 10*(1), 3-10.

Tung, V. C., Allen, M. J., Yang, Y., & Kaner, R. B. (2009). High-throughput solution processing of large-scale graphene. *Nature Nanotechnology, 4*(1), 25-29.

Venezuela, P., Lazzeri, M., & Mauri, F. (2011). Theory of double-resonant Raman spectra in graphene: Intensity and line shape of defect-induced and two-phonon bands. *Physical Review B, 84*(3), 035433.

Vlassiouk, I., Regmi, M., Fulvio, P., Dai, S., Datskos, P., Eres, G., & Smirnov, S. (2011). Role of hydrogen in chemical vapor deposition growth of large single-crystal graphene. *ACS Nano, 5*(7), 6069-6076.

Wallace, P. R. (1947). The band theory of graphite. *Physical Review, 71*(9), 622-634.

Wang, J., Zhu, M., Outlaw, R., Zhao, X., Manos, D., Holloway, B., & Mammana, V. (2004). Free-standing subnanometer graphite sheets. *Applied Physics Letters, 85*(7), 1265-1267.

Wang, J., Zhu, M., Outlaw, R. A., Zhao, X., Manos, D. M., & Holloway, B. C. (2004). Synthesis of carbon nanosheets by inductively coupled radio-frequency plasma enhanced chemical vapor deposition. *Carbon, 42*(14), 2867-2872.

Wang, S. J., Geng, Y., Zheng, Q., & Kim, J.-K. (2010). Fabrication of highly conducting and transparent graphene films. *Carbon, 48*(6), 1815-1823.

Wang, W. L., Meng, S., & Kaxiras, E. (2008). Graphene nanoflakes with large spin. *Nano Letters, 8*(1), 241-245.

Wang, Y., Huang, Y., Song, Y., Zhang, X., Ma, Y., Liang, J., & Chen, Y. (2008). Room-temperature ferromagnetism of graphene. *Nano Letters, 9*(1), 220-224.

Wu, Z.-S., Ren, W., Gao, L., Zhao, J., Chen, Z., Liu, B., . . . Cheng, H.-M. (2009). Synthesis of graphene sheets with high electrical conductivity and good thermal stability by hydrogen arc discharge exfoliation. *ACS Nano, 3*(2), 411-417.

Xia, H., Li, W., Song, Y., Yang, X., Liu, X., Zhao, M., . . . Zhu, D. (2008). Tunable magnetism in carbon-ion-implanted highly oriented pyrolytic graphite. *Advanced Materials, 20*(24), 4679-4683.

Xu, Q. F., & Wang, J. N. (2009). A superhydrophobic coating on aluminium foil with an anti-corrosive property. *New Journal of Chemistry, 33*(4), 734-738.

University of Malaya

Xu, X.-H., Wu, H.-S., Zhang, C.-J., & Jin, Z.-H. (2001). Morphological properties of AlN piezoelectric thin films deposited by DC reactive magnetron sputtering. *Thin Solid Films, 388*(1), 62-67.

Yan, J., Henriksen, E. A., Kim, P., & Pinczuk, A. (2008). Observation of anomalous phonon softening in bilayer graphene. *Physical Review Letters, 101*(13), 136804.

Yan, Z., Peng, Z., Sun, Z., Yao, J., Zhu, Y., Liu, Z., . . . Tour, J. M. (2011). Growth of bilayer graphene on insulating substrates. *ACS Nano, 5*(10), 8187-8192.

Yang, D., Velamakanni, A., Bozoklu, G., Park, S., Stoller, M., Piner, R. D., . . . Ventrice, C. A. (2009). Chemical analysis of graphene oxide films after heat and chemical treatments by X-ray photoelectron and Micro-Raman spectroscopy. *Carbon, 47*(1), 145-152.

Yazyev, O. V. (2008). Magnetism in disordered graphene and irradiated graphite. *Physical Review Letters, 101*(3), 037203.

Yazyev, O. V. (2010). Emergence of magnetism in graphene materials and nanostructures. *Reports on Progress in Physics, 73*(5), 056501.

Yazyev, O. V., & Helm, L. (2007). Defect-induced magnetism in graphene. *Physical Review B, 75*(12), 125408.

Yazyev, O. V., & Louie, S. G. (2010). Topological defects in graphene: Dislocations and grain boundaries. *Physical Review B, 81*(19), 195420.

Yu, Q., Lian, J., Siriponglert, S., Li, H., Chen, Y. P., & Pei, S.-S. (2008). Graphene segregated on Ni surfaces and transferred to insulators. *Applied Physics Letters, 93*(11), 113103.

Zandiatashbar, A., Lee, G.-H., An, S. J., Lee, S., Mathew, N., Terrones, M., . . . Koratkar, N. (2014). Effect of defects on the intrinsic strength and stiffness of graphene. *Nature Communications, 5*(1), 3186.

Zhang, Y.-L., Wang, J.-N., He, Y., He, Y., Xu, B.-B., Wei, S., & Xiao, F.-S. (2011). Solvothermal synthesis of nanoporous polymer chalk for painting superhydrophobic surfaces. *Langmuir, 27*(20), 12585-12590.

Zhang, Y., Gomez, L., Ishikawa, F. N., Madaria, A., Ryu, K., Wang, C., . . . Zhou, C. (2010). Comparison of graphene growth on single-crystalline and polycrystalline Ni by chemical vapor deposition. *The Journal of Physical Chemistry Letters, 1*(20), 3101-3107.

Zhang, Y., Small, J. P., Pontius, W. V., & Kim, P. (2005). Fabrication and electric-field-dependent transport measurements of mesoscopic graphite devices. *Applied Physics Letters, 86*(7), 073104.

Zhang, Y., Wei, S., Liu, F., Du, Y., Liu, S., Ji, Y., . . . Xiao, F.-S. (2009). Superhydrophobic nanoporous polymers as efficient adsorbents for organic compounds. *Nano Today, 4*(2), 135-142.

University of Malaya

## LIST OF PUBLICATIONS AND PAPERS PRESENTED

1. **Othman, M**., Ritikos, R., Muhammad Hafiz, S., Khanis, N. H., Abdul Rashid, N. M., & Abdul Rahman, S. (2015). Low-temperature plasma-enhanced chemical vapour deposition of transfer-free graphene thin films. *Materials Letters, 158*, 436-438.

University of Malaya